Deutsches Zentrum für Luft- und Raumfahrt Göttingen
Justus-Liebig-Universität Giessen

Impact of Microwave Coupling and Magnetic Field Topology on Thrust and Beam Parameters in Electron Cyclotron Resonance Thrusters with Magnetic Nozzles

Dissertation

zur Erlangung des Grades
„Doktor rerum naturalium“
im Fach Physik

Clara Elisabeth Schäfer

Göttingen 2025

Blick gen Sterne.

Betreuer und Erstgutachter: Prof. Dr. Peter J. Klar
Zweitgutachter: Prof. Dr. Andreas Dillmann

Acknowledgement

First and foremost, I want to thank my support system - my family and friends. I'm especially grateful to my parents for their unwavering encouragement throughout my studies. Despite my choice to study in one of the most expensive cities, you have continually backed me in pursuing my interests and hobbies, even the more far-fetched (and, again, costly) ones. Beyond your financial support, what I admire most is your steadfast belief in my ability to succeed. For this, I thank you deeply. I would also like to thank Robin for his endless patience and help. Even though I moved 500 km away, you have been there never doubting that we would work through this journey together, making ”us” feel so effortless for me. Of course I thank you also for reviewing my texts (including parts of this one), which I know you may not have chosen to read but did anyway:). To my friends who (willingly) embarked on this PhD journey with me, thank you. You not only visited but also lent your ears to my endless rants and concerns. A special thanks to Fanny, Bianca, Nici, Dennis, Sinthu, and Johanna for being there throughout.

Now I'd like to thank my lab mates. In particular, my gratitude goes to Jana Zorn - not only for her support with the preliminary measurements and her endurance in sitting with me, often until it was dark and snowy outside, but also for helping me through challenging times. You always found a way to reframe the hard moments and laugh with me, making it all feel a bit lighter. I'm also grateful to the other PhD students in Giessen who welcomed and supported me as one of their own, even though I was only there a few weeks each year - thank you, Malina Reitemeyer, Konstantin Keil and Felix Becker. Finally, a big thank you to Jens Schmidt, Felix Plettenberg, Yung-An Chan, and Christopher Geile for all their support with testing, reading, and during the discussions. This work would not have been possible without your insights and help. Few things are as reassuring as standing together in front of something and no one knows what exactly happens and why it is not working :).

I would like to thank my team of supervisors and mentors, beginning with Peter Klar. Thank you for reading all of my articles and for providing such insightful and enthusiastic feedback! I am deeply grateful that you took so much time to guide me, discuss next steps, and explore the meaning of my work. I consider myself immensely lucky to have you as my Doktorvater, and I do not take any of this for granted. I also want to thank Kristof Holste, who dedicated his time to our quarterly meetings and took on the task of reviewing and correcting my work. With not just one, but two supervisors highly attuned to detail and formality, I've learned the infinite finesse of scientific writing. For this, I am grateful to both Kristof and, of course, Martin Grabe. As my supervisor on the DLR side, Martin, I thank you so much for all the Doktorandenmeetings. Your questions, which always challenged me and encouraged me to explore beyond my current understanding, have been invaluable. I am also grateful for your support in acquiring the necessary measurement equipment, lifting that burden from us and allowing us to focus on the work. Finally, my thanks go to Jan Martinez Schramm, for providing the opportunities to attend conferences, seminars, and workshops. I have always admired how you prioritize the person over the coworker, creating a safe, supportive working environment where I feel encouraged, both professionally and personally.

Of course, I also want to thank the ONERA electric propulsion team for allowing us to use the MINOTOR prototype as a reference thruster and for the engaging discussions at conferences.

Thank you all for an experience that, while perhaps not always easy, was incredibly exciting and rewarding! When I write “we” in the following sections, I truly mean it. Thank you all very much!

Declaration

I declare that I have completed this dissertation single-handedly without the unauthorized help of a second party and only with the assistance acknowledged therein. I have appropriately acknowledged and cited all text passages that are derived verbatim from or are based on the content of published work of others, and all information relating to verbal communications. I consent to the use of an anti-plagiarism software to check my thesis. I have abided by the principles of good scientific conduct laid down in the charter of the Justus Liebig University Giessen „Satzung der Justus-Liebig-Universität Gießen zur Sicherung guter wissenschaftlicher Praxis“ in carrying out the investigations described in the dissertation.

Date

Signature

Abstract

Conventional ion thruster technologies face challenges, such as electrode and grid erosion and the requirement of separate neutralizer devices for operating in space. Electric propulsion concepts that utilize electron cyclotron resonance (ECR) for plasma generation can eliminate the need for internal electrodes within the plasma. Furthermore, ECR concepts that employ magnetic nozzles to accelerate the entire plasma for thrust generation remove the need for both, neutralizers and acceleration grids. A new thruster concept, called DEEVA, developed at the German Aerospace Center (DLR), implements a magnetic nozzle for plasma acceleration and employs ECR for plasma ignition and heating.

Given its novel design, in this study we explore how the interaction between microwave coupling and the necessary magnetic field topology influences plasma properties, thrust generation, and thruster efficiency.

A series of experimental investigations is conducted to address this question. Alongside the development of three iterations of the DEEVA prototype, a reference thruster - the MINOTOR prototype, developed at the French National Aerospace Research Center (ONERA) - is examined. This reference thruster operates at a similar microwave frequency and within comparable power ranges. The presented investigations employ a range of experimental setups, vacuum test chambers, and plasma diagnostics. Tests are carried out in three vacuum facilities of different sizes. Diagnostic tools include a thrust balance, Faraday cups, retarding potential analyzers, and Langmuir probes.

Results indicate that the divergent magnetic field topology and coaxial coupling, realized by the MINOTOR thruster, produce higher ion currents and ion energies in the plasma plume than the first DEEVA prototype. By progressively adapting the DEEVA thruster's magnetic field topology in each prototype, allowing for larger ECR zones and higher magnetic field gradients, the latest DEEVA prototype (DEEVAv2-repulsive) achieves performance levels approaching those of the MINOTOR prototype.

While MINOTOR remains more efficient in the lower power range, findings suggest that adapting the magnetic field in case of the DEEVA concept can balance the power coupling effects. Additionally, DEEVA demonstrates greater flexibility in operating with various propellants and at higher power ranges, as it avoids exposing electrodes to the plasma, unlike the MINOTOR prototype, which uses a rod antenna inside the plasma to couple power. These advantages provide strong motivation to continue refining the DEEVA concept.

Zusammenfassung

Zu den Herausforderungen derzeitiger elektrischer Antriebskonzepte gehören Elektroden- und Gittererosion sowie die Notwendigkeit eines Neutralisators. Ein elektrisches Antriebkonzept, das eine elektrodenlose Plasmaerzeugung und -beschleunigung ermöglicht und zudem keinen Neutralisator benötigt, bietet einen erheblichen Vorteil für Langzeiteinsätze in der Raumfahrt. Ein solches Triebwerkskonzept wurde am Deutschen Zentrum für Luft- und Raumfahrt (DLR) entwickelt und trägt den Namen DEEVA. Es ermöglicht eine elektrodenlose Plasmaerzeugung durch Elektronenzyklotron-Resonanz mit Mikrowellen sowie die Beschleunigung des quasineutralen Plasmas durch eine magnetische Düse. Dadurch wird kein Neutralisator oder Beschleunigungsgitter benötigt.

In der vorliegenden Doktorarbeit wird erstmals an diesem Triebwerk untersucht, welchen Einfluss die elektrodenlose Leistungseinkopplung zusammen mit der erforderlichen Magnetfeldtopologie auf die Plasmacharakteristika im Strahl und damit einhergehend auf den erzeugten Schub ausübt.

Zur Beantwortung dieser Frage wurden drei Iterationen des DEEVA-Prototyps experimentell untersucht. Diese Ergebnisse werden mit einem Referenztriebwerk namens MINOTOR verglichen, das am französischen Nationalen Zentrum für Luft- und Raumfahrtforschung (ONERA) entwickelt wurde. Beide Triebwerkskonzepte, DEEVA und MINOTOR, arbeiten in ähnlichen Leistungs-, Volumenstrom- und Frequenzberei-chen. Alle Prototypen wurden unter vergleichbaren Umgebungsbedingungen untersucht (dieselben Kammern, dieselben Diagnostiken und Analysemethoden), um eine Vergleichbarkeit sicherzustellen. Tests wurden in drei Vakuumkammern unterschiedlicher Größe durchgeführt. Zu den Diagnostiken gehören Schubwaage, Faraday-Becher, Gegenfeld-Analysatoren und Langmuir-Sonden.

Die Untersuchungen zeigen, dass die koaxiale Einkopplung mit innerer Elektrode sowie ein rein divergentes Magnetfeld im Falle von MINOTOR zu höheren Ionenströmen und -energien führen und damit einhergehend zu höheren Schubwerten als im Falle von DEEVA. Allerdings zeigen die Ergebnisse auch, dass durch die schrittweise Anpassung der Magnetfeldtopologie des DEEVA Triebwerks in jeder Prototypgeneration, der neueste DEEVA Prototyp (DEEVAv2-repulsive) Performanceniveaus aufweist, die sich denen des MINOTOR Prototyps annähern.

Der MINOTOR Prototyp ist im unteren Leistungsbereich effizienter, jedoch demonstriert das DEEVA Triebwerk eine höhere Flexibilität in Bezug auf Treibstoffauswahl, Frequenz- und Leistungsbereich. Diese Vorteile bieten eine starke Motivation, das DEEVA-Konzept weiter zu verfolgen.

Contents

1. Introduction

1.1. Motivation for Electric Propulsion

Since the beginning of the 20th century, electric space propulsion (EP) has been considered as an alternative technology to conventional chemical propulsion in space. The term *electric* refers to the provision of charged particles (ions and electrons) by electrical energy. The basic concept of thrust generation for both forms of propulsion are Newton's laws of motion. A mass is accelerated and ejected. Due to the conservation of momentum and the interaction principle, thrust is generated by the product of ejection velocity and ejected mass per time interval. By increasing the ejection velocity, the ejected propellant mass can be reduced for the same thrust. This is a great advantage of electric propulsion in space. Even though the resulting thrust is currently still low due to the lower reaction mass, the possible ejection velocities of electric propulsion concepts exceed those of chemical thrusters by a factor of ten. This makes electric propulsion systems suitable for orbital (maintenance) manoeuvres of satellites, orbit raising, and deep space missions [1]. A higher ejection velocity directly results in lower propellant consumption for a given maneuver. Therefore, the efficient use of propellant is a key advantage of EP compared to chemical propulsion, where acceleration arises from converting chemical energy into kinetic energy through an expansion process. The efficiency of a thruster in terms of fuel consumption is measured by its specific impulse, defined as the impulse delivered per unit of propellant consumed and conventionally expressed in terms of weight at the surface of the Earth. The specific impulse is therefore expressed in seconds. The higher the specific impulse, the less propellant is required to achieve a given level of momentum. The high specific impulse of electric thrusters makes them highly appealing, enabling the attainment of high final velocities and total momentum, provided the thruster operates for a sufficiently long duration. Therefore, the lifetime of the propulsion system, primarily influenced by erosion and degradation of its components like the plasma chamber, electrodes, and neutralizers, emerges as a critical parameter. As a result, EP technology must exhibit exceptional reliability, with an extremely low probability of failure over an extended period. Additionally, a crucial consumable of an EP system is the propellant used. It largely dictates the thrust efficiency and the specific impulse level achievable. Propellant properties influencing performance include mass and ionization energy. The choice of propellant depends on thruster design, mission objectives, and duration. Common propellants employed in electric propulsion encompass xenon, argon, krypton, as well as more exotic molecules like iodine, air, and water [2].

Typical achievable thrusts for electric space applications range from 1 µN to 100 mN. There are many different concepts for the realization of electrical propulsion. A classification into three main groups is possible. The first are electrothermal thrusters. Here, the propellant gas is heated electrically and the thermodynamic expansion of the propellant gas is used with a nozzle for acceleration (Resistojets and Arcjets fall under this group). The second group are the so-called electrostatic thrusters. The ionization process and thus the generation of the plasma can vary here, but the acceleration, and as a result the thrust generation, takes place through a static electric field. This group includes gridded ion engines (GIE) and Hall thrusters (HT). The third class, which is relevant in what follows, are electromagnetic thrusters. These are thrusters that generate magnetic fields through plasma discharge processes, which contribute to acceleration. In many cases, additional static magnetic fields are added to define a suitable field topology for ignition and acceleration of the plasma. This group includes pulsed plasma thrusters (PPT) and magnetoplasmadynamic thrusters (MPDT). So-called electron cyclotron resonance thrusters (ECRT) also belong to this group [1].

Common challenges with existing ion or plasma thruster technologies are erosion of electrodes and grids, and the need for neutralizers [1]. Electrodes in contact with the plasma undergo wear and erosion over time, particularly at high power levels, thereby limiting the thruster's lifespan and reducing its reliability [2]. As for neutralizers; many EP systems require neutralizer devices either for operation and/ or for beam neutralization (f.e. GIEs or HTs). Neutralizers based on the principle of hollow cathode are technically challenging, since the thermal design of a hollow cathode is demanding due to the required thermionic emission of electrons from an insert material. Furthermore, the device is susceptible to failure because of embrittlement processes due to the inherent high temperature gradients, etc.

Neutralizer failure is one of the main reasons for the failure of conventional EP systems on satellites [1].

Plasma generation and acceleration through an electrode-less concept is therefore easily motivated. This includes plasma generation by electron cyclotron resonance (ECR). A thruster concept, where the whole plasma is accelerated (no need for a neutralizer) appears promising. This acceleration can be performed by a magnetic nozzle (MN). In light of the variety of EP thruster types available, in the following, attention is directed towards ECR thrusters as well as thrusters featuring MNs. Accordingly, notable members within the ECR thruster category are introduced. Subsequently, EP systems implementing MNs are explored. Finally, both aspects are integrated to present an overview of the current state-of-the-art in ECRTs equipped with MNs.

1.2. Overview of Thruster Concepts

1.2.1. Electron Cyclotron Resonance Thrusters

Plasma generation is understood as the creation of a large number of electrons and ions through multiplication processes initiated by a few free electrons via ion collisions. Initially, a neutral gas contains a small population of free, low-energy electrons. These electrons undergo multiplication when accelerated to the ionization energy of the neutral gas. This acceleration is facilitated by electric fields. These electric fields can be induced by either DC voltages or alternating fields. The focus here is on the ECR discharge. Alternating fields at higher frequencies can propagate within the plasma as electromagnetic waves, contributing significantly to plasma generation and heating. For instance, microwaves operating at 2.45 GHz, widely utilized in both material processing and everyday applications, can be resonantly absorbed by gyrating electrons at a magnetic flux density of 87.5 mT. This required magnetic field can be generated using either permanent magnets or electromagnets [3]. A typical set up for generating low-pressure, high-density plasmas using ECR in material processing involves coupling microwave power to the plasma across a dielectric window, rather than through direct connection to an electrode within the plasma [4]. The magnetic field in these configurations is generated by permanent and/or electromagnets [5]. In the realm of spacecraft propulsion, microwave thrusters hold the promise of eliminating the need for thermionic cathodes, as seen in DC discharge thrusters, and removing the requirement for dielectric discharge chambers in radio frequency thrusters. However, creating high-efficiency, high-thrust ion propulsion systems based on this technology can be challenging [5].

One of the best-known representatives of the ECR thruster group in the microwave regime is the µ10 ion thruster developed and described by Kuninaka *et. al.* Initially mentioned towards the end of the last century, the µ10 engine underwent numerous improvements and significantly benefited from the advancement of microwave generators, driven by progress in the wireless telephone and internet industry [6]. The µ10 ECR ion engine, along with its ECR neutralizer, was developed to address potential lifetime issues encountered with DC thrusters [7]. Specifically, it aimed to eliminate the need for hollow cathodes for primary electron generation and ion beam neutralization [7]. Thanks to the high level of reliability achieved, the µ10 ion engine has successfully operated during the two Hayabusa missions and is planned for use in the DESTINY+ mission [7]. The main features of this thruster include an ECR discharge with 4.25 GHz microwave frequency used to ionize xenon gas. Propellant enters the chamber through multiple injectors and is exposed to the microwave emitted from an antenna located in the waveguide. Permanent magnets, with a magnetic flux density of 0.4 T at their surface, are positioned in the discharge chamber to form a magnetic mirror. Xenon ions produced in the discharge are extracted through a high-voltage ion acceleration grid system [7].

A 0-dimensional ion production model for ECR ion thrusters emphasized the importance of investigating microwave power absorption efficiency [7]. In 2018, Coral *et al.* undertook a 2D investigation in this regard [7]. Additionally, they proposed a model that subdivided the ECR discharge chamber into three regions, which was validated through Langmuir probe measurements [7]. Subsequent studies aimed to enhance the thrust performance of the µ10 thruster. Tani *et al.* conducted tests in 2019 on a newly designed discharge chamber, which involved modifying the magnetic field geometry and adjusting propellant injection accordingly [8]. Measurements of ion current density inside and outside the discharge chamber were conducted, along with multi-charged ion measurements in the plume [8]. These improvements resulted in an ion beam current of 207 mA and a thrust of 12.0 mN at the maximum performance point [8].

Another ECRT system that aims to demonstrate the usage of water as a propellant was investigated by Nakagawa *et al.* [9]. Water, as a candidate for an alternative non-pressurized propellant for CubeSat thrusters, has the strong advantage of being a green propellant, allowing safer handling by humans on the ground. However, since oxidation is known as a clear disadvantage of using water and is fatal for hollow cathode operations, plasma generation without an electrode in the discharge chamber and also utilizing an ECR plasma as a neutralizer with a negatively biased voltage is therefore realized [9]. The here presented ECR ion source has a cylindrical discharge chamber equipped with two ring magnets, an antenna for the microwave, a screen grid and an accelerating grid to extract the ion beam [9]. Its operation condition are a microwave frequency of 4.25 GHz in the range from 0.25 to 6.6 W, a screen voltage of 1.50 kV and the accelerating voltage of −200 V. In the investigations performed by Nakagawa *et al.*, the mass flow rate was changed discretely, in the range of 50 µg /s in the case of water and 30 µg /s in the case of xenon [9]. Main objective was the investigation of alternative propellants for miniature ion thrusters to meet the demand of propulsion systems for micro-/nano-satellites. In the study the characteristics of the miniature ion thruster driven with water were compared with those of a xenon one using a global model and experiments [9]. For comparison with the developed global model, two kinds of experiments were conducted in that study: the ion source operation with water (for the comparison with xenon) and the ion population measurement in the plasma by a quadrupole mass spectrometer [9]. They observed a performance decrease in the propellant utilization efficiency and in the specific impulse using water as a propellant. Furthermore, differences between measurement and model were detected [9]. However, at a microwave power input of 0.25 to 6.0 W, the highest beam currents were about 12 mA for xenon and 18 mA for water. The difference from the experimental results was explained by the assumptions of the model, like the assumption of Maxwellian populations or spatial uniformity [9].

A similar set up utilizing xenon as propellant was investigated by Meng *et al.* in 2022 [10]. Equipped with two ring magnets, their ECR source operates within a power range of 0.5 W to 2 W at a microwave frequency of 4.2 GHz and a xenon mass flow rate ranging from 0.1 to 0.6 sccm. The accelerating grid system consists of two separate grids, each arranged with 211 holes in a circular area with a diameter of 20 mm. The main objective of this study was to determine the radial distribution of electron density using a non-invasive optical method [10]. Emissions were collected through the grid holes with an optical probe, and the electron parameters were obtained using the line-ratio method. The study revealed that the electron density profile was significantly influenced by the mass flow rate and input microwave power. At relatively low flow rates and power, a double-peak profile was observed, while a single peak distribution of electron density was observed at high flow rates and power. Electron densities in the range of 10^{16} to $10^{17}\,\mathrm{m}^{-3}$ were observed.

1.2.2. Electric Propulsion with Magnetic Nozzles

As the interest in electrodeless plasma thrusters for long-distance space travel grows, offering greater operational flexibility and lifetimes, magnetic nozzles (MN) are becoming increasingly prominent in recent space thruster development [11]. Resembling the traditional "de Laval" nozzle, a MN typically comprises a convergent-divergent topology of the applied magnetic field, guiding and accelerating a magnetized plasma jet into vacuum [12]. The diverging magnetic field radially confines the plasma and a self-consistent electrostatic field converts the thermal energy available in the electrons to ion kinetic energy. Therefore the electron response plays a crucial role in configuring the electrostatic field in the plume, responsible for ion acceleration and ultimately thrust generation [11]. One advantage of this plasma acceleration method is the absence of direct contact between the plasma and the walls of the discharge chamber. This reduces wall losses and simplifies plasma wall interaction description. Moreover, no electrodes are required for plasma acceleration or neutralization. Instead, the MN utilizes the expanding electron gas to neutralize the ion beam without the need for additional cathode installation [11]. This extends the thruster's lifetime and eliminates the need for complex neutralizer devices. Additionally, the capability to use multiple propellants is advantageous, along with the scalability and adaptability of a MN [12]. Various thrusters, both established and under development, exhibit different characteristics from the perspective of plasma generation and heating, yet they all realize the physics of quasi-neutral, quasi-collisionless plasma expansion in a MN [11]. In addition to ECR thrusters, as they are extensively discussed in the course of this work, it is pertinent to mention other advanced propulsion systems which incorporate MNs. These include the Magneto Plasma Dynamic Thruster, Helicon Plasma Thruster, and the Variable Specific Impulse Plasma Rocket. These systems utilize a range of alternative power sources spanning from radio frequency (RF) to microwave (MW) power, and all are equipped with a MN.

The Magneto Plasma Dynamic Thruster (MPDT) is an electromagnetic plasma accelerator that employs a coaxial configuration. In this set up, a high-current discharge ionizes a gas and propels it to high exhaust velocities through the Lorentz force generated by the interaction between the current flowing through the plasma and a self-induced or applied magnetic field [13]. With specific impulse ranging from 1500 to 8000 s and thrust efficiencies exceeding 40 %, particularly achieved at high power levels (above 100 kW), the steady-state version of the MPDT is recognized as a high-power propulsion solution. The challenge of inner conductor exposure to plasma, resulting in increased erosion, was stated to be mitigated by employing a multichannel hollow cathode and lithium as propellant in 1998 [13]. This approach was reported to yield processing power values in the range of 500 kW, generating thrust on the order of 12.5 N, and maintaining operation for 500 hours without significant erosion [13].

When operated with RF and a static magnetic field, EP thrusters are commonly referred to as Helicon Plasma Thrusters (HPT). This nomenclature stems from the fact that plasma density is augmented by helicon waves when applying static magnetic fields to the inductively-coupled RF plasma source, typically operated in the MHz range [14]. Helicon waves are electromagnetic waves observed in low-temperature, partially ionized plasmas in the presence of a static magnetic field. Ionization in helicon discharges is induced by helicon waves generated by an RF antenna [15]. Helicon sources represent versatile RF plasma sources capable of operating in various geometric or magnetic configurations, which influence the electric power transfer to the plasma and its subsequent expansion in a larger volume [16]. In addition to their utilization in electric propulsion, a substantial body of literature on helicon sources has emerged due to the diverse challenges posed by these discharges and the intriguing physics inherent in their solutions. The heightened interest in helicon discharges for space propulsion stems from their ability to generate high plasma densities compared to other RF sources at comparable power levels [15]. In the study conducted by Takahashi *et al.*, a permanent magnet HPT operating at a frequency of 13.56 MHz, with RF power reaching up to 2 kW and a flow rate of 24 sccm of argon, was examined [14]. The thruster featured a convergent-divergent magnetic nozzle, providing a maximum flux density of approximately 30 mT through arrays of permanent magnets. This set up resulted in a high plasma density downstream of the thruster exit. Direct thrust measurements yielded approximately 15 mN, with a specific impulse of around 2000 s, achieving a thrust efficiency of 7.5 % [14]. Additionally, Takahashi *et al.* investigated an RF thruster incorporating a MN in 2017, employing Langmuir probe measurements [17]. Temperature estimation was conducted based on the slope of the current-voltage characteristics at various spatial positions. The findings revealed that peripheral high-temperature electrons within the magnetic nozzle originated from the upstream antenna location and were transported along the connecting magnetic field lines. Operating conditions included a maximum flux density of approximately 40 mT, using 24 sccm of argon gas, and powering the RF antenna with a frequency of 13.56 MHz and a power setting of 1 kW [17]. Independent of the direct EP implementation of HPTs with MNs, Zhang *et al.* conducted measurements using a helicon plasma source equipped with a MN. This source is constructed from a glass tube, surrounded by a double saddle antenna, operating at a constant power of 310 W at a frequency of 13.56 MHz [18]. A solenoid positioned near the source exit is employed to generate a convergent-divergent magnetic nozzle. Their experiments provided empirical evidence of bi-directional ion acceleration along the axis of a convergent-divergent magnetic nozzle within a low-pressure laboratory plasma environment [18]. The axial profile of the ion saturation current, determined along the nozzle, exhibited a close correlation with the profile of the magnetic flux density. Ion beam potentials were measured on both sides of the magnetic nozzle and were found to be consistent with the maximum plasma potential measured at the throat.

In propulsion concepts such as inductively-coupled plasma (ICP) thrusters, HPTs, and ECRTs, RF or MW power is primarily coupled efficiently to electrons. These energized electrons then collide with neutrals of the propellant gas, initiating the ignition of a high-density plasma through collisional ionization processes [19]. While incorporating a helicon plasma source region, the Variable Specific Impulse Plasma Rocket (VASIMIR) thruster includes an ion cyclotron resonance heating (ICRH) region. In this thruster concept, the plasma generated by the helicon source is guided by a strong external magnetic field to a region where an RF signal equal to the ion cyclotron frequency is applied [19]. As per the conservation of magnetic momentum, the increased perpendicular velocity of the ions is converted into a high axial flow within the magnetic nozzle. Thus, unlike other thruster concepts (ICP, HPT, ECR), where most of the electric power is coupled to electrons, in VASIMIR, the majority of the power is coupled to ions, and their thermal energy is utilized to generate thrust [19]. To achieve the necessary field strength for ion cyclotron resonance heating, superconducting magnets with strengths above 1 to 2 T are employed. The laboratory experiments detailed in Longmier *et al.* [20] aimed to characterize the axial plasma potential profile within the expanding magnetic nozzle region of the VASIMIR-200i. These experiments identified the ion acceleration mechanism as an ambipolar electric field produced by an electron pressure gradient [20]. The helicon source, with a peak magnetic flux density of 0.17 T, operated with 25 mg/s argon propellant and 30 kW of RF power, yielded a measured argon ion kinetic energy of 20 eV. Additionally, a maximum plasma density of $10^{20}\,\mathrm{m}^{-3}$ and an electron temperature of 9 eV were detected in the helicon source. Notably, for these reported experiments, the ion cyclotron heating stage was not utilized [20]. The capability of utilizing the second stage, the ICRH stage, exemplifies one of the key advantages of the VASIMIR thruster. This feature allows for the adjustment of both thrust and specific impulse while operating at a fixed input power, rendering it an appealing option for a broad spectrum of potential space missions [21]. The control of ion velocity exiting the thruster is made possible by the RF wave coupling mechanism in the ICRH stage, which energizes the ions by launching the left-hand polarized slow mode waves from the high-field side of ion resonance [21]. In the study conducted by Olsen *et al.* [21] investigating the detachment process in the MN of a VASIMIR thruster, various diagnostic tools were employed. These included a retarding potential analyzer, electric field probe, plasma momentum flux sensor, 3-axis magnetometer, guard-ring Langmuir probe, and ion flux probe arrays [21]. They claimed that the plasma detachment from the applied MN occured through a two-stage process. The first stage involved a loss of adiabaticity, where the ratio of the ion Larmor radius to the magnetic field scale length approached unity. Subsequently, the second stage was characterized by the formation of high-frequency electric fields, facilitating competing interactions between detached ions and magnetized electrons [21].

1.2.3. Electron Cyclotron Resonance Thrusters with Magnetic Nozzle

The first propulsion design to use ECR with microwave frequency for plasma generation and a divergent magnetic field for plasma acceleration was published by Miller *et al.* in 1963 [22, 23]. In their study, they presented the first approaches to describe the operation and characteristics of their thruster, both theoretically and experimentally [22]. For this purpose, they assembled the necessary equations to explain the physical processes in an ECRT [22]. These include the absorption of a right-handed polarized EM wave with microwave frequency in a resonant magnetic field, as well as the formation of a space charge separation and the resulting electric field through the conversion of transverse to longitudinal velocity of the gyrating electrons [22]. In addition, they already addressed the process of detachment of the quasi neutral beam from the magnetic field lines and the thereby generated thrust [22]. Furthermore, the influences by magnetic field strength and gas densities were investigated by experimental examination of the plasma and the beam [22]. For this purpose, two radio frequency probes (antennas) were mounted in quartz glass and placed inside the plasma [22]. A pendulum calorimeter was inserted into the beam, which allowed a temperature measurement in addition to the deflection [22]. Furthermore, two electrodes were placed in the beam to determine the difference in potential at two different positions. With an input power of 300 W and a frequency of 2.45 GHz they claimed 20 % of input power in the beam. During the same period, similar analytical and experimental investigations were carried out in Tokyo by Nagatomo *et al.* [23, 24]. In this study, two propulsion systems with different diameters were investigated [24]. Argon was specified as the propellant gas [24]. Langmuir probes and an electrostatic energy analyzer were used as plasma and beam diagnostics. Also, the force acting on the magnetic field generating coils, due to the accelerated plasma, was measured. A total efficiency of 8 % was claimed. The advancement of studies aimed at further analytically and experimentally investigating ECR plasma acceleration occurred 20 years later, conducted by Sercel *et al.* [25, 26]. In their research, a microwave power supply ranging from 0.3 to 7.0 kW was utilized (with operation possible only above 300 W), along with argon as the propellant in the range of 5 to 20 sccm. The magnetic field required for resonance and acceleration was generated by a magnetic solenoid, consisting of a water-cooled copper coil with approximately 150 turns. To attain a resonance field of 75 mT in the diverging region of the field, the solenoid necessitated a steady current of 160 amperes at around 25 V [26]. Subsequently, Kaufman *et al.* [27] conducted plasma measurements on the device using movable diagnostic probes, including a Faraday cup and a gridded energy analyzer, while varying the propellant gas flow rate and input microwave power level. Their observations revealed that ion energies decreased with increasing flow rate and background pressure, while the microwave power level had a negligible effect on the ion energy. The measured ion energies ranged from 20 to 40 eV. The calculated propulsion parameters indicated that the efficiency of the laboratory device was low and that the tank pressure significantly influenced its performance [27]. In the following years, the development of other electric space propulsion systems (HT/PPT etc.) continued, while in comparison the development work on the ECRT did not show sufficient potential to continue [23].

In recent years, the concept of ECRT with MN was reestablished by ONERA (fr. Office national d'études et de recherches aérospatiales). The patent-protected thruster concept [28] and the determined characteristics were presented in 2013 by Jarrige *et al.* [29] and 2015 by Cannat *et al.* [30]. Their thruster prototype consisted of two coaxial cylinders connected to a microwave coaxial transmission line [30]. Argon or xenon gas was injected into the thruster through a number of small holes in the backwall [30]. The external magnetic field was produced using either a set of permanent magnets or a multi-layer, water-cooled coil [30]. The probes used for the characterization of the thruster plume were gridded Faraday probes for ion current density measurements, retarding potential analyzer (RPA) and a Hiden Plasma Sampling Mass (PSM) ion analyzer for ion energy distribution function measurements and a Langmuir probe to measure the electron temperature [30]. With a microwave power of 30 W and a xenon flow rate of 0.1 mg/s a thrust of 1 mN was estimated based on probe measurements [30]. In the years that followed, and up to the present day, various publications under the project *Magnetic Nozzle Electron Cyclotron Resonance Thruster* (MINOTOR) focused on conceptual modifications and optimization of the thruster [31, 32, 33, 34]. This was made possible by various diagnostic and analytical methods, which demonstrate a high degree of repeatability and reliability of the data. Diagnostic tools included Langmuir probe (LP), laser induced fluorescence (LIF), thrust balance (TB), diamagnetic loop and numerical models [32]. Facility tests were performed as well as various gas inlet system tests [32], showing high influence of chamber and background pressure on the performance of the thruster. This makes it harder to reproduce the exact parameters of the same thruster in different vacuum chambers. It is essential to correlate the historical development of ECRT with the understanding and reliability of the diagnostic methods used to characterize these thrusters. Although the various past studies indicate the increasing reliability of the data, various publications also point to discrepancies, both between different diagnostic methods and between theory and experiment [23]. During the development of the thruster, various designs were characterized using a wide range of tools [32]. Design options include different diameters of the discharge chamber and different coupling versions of the microwave (antenna and waveguide) [23, 32, 35]. It was found that the microwave coupling via waveguides instead of a coaxial structure leads to smaller ion energies and resulting thrust [23, 35]. It was stated in various publications that in fact the ion energy was an intrinsic feature of the microwave coupling [23, 35]. However, the concept that yields favorable performance, wherein the inner conductor is exposed to the plasma, limits the thruster's lifetime drastically.

To circumvent this issue, Inchingolo *et al.* introduced a concept for a circular waveguide ECRT prototype powered by microwaves at 5.8 GHz within a power range of 80 to 300 W in 2023 [36]. This prototype features a magnetic field generated by a combination of Sm-CoYXG32 magnets, facilitating ECR, and an electromagnet responsible for shaping the diverging MN while allowing for the adjustment of the resonance position and MN geometry. The analysis of the main plasma plume properties was conducted using electrostatic probes while varying parameters such as the mass flow rate of xenon propellant, microwave power, electromagnet current, and propellant injector design. The study revealed that a single radial injector hole was inadequate for achieving a symmetric ion current profile and demonstrated that both the shape and strength of the magnetic nozzle significantly influenced the divergence angle and thruster floating potential [36]. Notably, a utilization efficiency of up to 70% and electron temperatures reaching 16 eV were measured [36].

In 2016, Ganguli *et al.* [37] introduced an alternative propulsion concept known as the Compact ECR Plasma Source (CEPS). This portable device operates with microwaves at 2.45 GHz up to 800 W of power. The microwaves are generated by a standard magnetron mounted on a rectangular waveguide launcher. A system of waveguide transitions and tuning possibilities allows microwave coupling through a microwave-transparent window [37]. The required magnetic field is generated by a set of appropriately designed NdFeB ring magnets. Plasma densities ranging from 9×10^{11} to $10^{12}\,\mathrm{cm}^{-3}$ and electron temperatures in the range of approximately 2 to 3 eV were determined [37]. Empirical estimates for the application of CEPS as a thruster using argon yielded peak thrusts ranging from 2.5 to 7.5 mN, achieved with microwave powers of approximately 500 W [38]. Furthermore, Moloney *et al.* investigated the AQUAJET propulsion system, which implements ECR heating using a microwave frequency of 2.45 GHz. This system employs a single hollow cylindrical permanent magnet to create a magnetic nozzle and achieve ambipolar acceleration [39]. Structurally, it bears resemblance to the MINOTOR thruster; however, it differs in that the inner conductor, acting as the antenna, is insulated from the plasma by a dielectric slab and sleeve made from boron nitride. This cathodeless design allows the propulsion system to operate with a wide range of alternative propellants, including argon, xenon, and water. Direct thrust measurements were obtained using a pendulum-type thrust balance while operating at load power levels ranging from 17 to 171 W with various propellants at different mass flow rates. The AQUAJET system demonstrated thrust and specific impulse values of up to 0.72 mN and 736 s, respectively, at 171 W with argon; 0.83 mN and 861 s at 143 W with xenon; and 0.26 mN and 188 s at 82 W with water [39].

However, the further pursuit in the last ten years of ECR thrusters based on MW technology and equipped with MN can be traced back to ONERA's patent on the MINOTOR-like thruster [28]. A thruster that operates in a similar power, frequency and mass flow range, demonstrates similar efficiency and performance, but avoids electrode erosion (of the inner conductor) is therefore still a challenge for subsequent innovations. An alternative propulsion concept utilizing a different approach to microwave coupling, neither coaxial with an inner conductor nor via waveguide transitions through a window upstream of the MN, holds promise for achieving comparable thrust and efficiency within the same power range. Such an innovative approach, featuring a magnetic nozzle, could facilitate electrodeless plasma generation, thereby eliminating the need for an antenna within the plasma, while enabling effective plasma acceleration.

1.3. Research Question and Approach

The Decentralized Energy supplied Electric Propulsion (DEEP) project, jointly conducted by various institutes of the German Aerospace Center, aims to advance EP technology. The project focuses on developing a thruster that utilizes a microwave electron cyclotron resonance plasma discharge combined with a magnetic nozzle for plasma acceleration, alongside structure-integrated supercapacitors and a battery. This hybrid power supply system is designed to enable the use of lower-power batteries and solar panels on the satellite itself, thereby reducing overall mass and increasing available payload mass [40]. The DEEP project introduces the DEEVA thruster (*DLR Electrodeless ECR Via microwave plasma Accelerator*), which is discussed in the course of this thesis. The DEEVA thruster concept utilizes electrode-less microwave coupling through an annular waveguide (ring cavity), transmitting power through two resonant coupling slots into the plasma discharge chamber made of quartz. Additionally, the thruster employs a diverging magnetic field to form a magnetic nozzle, enabling electrodeless acceleration of a quasi-neutral plasma and eliminating the need for a neutralizer.

The concept of microwave coupling for an electron cyclotron resonance plasma through an annular waveguide — using a slotted antenna called SLAN — was firstly introduced by Werner, Korzec, and Engemann in 1994 in the context of surface processing [41, 42, 43, 44]. Building on this, the innovative approach of combining this microwave coupling with a magnetic field topology that forms a magnetic nozzle, enabling an electrodeless and neutralizer-free electric space propulsion system, introduces additional complexity in understanding the effects of the plasma.

Consequently, the central question of this study emerges: How does the electrodeless microwave coupling in conjunction with the magnetic field topology influence the plasma and the thruster parameters and thus ultimately the thrust?

To address this question, an experimental approach is adopted involving a series of mappings of plasma and beam parameters of the new DEEVA thruster under variable operational conditions. To deepen the understanding of the processes influencing the determined plasma parameters and thruster behavior, the observations are compared with those obtained from a prototype of the established MINOTOR thruster. Both thrusters operate within comparable power, frequency, and volume flow ranges, are of similar size, and are subject to similar environmental conditions during investigation.

1.4. Thesis Structure

To address the central question, it is imperative to introduce the first prototype of the DEEVA thruster (DEEVAv1), as it serves as the foundation for formulating initial hypotheses on its operating principle. Chronologically, at the outset of thruster development, both the MINOTOR reference prototype and the initial DEEVAv1 prototype were available for testing. By comparing the plasma and beam findings of DEEVAv1 with those of MINOTOR, preliminary hypotheses regarding the impact of microwave coupling and magnetic fields on thruster operation were formulated. These initial hypotheses then guided the development of the second prototype (DEEVAv2), aimed at validating these hypotheses. However, to avoid redundancy, the results will not be presented chronologically in this work. Instead, the findings and working hypotheses of all engines will be presented concurrently, with a comprehensive summary and discussion provided in the subsequent section.

The thesis is structured as follows: In Chapter 2, we firstly introduce in Section 2.1 the fundamentals covering basic plasma physics and deepen the understanding of specifically ECR plasmas in static magnetic fields. In Section 2.2 the thruster versions and the reference thruster are presented. The operating principles, covering elements of microwave engineering are outlined, and the existing literature values and models of the reference thruster, MINOTOR, are recapitulated. Since the measurements are conducted in different test facilities, the respective properties are also presented. In Section 2.3 all necessary information about diagnostic tools, such as magnetic field probe, Langmuir probe, Faraday cup, thrust balance, and retarding potential analyzer are provided. The evaluation procedures, as well as limitations and influence factors that may affect or restrict the conclusions drawn from the measurements, are discussed.

Chapter 3 is structured as follows: First, we introduce the configurations of the prototypes and the propellants in use. We then present thrust balance results for the prototypes in Section 3.2, leading to initial observations that differentiate between the development stages of the DEEVA and MINOTOR prototype. To address the extent to which microwave coupling and magnetic field topology affect plasma parameters and thrust, we proceed systematically by investigating the different contributions to the thrust. First, we show the measured magnetic field topologies of the prototypes in Section 3.3, where the initial promising characteristics of each thruster are already identified. Next, we examine the characteristics of MNs in Section 3.4, naturally considering the electrons and the associated ion dynamics. In Sections 3.5 and 3.6, we compare the ion energies and ion currents extracted by the thrusters, allowing us to calculate thrust-contributing force values attributed to high-energy ions. By comparing these force values with the thrusts measured by thrust balance tests, we derive in Section 3.7 to a ratio that can be interpreted as an efficiency factor—indicating how well the effects of the MN (i.e., the high-energy ion current) are utilized for thrust. Comparing these ratios provides insight into which prototypes make effective use of the MN effects.

Additionally, the development stages of the DEEVA thruster reveal adjustments that can be made to make better use of the MN effects and improve engine performance. These aspects are discussed further in Chapter 4. In that chapter, we first summarize the findings before engaging in a critical discussion. We address limitations, assumptions, and challenges that need to be overcome in future experiments, while also presenting potential improvements to the DEEVA prototype. Finally, we tackle the central question regarding the influence of microwave coupling and magnetic field topology on plasma and thrust parameters, providing an answer based on the results and discussions presented.

2. Theoretical Background and Experimental Details

In the previous chapter, we have covered various propulsion systems established and investigated in previous studies. We also introduced some concepts, like ECR and MN, without going into detail. In this chapter, we aim to address this gap by following the logic of basic questions related to the development and operating principles of an electric propulsion system equipped with a MN. For this purpose we seek answers to the following questions:

First, what is a basic characteristic of a space propulsion system? What is the main difference between chemical and electric space propulsion? Since electric propulsion is driven by plasmas, we need to understand: What is a plasma? What properties can be assigned to matter in the plasma state? How can we ignite a plasma and sustain/heat it? How can we accelerate the plasma and exhaust it to produce thrust? These questions will guide us through the first part of this chapter. We will then explore the technical realization of a plasma thruster by addressing the questions: What kind of technology in the microwave regime is necessary for this realization? How was an ECR plasma thruster with MN realized in previous studies? What was the outcome of previous thruster development, and what challenges remain? How can we circumvent these challenges? In the third part of this chapter, we introduce the plasma and thruster diagnostics implemented and present the experimental set ups. We provide some exemplary evaluation procedures and discuss a possible impact of the diagnostic probes on the measurement results.

2.1. Fundamentals for Electric Propulsion

We start with the two questions; What is a basic characteristic of a space propulsion system? What is the main difference between chemical and electric space propulsion? To describe one of the most important parameters in space travel and rocket science, reference is made to the Tsiolkovsky equation. This equation, based on Newtons axiom "actio=reactio" describes the speed increment, i.e. the difference in the speed of a rocket or spacecraft, depending on the fuel used and its exit velocity. The derivation of this equation from the momentum equation can be found in various textbooks, i.e. Ref. 45.

Assuming constant exit velocity, the velocity increment Δv of a rocket or spacecraft can be given by Eq. 2.1, where m_0 describes the start mass, m_f the final mass after the acceleration phase and c_e denotes the effective exit velocity:

$$\Delta v = c_\mathrm{e} \ln\left(\frac{m_0}{m_\mathrm{f}}\right). \tag{2.1}$$

The exit velocity is defined by the thrust produced T_T and the massflow $\dot{m}$:

$$c_\mathrm{e} = \frac{T_\mathrm{T}}{\dot{m}}. \tag{2.2}$$

In rocketry, it is common to use the weight-specific impulse I_s in seconds s. For that reason the exit velocity is normalized with the gravitational acceleration of $g \approx 9.81\,\mathrm{m/s^2}$ [45]:

$$I_\mathrm{sp} = \frac{c_\mathrm{e}}{g}. \tag{2.3}$$

By that it is then possible to define an efficiency η of the spacecraft or rocket with respect to an input power P_i. This allows us to compare and evaluate the performance of electric and chemical propulsion:

$$\eta = \frac{T_\mathrm{T}^2}{2\,\dot{m}\,P_\mathrm{i}}. \tag{2.4}$$

In chemical thrusters the exit velocity is limited by the chemical energy stored inside the fuel and its conversion into kinetic energy. In electric thrusters the exit velocity is theoretically limited only by the speed of light. Compared to the maximum theoretical exit velocities of around 5 km/s at chemical thrusters, electric thrusters reach exit speeds of up to 50 km/s. As a consequence, the ratio of propellant mass to spacecraft dry mass is significantly lower for EP compared to chemical propulsion. EP achieves high specific impulse (I_{sp}) values, approaching several thousand seconds, due to the separation of energy source from expelled propellant. However, onboard spacecraft power is limited to tens of watts to a few kilowatts, primarily sourced from solar panels, restricting EP systems to very low (nN) to low (mN) thrust levels. Despite this limitation, plasma propulsion remains advantageous for tasks like station keeping, attitude control, efficient orbit transfers, deep space exploration, and de-orbiting maneuvers [1, 2, 46].

2.1.1. Basics Plasma Physics

What is a plasma? What properties can be assigned to matter in the plasma state? Important characteristics of plasma are connected to its definition. One speaks of matter in a plasma state, if it fullfills some basic properties. It is possible to define plasma as an ensemble of free charged particles which interact mechanically (via collisions) and electromagnetically, but the ensemble as a whole is charge neutral. One important property is the effective shielding of the electric potential of the charged particles. The connection between density of particles and their electrostatic potential is described by the Maxwell-Boltzmann-distribution in phase space [3]:

$$f(r,v) = n_0 \sqrt{\frac{m^3}{(2\pi T)^3}} \exp\left(-\frac{\frac{1}{2}mv^2 + q\phi}{T}\right). \tag{2.5}$$

The spatial dependence lies in the particle number density in the potential-free space, n_0 as well as in the potential ϕ and the temperature T. In the following, temperatures are given in eV, so the Boltzmann constant k_{B} is omitted. The integral over the Maxwell distribution in velocity space is normalized to 1, so that a Taylor expansion can be used to determine the particle density of the two species (electrons and ions). With the Poisson equation ($\Delta\phi(r) = -\rho(r)/\epsilon$) it is then possible to derive an expression for the potential, the so called Debye-Hückel potential:

$$\begin{aligned} \phi(r) &= \frac{q_0}{4\pi\epsilon_0}\frac{1}{r}\exp\left(-\frac{\sqrt{2e^2 n}r}{\sqrt{\epsilon_0 T}}\right) \\ &= \frac{q_0}{4\pi\epsilon_0}\frac{1}{r}\exp\left(-\frac{\sqrt{2}r}{\lambda_{\mathrm{D}}}\right), \end{aligned} \tag{2.6}$$

where $\phi(r)$ is the potential and q_0 is the charge and r is the distance. Depending on the density of the electrons n, the temperature T and the vacuum permittivity ϵ_0, the potential $\phi(r)$ of a positive charge is therefore efficiently shielded (down to $1/e$) within the range of the so called Debye length λ_{D}[3]:

$$\lambda_{\mathrm{D}} = \sqrt{\frac{\epsilon_0 T}{e^2 n_0}}. \tag{2.7}$$

In contrast to the Coulomb potential of a charged particle ($1/r$ dependence), the Debye-Hückel potential of a plasma decreases exponentially. Therefore, matter being in the plasma state requires that its spatial dimension L is significantly larger than the Debye length, i.e. for $L \gg \lambda_{\mathrm{D}}$. Otherwise the collective properties of a plasma cannot appear.

Another important feature of the charge density is its response to external electric fields. An external electric field leads to a displacement of positive and negative particles until the field is neutralized within the plasma. As the electrons are much lighter and respond faster to external fields, their dynamics determine the response of the plasma at higher frequencies from MHz to THz. The solution of the Poisson equation, in response to an electric field leads to a harmonic oscillation. An eigenfrequency is found, the so called plasma frequency ω_{P}, with e as the electron charge, n as the density, ϵ_0 the vacuum permittivity and m_e as the electron mass:

$$\omega_\mathrm{p} = \omega_\mathrm{pe} = \sqrt{\frac{e^2 n}{\epsilon_0 m_\mathrm{e}}}. \tag{2.8}$$

The charge density in the plasma can therefore not react to electric field modulation faster than the plasma frequency. Electromagnetic waves with lower frequency than the plasma frequency ($\omega < \omega_\mathrm{p}$) are reflected and cannot penetrate into the plasma. The frequency of the electrons is usually given as the plasma frequency, as they are responsible for the fastest response of the plasma to electric fields. The plasma frequency of the ions also plays a role in wave phenomena and is given as:

$$\omega_\mathrm{pi} = \sqrt{\frac{e^2 Z_\mathrm{i} n_\mathrm{i}}{\epsilon_0 m_\mathrm{i}}}. \tag{2.9}$$

It is important to note, that we assume a quasi neutrality of the plasma, therefore the density of electrons n_e and ions n_i are described by the relation:

$$n_\mathrm{e} = Z_\mathrm{i} n_\mathrm{i}, \tag{2.10}$$

where Z_i denotes the average charge state of the ions.

Ionization Process

How can we ignite a plasma and keep it running? Several chemical and physical reactions can lead to a change of a former neutral atom to a charged or excited one. Main focus of this section lies on the discussion of the gases argon and xenon, since they are meant to be propellant for the here discussed spacecraft application. The simplest way of generating a positive ion is the ionization by direct electron impact. An electron e with a kinetic energy high enough to provide the ionization energy collides with the neutral Ar atom [47]. In that case an additional electron is produced:

$$e + \mathrm{Ar} \rightarrow \mathrm{Ar}^+ + e + e.$$

The cross section σ of an electron with an energy E_0 in this ionization process is described by the Rutherford differential scattering cross section, which describes the probability that the scattered particle is deflected into the solid angle $\mathrm{d}\Omega = 2\pi \sin(\theta)\mathrm{d}\theta$:

$$\frac{\mathrm{d}\sigma}{\mathrm{d}\Omega} = \left(\frac{1}{4\pi\epsilon_0}\frac{Z_1 e^2}{4E_\mathrm{e}}\right)^2 \sin^{-4}\left(\frac{\theta}{2}\right). \tag{2.11}$$

$Z_1 e^2$ describes the product of the charges of the atom $Z_1 e$ and the scattered electron e, with e as the electron charge of $e = 1.6 \cdot 10^{-19}\,\mathrm{C}$ and ϵ_0 as the vacuum permittivity. In order to ionize the atom, the electron energy E_0 has to match or exceed the ionization energy of the atom: $E_0 \geq E_\mathrm{ion}$. This cross section can be integrated over the electron distribution function, namely the quasi-equilibrium Maxwell-Boltzmann-distribution describing the probability to find an electron with an energy E_e, compare Equation 2.5. The integration of the cross section leads, together with the velocity distribution, to the ionization/reaction rate coefficient k_coeff, inhibiting the information about the number of processes (collisions) within a unit time and unit volume. This reaction rate coefficient can be determined in dependence on the velocity of the electron v_e:

$$k_\mathrm{coeff}(T_\mathrm{e}) = \int \sigma(v) v f(v) dv = \langle \sigma v_\mathrm{e} \rangle. \tag{2.12}$$

The reaction rate coefficient is therefore an integral factor, containing information about the energy distribution functions and depending on the temperature/mean energies of the collision partners. The braket represents the averaging process and considers that the velocity is mostly attributed to the lighter collision partners, the electrons. In total, the rate of direct ionization by electron impact ω_ion can then be calculated with the electron density n_e and density of neutral particles n_0:

$$\omega_{\mathrm{ion}} = k_{\mathrm{coeff}}(T_{\mathrm{e}})n_{\mathrm{e}}n_0. \tag{2.13}$$

Another important ionization process is the photo ionization [47]. Photo ionization occurs when a photon γ with sufficiently high energy ionizes an atom Ar. This may happen directly, if the photon's energy is above the ionization energy of the atom. Alternatively, if the atom is already in an excited state, a photon with lower energy can ionize it [47]:

$$\gamma + \mathrm{Ar} \to \mathrm{Ar}^+ + e.$$

As an example, the energy of a microwave quantum is determined with the Planck constant h as follows:

$$E_\gamma = hf \Rightarrow E_\gamma = 4.136 \cdot 10^{-15}\mathrm{eVs} \cdot 2.45 \cdot 10^9\mathrm{Hz} = 10.1 \cdot 10^{-6}\,\mathrm{eV}. \tag{2.14}$$

This is not enough to ionize itself, e.g., argon atoms, with an ionization energy $E_{\mathrm{ion}} \approx 15.7\,\mathrm{eV}$. Photo ionization can therefore in this case just come into play, if the atoms are already excited by an earlier electron impact. However, those excited/metastable states may decay in different possible ways, e.g. by sending out photons of a specific wavelength. Glow discharges of different elements exhibit different spectra as the energy states involved are different. In case of molecules, relaxation may also take place internally via excitation of vibrations or rotations. Stepwise ionization by electron impact can occur in thermal or energy-intense discharges. This process is comparable to the stepwise photo ionization: A neutral atom or molecule collides with an electron, which does not ionize the atom but transfers energy to one of its bound electrons. The atom is now excited, for example in a metastable state. If it is hit by another low-energy electron, it can be ionized even though the kinetic energy of the latter electron is lower than the ionization energy E_{ion} [47].
As an example of the energy levels of argon:

- Ionization: ($e + \mathrm{Ar} \to \mathrm{Ar}^+ + e + e$): $E_{\mathrm{ion}} \approx 15.8\,\mathrm{eV}$.
- Excitation: ($e + \mathrm{Ar} \to \mathrm{Ar}^* + e$): $E_{\mathrm{exc}} \approx 11.6\,\mathrm{eV}$.

Each ionization process requires a free electron. This electron can be produced either by photo ionization or by electron collision. This free electron can be accelerated until its kinetic energy reaches the ionization or excitation energy of the gas. This acceleration occurs through electric fields. The intensity and frequency of these fields, as well as how they are introduced into the plasma, can vary. This accelerated, free electron can contribute to creating additional metastable or ionized atoms. Metastable states, themselves can be turned into ionized ones by colliding with an electron or by absorbing a photon. These three processes are the most relevant since we are dealing with noble gases, which are monoatomic. We are therefore not discussing molecular or poly-/diatomic effects like dissociative ionization or Penning ionization. We want to present some possible ways to apply accelerating electric fields into a gas or plasma to ignite and further heat it, to compensate recombination processes in the next subsection.

Plasma Sources

The process of plasma generation is typically initiated by accelerating few low-energy electrons by electric fields to the ionization energy of the background gas. There are several ways to couple electric fields into the gas, as well as into the generated plasma, to further heat it. The resulting plasmas are called according to the coupling mechanism, e.g. inductively coupled plasma etc. [3]. We want to give a description of the different coupling methods and the resulting characteristics. One of the most common plasma sources which is based on a strong, static electric field is the so called glow discharge. Such discharges are used in fluorescent tubes. Thermionic plasma sources use a filament heated with electricity (or directly cathodes) which emits high-energy electrons. Similar to glow discharges, the electrons of the thermionic plasma source can additionally be accelerated by electric fields. Especially for material surface processing one uses alternating fields. Here it is distinguished between capacitive and inductive plasmas. Both capacitive and inductive plasmas are usually driven by frequencies around 13.56 MHz, and are therefore referred to as RF plasmas [3]. If the plasma is located between two electrodes (like a capacitor) one speaks of an capacitive plasma. Here ions and electrons are accelerated directly onto the electrodes, which can lead to high sputter rates. One can use dielectrics in front of one electrode and then ignite a plasma, called dielectric barrier discharge. This delays the discharge development and leads to lower plasma densities. Is the alternating field coupled into the plasma by an inductance and the plasma is situated inside a coil, one speaks of an inductive plasma. In comparison to a capacitive plasma, the sputter rates are minimized in this configuration. If the driving frequency is high, around 2.45 GHz one speaks of a microwave plasma. Here, the alternating fields can propagate inside the plasma and heat it from within. If the electrons shall be accelerated exclusively by the microwave, a resonator is necessary in order to deliver a sufficient strength of the electric field. On the other hand, one can use a magnetic field with suitable magnitude to make use of the electron cyclotron resonance, these are the so called ECR plasmas [3].

2.1.2. Plasma in a Static Magnetic Field

In order to understand how such ECR plasmas are heated, more precisely how microwaves can propagate in a plasma exposed to an external magnetic field, a fundamental understanding of the influence of electric and magnetic fields on the medium plasma is required. Furthermore, it is necessary to look at relevant wave phenomena. To describe the influence of time-dependent electromagnetic fields on trajectories of charged particles, we first consider the trajectories of plasma particles in homogeneous, time-independent magnetic fields. This also lays the ground for basics of magnetic nozzle designs.

For clarification, we use the terms magnetic field and magnetic flux density interchangeably and with the same meaning: The area density of the magnetic flux vertically through a surface element, measured in units of Tesla or Gauss. Magnetic field lines visualize the direction and sense of direction of the magnetic field or magnetic flux at each point of the field. The magnitude of the field strength/the magnetic flux density is therefore proportional to the field line density.

Starting point is the equation of motion for a charged particle in a magnetic field that is constant in space and time. Newton's equation of motion with mass m, charge q and the Lorentz force $\vec{F}_\mathrm{L} = \vec{v} \times \vec{B}$ and an additional general force $\vec{F}$ reads:

$$m\dot{\vec{v}} = q\vec{v} \times \vec{B} + \vec{F}. \tag{2.15}$$

Without an additional external force $\vec{F}$, the velocity components can be determined in relation to the magnetic field direction. The Lorentz force creates a gyration with frequency ω_C for the velocity components perpendicular to the magnetic field, which depends on the flux density of the magnetic field B, the charge of the particle q and its m:

$$\omega_\mathrm{C} = \frac{q\,B}{m}. \tag{2.16}$$

The particle therefore moves (without additional external forces) in a circular orbit in the plane perpendicular to the magnetic field lines. The absolute value of the velocity component $v_\perp$ perpendicular to the magnetic field B is constant. The orbit radius is the so called Larmor radius ρ_L:

$$\rho_\mathrm{L} = \left|\frac{v_\perp}{\omega_\mathrm{C}}\right| = \left|\frac{m\,v_\perp}{q\,B}\right|. \tag{2.17}$$

If a velocity component parallel to the magnetic field is superimposed on the gyration movement, the guiding center of the circular movement follows the course of the field line of the magnetic field. If the Larmor radius and the gyration frequency are known, the movement of the particle is determined by the trajectory of the guiding center. If one looks towards the magnetic field lines, ions move clockwise and electrons move counterclockwise [3].

Waves in Cold Plasma

In order to describe to what extent the trajectories of the plasma particles are affected by external influences, it is necessary to consider wave propagation in the plasma medium. There is a whole zoo of wave types in plasmas. A classification into wave types is difficult because in the plasma there are electromagnetic waves that change the medium (the dielectric plasma), and, as in gas, there are also sound waves that can propagate through pressure disturbances [3]. Both are mutually dependent because the particles carry a charge. Therefore a pressure disturbance has an effect on charge densities and therefore on the dielectric properties and vice versa. Influencing factors that play a major role in the course of the work regarding wave propagation in plasma are external magnetic fields and wave types that depend on the direction of propagation and polarization. More detailed overviews of sound waves, electrostatic waves and electromagnetic waves in warm and cold plasmas in a wide frequency range can be found in literature [3]. We will focus on relevant phenomena below. This includes the propagation of (transversal) electromagnetic waves in a stationary magnetic field, i.e., a magnetized plasma. Furthermore, we are assuming a cold plasma, which means that we do not need to take pressure effects into account in the following. Furthermore, we want to consider the irradiation of the waves both parallel and perpendicular to the external magnetic field, since both come into play in the case of the SLAN. In case of an unmagnetized, cold plasma, the dielectric tensor is a simple scalar function of the frequency whereas in the case of an external, stationary magnetic field in which the plasma is located the situation is more complicated [3]. In the latter case, the wave propagation depends on whether it runs parallel or perpendicular to the external magnetic field. The dielectric tensor is defined by a linearization of the Maxwell's equations, which shall be given here as a reminder and notation orientation:

$$\vec{\nabla} \cdot \vec{B} = 0, \tag{2.18}$$

$$\vec{\nabla} \cdot \vec{E} = -\Delta\phi = \frac{\rho}{\epsilon_0}, \tag{2.19}$$

$$\vec{\nabla} \times \vec{E} = -\frac{\partial \vec{B}}{\partial t}, \tag{2.20}$$

$$\vec{\nabla} \times \vec{B} = \mu_0 \vec{j} + \frac{1}{c^2}\frac{\partial \vec{E}}{\partial t}. \tag{2.21}$$

For the linearization, the waves are set up as disturbances that superimpose the ground state, so all parameters $(\vec{E}, \vec{B}, \vec{v}, ...)$ are superimposed by these disturbances. The linearized Maxwell equations are then formed accordingly. A determining equation for the dielectric tensor $\bar{\bar{\epsilon}}$ with i as the complex number, $\vec{k}$ the wave vector, $\vec{B}_1$, $\vec{E}_1$ as the electromagnetic (EM) wave components, c the velocity of light and ω the applied frequency is derived:

$$i\,\vec{k} \times \vec{B}_1 = -\frac{i\,\omega}{c^2}\,\bar{\bar{\epsilon}} \cdot \vec{E}_1. \tag{2.22}$$

In case of a cold magnetized plasma, the tensor has the form:

$$\bar{\bar{\epsilon}} = \begin{bmatrix} \epsilon_{xx} & i\epsilon_{xy} & 0 \\ -i\epsilon_{xy} & \epsilon_{yy} & 0 \\ 0 & 0 & \epsilon_{zz} \end{bmatrix}, \tag{2.23}$$

where

$$\epsilon_{xx} = \epsilon_{yy} = 1 + \frac{\omega_{\mathrm{pe}}^2}{\omega_{\mathrm{ce}}^2 - \omega^2} + \frac{\omega_{\mathrm{pi}}^2}{\omega_{\mathrm{ci}}^2 - \omega^2}, \tag{2.24}$$

$$\epsilon_{xy} = \frac{\omega_{\mathrm{ce}}}{\omega} + \frac{\omega_{\mathrm{pe}}^2}{\omega_{\mathrm{ce}}^2 - \omega^2} - \frac{\omega_{\mathrm{ci}}^2}{\omega} \frac{\omega_{\mathrm{pi}}^2}{\omega_{\mathrm{ci}} - \omega^2}, \tag{2.25}$$

$$\epsilon_{zz} = 1 - \frac{\omega_{\mathrm{pe}}^2}{\omega^2} - \frac{\omega_{\mathrm{pi}}^2}{\omega^2}. \tag{2.26}$$

The frequency-dependent expression for the elements of the dielectric tensor contains the plasma frequencies ω_{pe}, ω_{pi} for the ion and electron species, as well as the gyration frequencies of electrons and ions ω_{ce}, ω_{ci}.

This dielectric tensor $\bar{\bar{\epsilon}}$ can be used to set up wave equations for the cold, magnetized plasma. In the case of a wave propagation parallel to the magnetic field, one obtains a right and a left circularly polarized wave as solutions which can propagate inside the plasma [3]. The associated dielectric constants for the R and L waves then follow:

$$\epsilon_{\mathrm{R}} = \epsilon_{xx} + \epsilon_{xy}, \tag{2.27}$$

$$\epsilon_{\mathrm{L}} = \epsilon_{xx} - \epsilon_{xy}. \tag{2.28}$$

Furthermore, in case of high frequencies, $\omega \gg \omega_{\mathrm{ci}}$, the drift motions are dominated by electrons. Therefore, the ion term in the dispersion relations can be neglected [3]. The dispersion relations of the R and L wave in case of a cold, magnetized plasma, where the wave propagates parallel to the magnetic field, therefore reads:

$$k_{\mathrm{R}} = \frac{\omega}{c}\sqrt{1 - \frac{\omega_{\mathrm{pe}^2}}{\omega(\omega - \omega_{\mathrm{ce}})}}, \tag{2.29}$$

$$k_{\mathrm{L}} = \frac{\omega}{c}\sqrt{1 - \frac{\omega_{\mathrm{pe}^2}}{\omega(\omega + \omega_{\mathrm{ce}})}}. \tag{2.30}$$

The corresponding dispersion relations are plotted in Figure 1 on the left. At very high frequencies in such a plasma, drifts play a minor role and the response of the electrons is dominated by the Coulomb force parallel to the electric field of the EM wave [3]. In the case of the R wave, the electrons gyrate in the same direction of rotation as the field vector. In case of the L wave, the electrons gyrate in the opposite direction. The effective wave frequency that the electrons sense is therefore increased in case of the R wave [3]. As the frequency decreases, one first approaches the cut-off frequency of the R wave, which means that the R wave can no longer propagate inside the plasma, whilst the L wave still can. However, the R wave appears again below the electron sound speed. In the lower frequency range, the field vector rotates in phase with the electrons. As a result, they are continuously accelerated, so the wave gives off its energy to the electrons and gets absorbed, which is why this branch is also often referred to as the electron cyclotron wave branch [3].

If the EM wave is irradiated into a cold plasma perpendicular to an applied static magnetic field, a distinction is made between the ordinary (O) and extraordinary (X) waves. Here the O-wave refers to the situation where the electric field of the wave is parallel to the external magnetic field and the X-wave to that where the electric field oscillates perpendicular to the magnetic field lines [3]. The latter situation is especially interesting for the configurations in this work. The dispersion relation of the O wave is the same as the field-free dispersion relation. For the X wave it holds:

$$N^2 = \frac{2\,\epsilon_{\mathrm{R}}\epsilon_{\mathrm{L}}}{\epsilon_{\mathrm{R}} + \epsilon_{\mathrm{L}}}. \tag{2.31}$$

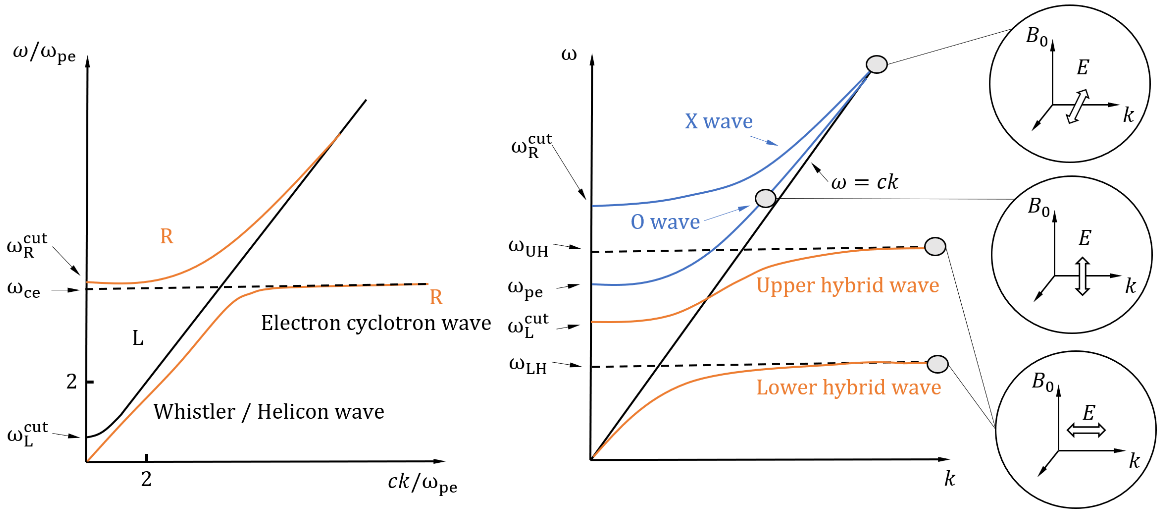

Figure 1: On the left, dispersion relation for transversal waves in a cold, magnetized plasma for the wave vector $\vec{k}$ parallel to the magnetic field ($\vec{k} \parallel \vec{B}$). The right and left cut off frequency are shown. The ranges for Whistler / Helicon waves as well as the electron cyclotron wave are depicted. The electron cyclotron wave corresponds to the right circularly polarized wave approaching asymptotically the electron cyclotron frequency. On the right, one can see the dispersion relation for the wave vector orthogonal to the magnetic field ($\vec{k} \perp \vec{B}$). The branches for the X and O-wave are shown, as well as the upper and lower hybrid wave. Additionally the oscillation direction of the electric field of the EM wave is indicated. Adapted from Ref. 3.

Here too, a dispersion relation of the X wave can be established for the case of high frequencies (electron waves, $\omega \gg \omega_{\mathrm{ci}}$):

$$k = \pm\frac{1}{c}\sqrt{\frac{(\omega^2 - (\omega_{\mathrm{L}}^{\mathrm{cut}})^2)(\omega^2 - (\omega_{\mathrm{R}}^{\mathrm{cut}})^2)}{\omega^2 - \omega_{\mathrm{UH}}^2}}. \tag{2.32}$$

For very high frequencies, the dispersion relation of a vacuum wave, i.e. a linearly polarized transverse wave, follows again. The upper hybrid frequency $\omega_{\mathrm{UH}} = \sqrt{\omega_{\mathrm{pe}}^2 + \omega_{\mathrm{ce}}^2}$ and the lower hybrid frequency as $\omega_{\mathrm{LH}} \approx \sqrt{\omega_{\mathrm{ce}}\omega_{\mathrm{ci}}}$ are shown in Figure 1 on the right. The upper hybrid frequency lies above the plasma and gyration frequency and is therefore independent of ion dynamics [3]. The lower hybrid frequency, however, is very much determined by ion dynamics. The X wave does not exist in the range between the lower hybrid frequency and the right cut-off. Only below the upper hybrid frequency, the sign changes and both the upper and lower hybrid frequencies can be observed [3]. It must also be mentioned that in the case of the X wave with a magnetic field gradient along the direction of incidence, it is important whether one irradiates from the low-field side or the high-field side of the magnetic field. In the case of irradiation from the low-field side, the X wave is reflected at the R-cutoff and never reaches the cyclotron resonance. It is therefore only possible to radiate the X wave from the high-field side for heating [3].

Forces on Particle Trajectories

How can we accelerate the plasma and exhaust it to produce thrust? Equation 2.15 described the motion of a charged particle in a static and homogeneous magnetic field. If we now set up an arbitrary force acting on that particle in such a magnetic field $\vec{B}$, the drift motion $\vec{v}_{\mathrm{D}}$ of the particle's guiding center in a magnetic field can be written as:

$$\vec{v}_{\mathrm{D}} = \frac{\vec{F} \times \vec{B}}{qB^2}. \tag{2.33}$$

An important example is the drift resulting from the Coulomb force $q\vec{E}$ when an electric field acts on the charge carriers. It results in the so-called $E \times B$ drift:

$$\vec{v}_{\mathrm{E\times B}} = \frac{\vec{E} \times \vec{B}}{B^2}. \tag{2.34}$$

If gradients in the magnetic field are present, these inhomogenities in the stationary field can also have force effects on the particle dynamics. A spatial variation of the magnetic flux density parallel or perpendicular to the magnetic field lines leads to so-called gradient or curvature drifts. In this work especially the effect of gradients in the magnetic flux density parallel to the magnetic field lines are relevant. If the field strength of the magnetic field increases along the magnetic field lines, this arrangement is known as the magnetic mirror or magnetic bottle. Such a magnetic field topology and its effect on electron dynamics can be seen in Figure 2. Assuming that the magnetic field is rotationally symmetrical and increases along the z axis, curved magnetic field lines automatically result. This means that the field strength decreases in the direction of the radius of curvature. This gradient together with the curvature of the magnetic field lines leads to an azimuthal drift. This motion is to be distinguished from gyration around the single magnetic field line, as gyration is not a drifting of the center of guidance. The particles therefore additionally precess around the axis of symmetry of the configuration besides the gyration motion, compare Figure 2. Following from divergence-free condition of the magnetic field, it is described in cylindrical coordinates by:

$$B_{\mathrm{r}}(r, z) \approx -\frac{r}{2}\frac{\partial B_{\mathrm{z}}}{\partial z}. \tag{2.35}$$

Therefore, the equation of motion of a particle follows as:

$$\begin{aligned} m\dot{v}_{\mathrm{z}} &= -qv_\theta B_{\mathrm{r}} \\ &= qv_\theta \frac{r}{2}\frac{\partial B_{\mathrm{z}}}{\partial z}. \end{aligned} \tag{2.36}$$

With the Larmor radius definition, Eq. 2.17, the equation of motion in a magnetic mirror configuration yields:

$$m\dot{v}_{\mathrm{z}} = -\frac{\frac{1}{2}mv_\perp^2}{B}\frac{\partial B_{\mathrm{z}}}{\partial z}. \tag{2.37}$$

Generalized to a non-axial field line, the equation of motion can be formulated as:

$$m\dot{v}_{||} = -\mu\nabla_{||}B. \tag{2.38}$$

Here the magnetic moment $\mu = \frac{1}{2}mv_\perp^2/B$ of the charged particles (forming due to the gyration of the particles about the magnetic field lines) and the mass of the particle m, is used to formulate the acting force. So, all-together the inhomogenity of the magnetic field parallel to the magnetic field lines, leads to an acceleration ($\dot{v}_{||}$) opposite to the gradient direction $\nabla_{||}B$, compare Eq. 2.38 [3, 20]. This magnetic field topology reveals one of the most important aspects of a MN. If one allows the character of a divergent magnetic field, electrons and ions are accelerated in a direction opposite the gradient direction, i.e. in the direction of a weak magnetic field towards the outside of the thruster. This acceleration process is made possible without any electrodes exposed to the plasma. However, as mentioned above, many magnetic nozzle designs cover converging-diverging character of the magnetic field lines. The same gradient force that accelerates the plasma in the diverging part can cause particles to decelerate and even reflect in the converging sections of a MN. This phenomenon, known as the magnetic mirror effect, has been the subject of investigation in several recent studies

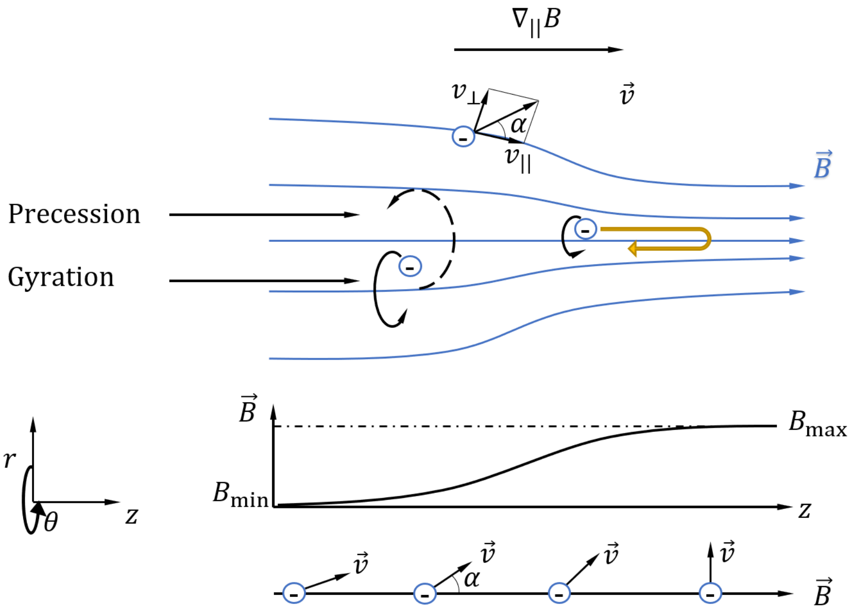

Figure 2: Magnetic field configuration forming a magnetic mirror. The converging magnetic field lines are depicted in blue on the top. The direction of the magnetic field gradient, parallel to the magnetic field lines $\nabla_{||}B$, is shown above. The charged particle - in this case an electron - is indicated as well as its path, exhibiting a gyration motion about the magnetic field lines, and an azimuthal precession about the symmetry axis of the configuration. The gyration motion is shown as a solid line, the precession is shown as a dashed line. A second exemplary electron is shown with the velocity components $v_{||}$ and $v_\perp$, together with their pitch angle α. The reflection at the 'bottleneck' of the magnetic mirror is indicated as a yellow arrow. At the bottom the cylinder coordinate system is shown, with the azimuthal angle θ. A quantitative description of the magnetic flux density, based on the magnetic field topology above, is depicted as well. The field strength increases along the z-axis from the minimum magnetic flux density B_{min} to the maximum field strength B_{max}. Below the depicted gradient, its effect on the velocity of the electron is shown schematically. With an increase in magnetic field strength, the parallel velocity is transformed into perpendicular velocity. If the mirror condition is fulfilled, the particle is reflected, as indicated with the yellow arrow. Adapted from Ref. 3.

aimed at modeling MN behavior [11, 12, 48, 49]. Depending on the magnetic field ratio (the ratio of maximum field strength to minimum field strength, $B_{\mathrm{min}}/B_{\mathrm{max}}$), a critical pitch angle α leading to particle reflection can be determined [3]:

$$\sin\alpha > \sqrt{\frac{B_{\mathrm{min}}}{B_{\mathrm{max}}}}. \tag{2.39}$$

The pitch angle is defined by the parallel and orthogonal velocity components of the particle ($\tan\alpha = v_{\perp}/v_{||}$). Thus, in a convergent–divergent MN, just particles with a sufficiently high energy in parallel direction can leave the converging part to be accelerated in the diverging part of a MN. Due to their lower mass, electrons follow the acting gradient force faster than ions, leading to a charge separation and therefore to a self-consistent electrostatic field, also called ambipolar field, since it is acting on both electrons and ions alike. The axial motion of individual ions or electrons is therefore governed by both electrostatic and magnetic mirror forces [11]. While the electrostatic field accelerates ions and decelerates electrons axially in the convergent and divergent MN regions, the magnetic mirror force decelerates both ions and electrons in the convergent part and accelerates them axially in the divergent part. The electron response, in particular their temperature, plays a fundamental role in the set up of the electrostatic field in the plume, which is then in return responsible for the ion acceleration [11]. Plasma detachment, involving the electromagnetic exiting of ions and electrons, ultimately produces the thrust. This process can be explained in two ways. Either by frozen-in magnetic flux, according to ideal MHD theory for plasmas of sufficiently high density [50]; or by plasma detaching as soon as the ion gyromagnetic radius is equal to the radius of the plasma cross section and the ions are assumed to demagnetize [30]. The latter is most likely to be the dominating process in case of EP plasma, due to the typical plasma densities of about 10^{13} to $10^{17}\,\mathrm{m}^{-3}$. The detachment process however is not well understood yet.

2.2. Experimental Set Up

We now discuss the technical realization of a plasma thruster. We want to investigate; What kind of technology in the microwave regime is necessary for the realization of an ECR thruster with MN? How was an ECR plasma thruster with MN realized in previous studies? What was the outcome of previous thruster development, and what challenges remain? How can we circumvent these challenges?

2.2.1. Prototypes under Investigation

Elements of Microwave Engineering

The thruster prototypes discussed rely on ECR excitation of the plasma with frequencies in the microwave range. We have the opportunity to build upon prior research, particularly on the MINOTOR prototype, which allowed us to leverage existing microwave engineering expertise from the corresponding ONERA research group. Thus, we aim to advance this work further. In this section, we provide insights into the essential connections between plasma generation and microwave engineering, crucial for comprehending our research efforts.

Waveguides, Transitions and Modes

In a broader sense, a waveguide serves as a pathway for directing electromagnetic waves, along a specific direction. This guidance can be provided by a rectangular shaped pipe, consisting of a conducting material, or a circular hollow pipe. For the purposes of our discussion, we are considering waveguides filled with a uniform, isotropic dielectric material or vacuum. Detailed descriptions are provided for two specific types of waveguides: a coaxial waveguide and a circular waveguide structure. These waveguide configurations will play a significant role in the analysis conducted in this study. We also want to take a look at the coaxial to waveguide transition, as this transition is excessively used in our investigations.

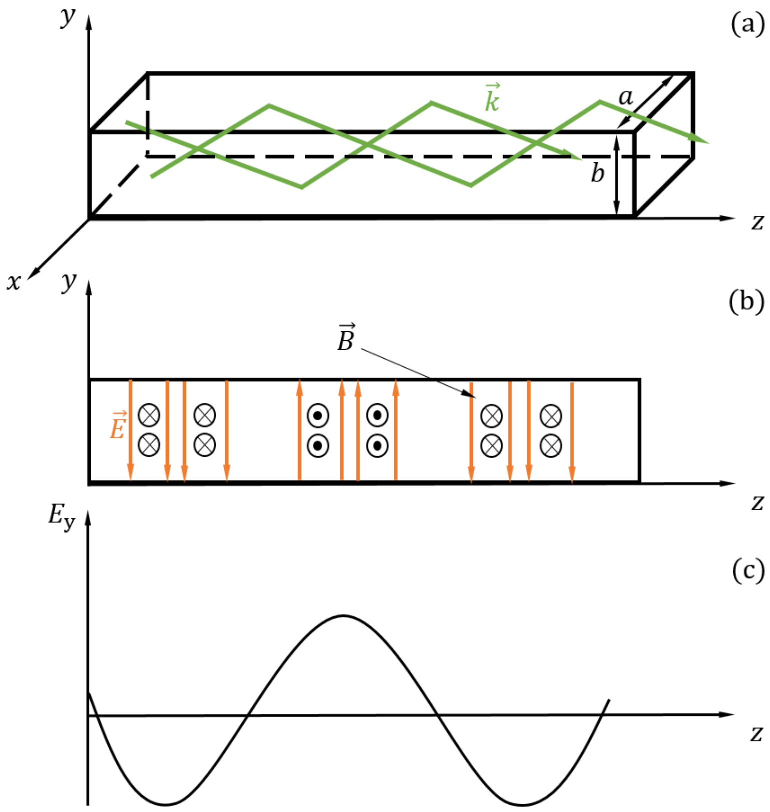

Figure 3: Propagation of an electromagnetic wave in a rectangular waveguide. On the top (a) one can see the propagation direction $\vec{k}$ in green of the incident electromagnetic waves in the rectangular pipe with the dimensions a and b in x, y direction. The reflection at the walls at $x = -a$ and $x = 0$ is shown. In (b) the cross section and a resulting mode is shown with the electric field $\vec{E}$ indicated in orange and the magnetic field $\vec{B}$ in black. The electric field strength in y direction E_y is additionally shown in (c).

Electromagnetic waves can always be described by Maxwell's equations (see Eq. 2.21). The reflection and transmission of electromagnetic waves inside a waveguide and therefore the establishment of modes within a waveguide follow from solving the Maxwell's equations for given boundary conditions. As an example compare Figure 3: Imagine a long pipe with a rectangular cross section of the dimensions in width a in x direction and height b in y direction. When a plane EM-wave strikes one of the narrow sides perpendicularly (hits the wall at $x = 0$ or $x = -a$), it bounces back and forth between the two walls, creating a standing wave. If the distance between the walls is decreased, the wave can only propagate at a specific angle, creating a different standing wave between the walls. This circumstance is shown in Figure 3 on the top. The minimum width a of a rectangular waveguide corresponds to approximately half the wavelength of the transmitted frequency, precisely when only a single maximum in the transverse direction (x) fits into it. Thus, the width a of a rectangular waveguide can serve as a determinant for the lowest frequency utilized in the associated device. This critical wavelength is termed as cutoff wavelength. It can be estimated using the relation $\lambda = 2a$, where a represents the longer side of the rectangular waveguide cross section [51, 52].

Important solutions of the arising modes within waveguides are the following:

Firstly, the so called TEM mode (transversal electromagnetic mode). The TEM mode can propagate at any frequency and is characterized by the same dispersion relation as waves in free space/vacuum. There is no electric or magnetic field component present in propagation direction of the wave(-

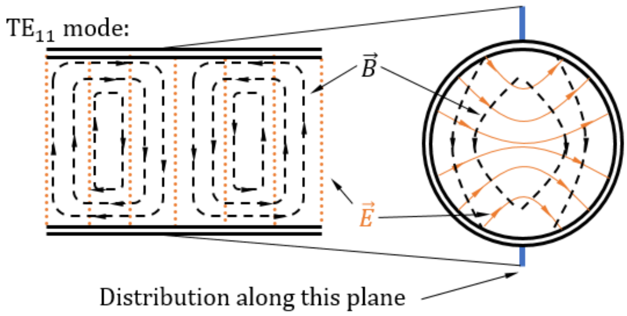

Figure 4: TE_{11} mode in a circular waveguide. On the left, cross section with the mode forming. The electric field lines are indicated in orange, the magnetic field lines in black. On the right, front plane of the circular waveguide, again with the electric field lines in orange and the magnetic field lines in black.

packages). In electromagnetic waves, the electric and magnetic fields are invariably perpendicular to each other. For waves to propagate in a spatial direction in a waveguide, electric or magnetic field components of the wave can exist in that spatial direction. When the electric field is perpendicular to the direction of propagation, they are termed H waves or TE mode (transversal electric mode). Conversely, when the magnetic field is perpendicular to the propagation direction, they are denoted E-waves or TM mode (transversal magnetic mode). To describe a mode in a waveguide, it is necessary to specify two numbers, the mode order: e.g. (2,3) mode. The first number represents the number of maxima of the transversal component (E or H in x direction in Figure 3), the second number 3 represents the number of maxima of respectively the parallel component maxima (E or H in y direction in Figure 3) [51, 52, 53].

We want to start with the description of a coaxial waveguide offering a compact, shielded, and flexible means to guide microwaves. In such coaxial waveguides (cables) electromagnetic waves propagate between two cylindrical conductors, primarily supporting the TEM mode [23]. However, it can also sustain TE and TM modes above a certain cutoff frequency. Within a coaxial line, the amplitude of TEM electromagnetic fields exhibits rotational symmetry and is inversely proportional to the radius. The electric field is oriented radially, while the magnetic field adopts an azimuthal orientation [23]. For an empty coaxial line (magnetic and electric permeability μ,ϵ=1) at frequency $f = 2.45\,\text{GHz}$, the wavelength is given as $\lambda = 1/(f\sqrt{\mu\epsilon}) = 12.24\,\text{cm}$.

In case of a circular waveguide, the modes result from the Bessel function and its derivatives as well as zero points, with which the possible propagation of H and E waves for the circular waveguide can be determined [23]. The fundamental mode of the circular waveguide is the TE_{11} mode, see Figure 4. Here the wavelength of frequency $f = 2.45\,\text{GHz}$ is determined to be $\lambda = 22.22\,\text{cm}$.

A number of different techniques can be used to achieve coupling between different types of waveguides [23]. The coaxial-to-waveguide transition is a way to couple a waveguide to a coaxial line by connecting the outer conductor of the coaxial line to a wall of the waveguide and having the inner conductor extend into the waveguide volume. This type of transition is used in the transmission line from generator to thruster, for all the DEEVA prototypes as well as for the MINOTOR prototype in use, see Figure 5. A common coaxial-to-waveguide transition geometry is also shown in Figure 5 together with a schematic of the microwave coupling in case of MINOTOR [23]. The lengths of the coaxial launchers, as well as the sizes of the waveguides and MINOTOR prototype are based on the operation frequency of $f = 2.45\,\text{GHz}$ and are also shown in Figure 5.

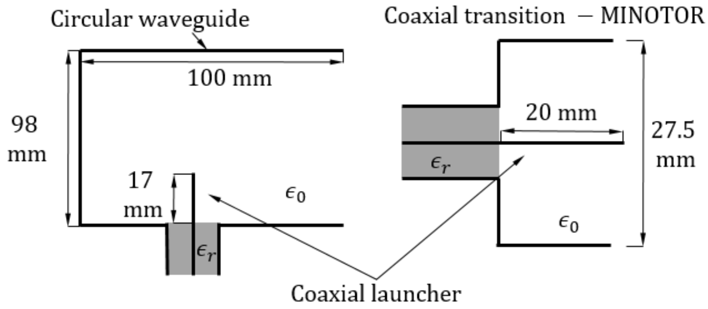

Figure 5: Coaxial to waveguide transition, adapted from Ref. 23. On the left, circular waveguide for the transmission line with lengths given in the drawing. The coaxial microwave launcher on the bottom is fed into the circular waveguide with a N-type socket on which a copper antenna is soldered or pressed within a dielectric material with the permittivity ϵ_r. The modes develop and can be received by an identical circular waveguide, and therefore translate the waveguide microwave signal back to a coaxial one. On the right, a coaxial to waveguide transition as the transition is realized in case of the MINOTOR prototype. The relevant lengths are given in the drawing.

Slot Antenna Design

One method to distribute homogeneous microwave power over a large area is the use of power radiation from large-area antennas, especially slot antenna matrices. A slot antenna has a radiation characteristic that is the verse to that of a dipole antenna, a schematic drawing can be seen in Figure 6 [42].

Slot antenna applicators can have a linear, a rectangular, a circular; or the, for our case relevant, annular geometry. The diameter of the ring cavity is chosen such as to develop a standing electromagnetic TE_{10} wave inside the center cavity [42]. The circumferential length of the middle line of the cavity is about $n\lambda$, where λ is the waveguide wavelength and n an integer. The precise dimensions of the ring cavity were optimized on the basis of a COMSOL simulation. On the inner side of the ring cavity, there are n (in our case 2) resonant coupling slots, about half of a free-space wavelength long (6.12 cm), equally spaced azimuthally and axially directed (i.e. perpendicular to the direction of wave propagation within the waveguide). In the ideal case the nodes of the electric field will be at the positions of the slots. Oscillation of this field gives rise to a magnetic field along the slots [42]. In this case each slot, acts as a slot antenna, receiving and radiating the EM signal into the application space. A field pattern with a maximum electric field between the slot antennas is established in the application space (where the glas tube and then the plasma is located). The space between the application chamber (inner cylinder) wall and the plasma chamber (glas tube) wall can be treated as a coaxial waveguide [42]. When the plasma is of sufficiently high conductivity, a coaxial mode of microwave propagation TE_{m1} can develop, where m is the number of wavelengths along the quartz tube. The principal electric and magnetic field lines in such a waveguide seen from the axis of the plasma source are shown in Figure 7 [42].

Two relevant waves that can propagate within the plasma for heating in case of the SLAN antenna design can be referenced: First, there is coupling from the slots of the inner cavity. Here, the EM wave propagates inward towards the center of the cylinder. The electric field component is perpendicular to the thruster's centerline. Combined with the magnetic field topology, this results in the R wave. The second type of wave propagation is through the waveguide or coaxial waveguide. In this case, the wave travels along the thruster's centerline, parallel to the magnetic field lines. The only usable component for heating is the electric field component perpendicular to the wave propagation direction, which is also perpendicular to the magnetic field lines. This is known as the X wave.

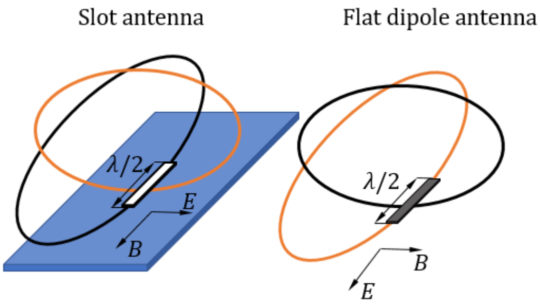

Figure 6: Slot antenna radiation characteristic. On the left, radiation pattern of a slot antenna. The electric field is indicated in orange, the magnetic field component is shown in black. On the right, the signal pattern of a dipole antenna. The radiation patterns of a slot and a dipole antenna are very similar, only the electric and magnetic field components of the electromagnetic wave are switched.

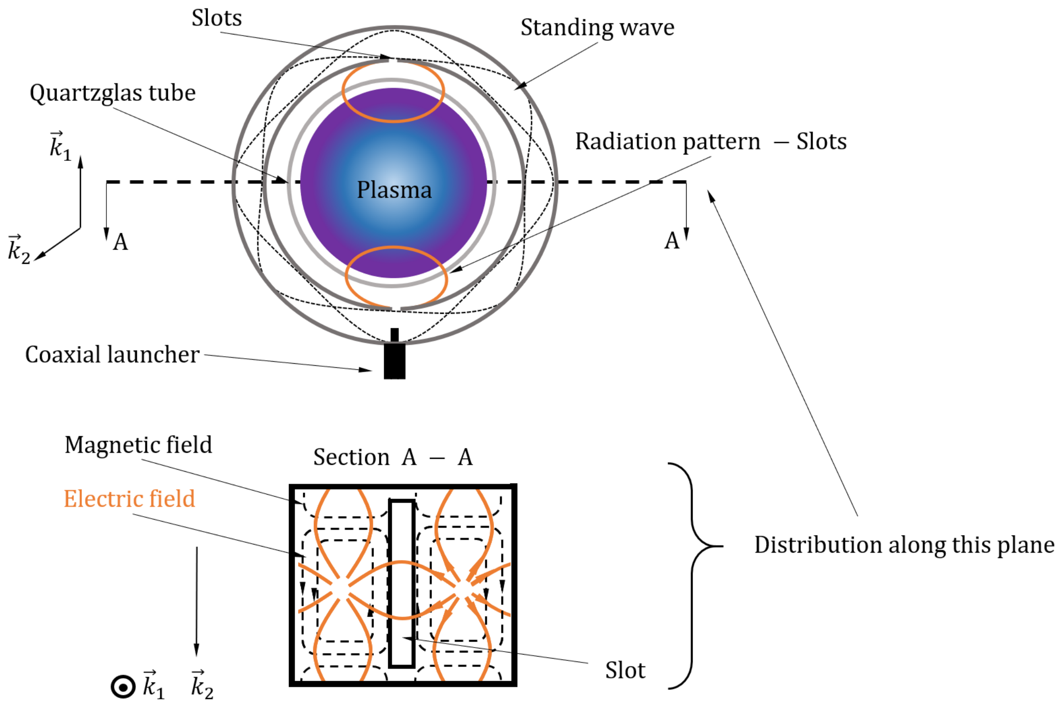

Figure 7: Electromagnetic fields in SLAN. On the top, the front view of the SLAN. The signal is fed into the space between the cylinders by the coaxial launcher (in black). Between the outer and inner aluminum cylinder the standing waves / the electromagnetic modes developing are indicated in gray. The slots in the inner aluminum cylinder and the quartzglas tube with the plasma in the center can be discerned. Furthermore, the electric field of the radiation pattern of the slot antenna is shown in orange. At the bottom, a cross section of the cylinders can be seen with the modes developing in the inner cylinder. The TE_{11} pattern for one slot is shown as an example. The electric field is indicated in orange, the black dashed line shows the magnetic field component of the mode. The wave vectors $\vec{k}_1$ and $\vec{k}_2$ correspond to the wave propagation direction in the slot antenna signal and to the TE_{11} mode in the waveguide, respectively.

Thruster Prototypes

We now come to the answers to the questions: How was the realization of an ECR plasma thruster with MN in previous studies? What were the outcomes of this earlier thruster development, and what challenges remained?

MINOTOR prototype

One of the thruster concepts under investigation is a MINOTOR prototype. It can be seen as photograph and schematic drawing in Figure 8. The chosen dimensions of the MINOTOR prototype investigated are motivated by the wavelength chosen for excitation, therefore optimized for 2.45 GHz [35]. The inner diameter of the thruster is given as 27 mm and an antenna made out of stainless steel of 20 mm length, serving as a long semi-open coaxial coupling structure, see also Figure 5 [35]. The close end of the coaxial structure used to fed the microwave into the thruster is a boron nitride plate. The static and divergent magnetic field of about 87.5 mT magnetic flux density at the backwall of the thruster is created by an annular permanent magnet consisting of a neodym-iron-boron alloy (Ne-Fe-B) [35, 54]. The electromagnetic wave is fed to the antenna of the thruster via a coaxial to waveguide transition. The two hollow cylinders have a length of 100 mm respectively. The connection to the coaxial cable from the microwave generator is a copper antenna reaching inside the waveguide with a length of 27 mm [34]. A second antenna of the same length is then placed in a 100 mm distance plus a slit of roughly 2 mm size in between the two cylinders in order to receive the microwave signal and radiate it inside the thruster. This assembly enables microwave feeding without mechanical or electrical coupling. This type of coupling enables the measurement of a floating potential at the conducting parts and reliable thrust measurements [35]. The thruster potential can be recorded with a hand-held multimeter. The thruster potential against ground as reference potential is measured over a time span of one minute and the mean and standard deviation is determined for each operation point.

The set up with the waveguides within the transmission line for thruster potential measurements is also possible for the DEEVA prototypes. In the results chapter if no specific reference is made whether the thruster was operated with waveguides or with cable, the MINOTOR prototype was kept in floating mode, while the DEEVA prototypes were operated in grounded mode. One statement omnipresent in former studies on the ECRT MINOTOR is the operation of the thruster in floating mode. As it is stated in Refs 55 and 56, observations indicate that the thruster potential depends on the electron temperature in the source and is directly proportional to the ion energy. Therefore, the possibility is created to operate the thruster prototypes in electrically floating as well as non-floating mode. We chose the ECR thruster MINOTOR to serve as reference thruster concept since its characteristics are well documented in multiple publications [23, 28, 29, 33, 34, 35, 57, 58, 59, 60, 61, 62].

State of the Art and Earlier Studies

MINOTOR prototypes with dimensions comparable to those given above were tested and simulated in various ways at different operational conditions. Within the framework of the study by Correyero Plaza *et al.*, various operating points were tested, such as different volume flow of $0.5 - 2.5$ sccm, microwave frequencies of 2.45 GHz $\pm$ 200 MHz and excitation powers of $15 - 60$ W with a background pressure of $3 \cdot 10^{-7}$ mbar [34]. The values given in Table 1 are excerpts from various publications and are determined with xenon and argon as the propellant. The volume flow in all cases was about 1 sccm in xenon case and up to 4 sccm for argon. Prototypes with permanent magnets (PM) were tested as well as prototypes where the magnetic field was provided by coils or solenoids. A variety of diagnostics at varying distances from the thruster have been used to characterize plasma and beam. The experimental results relevant to this work summarized in Table 1 give an idea of the magnitudes of plasma and plume parameters to be expected for both, the MINOTOR and the DEEVA prototypes.

With a single Langmuir probe in a minimum distance of 55 mm the electron energy probability function (EEPF), the second derivative of the Langmuir characteristic, was determined. This provided infor-

Thruster set up		Diagnostics and Results					Reference
Magnetic field	Propellant	LP	FP	TB	Ion energy analyzer	Thruster potential	
PM	Xenon	$T_{\mathrm{e}} \approx 20$ to $30\,\mathrm{eV}$	$J_{\mathrm{i,max}} \approx 80\,\frac{\mu\mathrm{A}}{\mathrm{cm}^2}$				[33]
		$n_{\mathrm{e}} \approx 10^{15}\,\mathrm{m}^{-3}$					
Solenoid	Xenon	$T_{\mathrm{e}} \approx 10$ to $30\,\mathrm{eV}$					
		$n_{\mathrm{e}} \approx 10^{15}\,\mathrm{m}^{-3}$					
Coils	Xenon	$T_{\mathrm{e}} \approx 12$ to $27\,\mathrm{eV}$			$E_{\mathrm{i}} \approx 50$ to $150\,\mathrm{eV}$	$\Phi_{\mathrm{TW}} \approx 30$ to $40\,\mathrm{V}$	[56]
PM	Xenon		$J_{\mathrm{i,max}} \approx 40\,\frac{\mu\mathrm{A}}{\mathrm{cm}^2}$	$T_{\mathrm{T}} \approx 0.3$ to $0.9\,\mathrm{mN}$*	$E_{\mathrm{i}} \approx 80$ to $320\,\mathrm{eV}$		[63]
			$I_{\mathrm{beam}} \approx 80\,\mathrm{mA}$				
PM	Argon		$J_{\mathrm{i,max}} \approx 60\,\frac{\mu\mathrm{A}}{\mathrm{cm}^2}$	$T_{\mathrm{T}} \approx 0.3$ to $0.5\,\mathrm{mN}$*	$E_{\mathrm{i}} \approx 80$ to $200\,\mathrm{eV}$		
			$I_{\mathrm{beam}} \approx 65\,\mathrm{mA}$				
PM	Xenon			$T_{\mathrm{T}} \approx 0.45$ to $0.9\,\mathrm{mN}$			[54]
PM	Xenon		$I_{\mathrm{tot}} = 45.5\,\mathrm{mA}$	$T_{\mathrm{T}} = 0.98\,\mathrm{mN}$	$E_{\mathrm{i}} = 248.5\,\mathrm{eV}$		[32]
PM				$\eta_{\mathrm{T}} = 16.1\,\%$			

Table 1: Excerpt of plasma characteristics of MINOTOR prototypes from literature. The thruster set up with the gas used is shown on the left. The results of the employed diagnostics are shown with the reference given on the right. LP stands for Langmuir probe, FP for Faraday probe, TB for thrust balance. $T_{\mathrm{e}}, n_{\mathrm{e}}$ are the electron temperature and density, respectively; $J_{\mathrm{i,max}}$ and I_{beam} the current density and total current of the beam, respectively; E_{i} is the mean ion energy; T_{T} is the determined thrust. The star at the thrust value refers to the determination of the force value via probe measurements. The thrust efficiency determined is shown as η_{T}, and the thruster potential as Φ_{TW}.

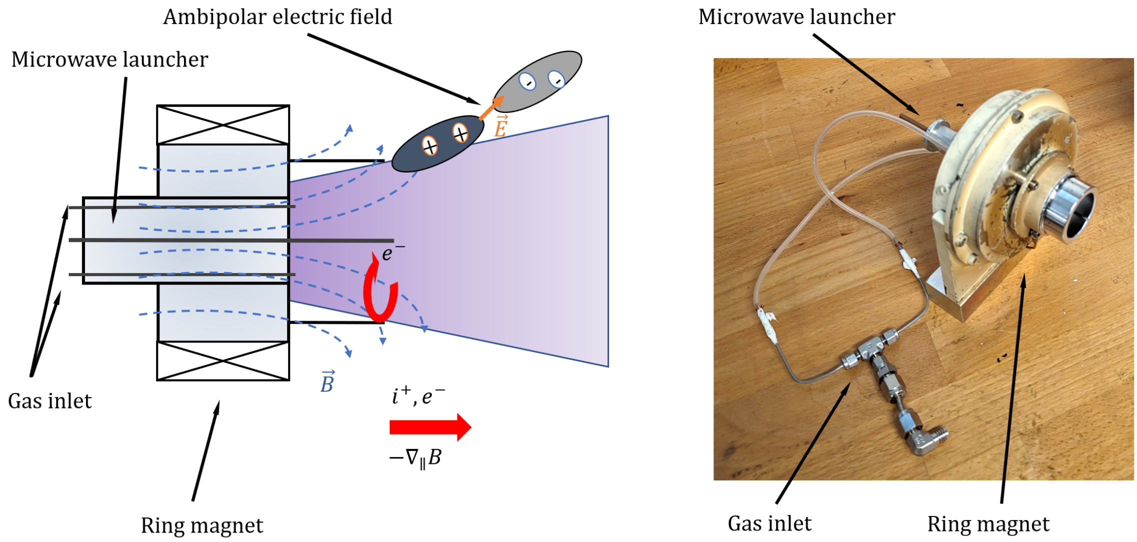

Figure 8: MINOTOR prototype under investigation. On the left, a schematic of the prototype. The thruster structure is pictured in black. The magnetic field lines are depicted in blue, and the particle motions are indicated in red. The ambipolar electric field is indicated in orange. Additionally, the gas inlet, the ring magnet and the microwave launcher are shown.

mation about the velocity distribution, whether a Maxwell-velocity-distribution was present (compare Eq. 2.5) [33, 34]. The two values for the electron temperature gained in that study

$$T_e = \begin{cases} 8\,\mathrm{eV} & \textit{low} \\ 30 \pm 2\,\mathrm{eV} & \textit{high} \end{cases}$$

refer to the two prevailing electronic temperatures. The fact of two electron temperatures present speaks against a Maxwell-velocity-distribution of the electrons in the plasma. In rarefied gases or plasmas in our density ranges, temperatures are to be interpreted as velocity dispersions. These velocity dispersions in parallel or orthogonal direction with respect to the magnetic field lines is often labeled as orthogonal or parallel temperature components [11]. The plasma potential determined by Langmuir probe measurements up to $\phi_\mathrm{P} = 165\,\mathrm{V}$ as well as the electron density n_e are also additionally mentioned in Ref. 61. Similar electron temperatures were also measured by laser-induce fluorescence (LIF) and diamagnetic loop measurements [34]. LIF additionally allowed a determination of the velocity of the ions at the thruster exit, $v_\mathrm{i} \approx 2100 \pm 100\,\mathrm{m/s}$, as well as together with Faraday probe measurements the determination of the plasma density n and ion current density I_i depending on the mass flow rate [34].

The diamagnetic loop measurement allowed the determination of the perpendicular electron pressure $p_{e,\perp} \approx 4 \cdot 10^{18}\,\mathrm{eV/m^3}$. Additionally an ion energy E_i was measured with a parallel plate analyzer (PPA) [32]. With a thrust balance, the thrust T_T was measured [32]. A comparison between measured properties and a 1D steady state model for a fully divergent magnetic field, assuming quasi-neutrality, current-free expansion and ions treated as a cold fluid species, was possible and delivered comparable results [61].

The connection between ion energy and electron temperature in a magnetic nozzle, more precisely in the magnetic field of a MINOTOR prototype was also investigated. As reported in Lafleur *et al.*, stronger magnetic fields resulted in smaller ion energy to temperature ratios, according to a non-Maxwellian kinetic model and Faraday probe measurements [56]. Furthermore, it was concluded that the magnetic field does not cause additional ion acceleration in the downstream region of the nozzle, as evidenced by the fact that ion energy values remained high even with the magnetic field turned off [56]. In these studies, the ratio of electron temperature to maximum ion energy often exhibited a relatively constant value. Specifically, in the absence of a magnetic nozzle, a ratio of 7 was observed, while stronger magnetic fields led to a ratio of about 4. Ion energies were measured in the range of 150 eV, with electron temperatures exceeding 20 eV [56].

The good performance values of the MINOTOR thruster have increasingly supported the development of other ECRTs with MN. However, a significant challenge remains in the coaxial design of many prototypes: the inner conductor is directly exposed to the plasma. Over time, this conductor shows high sputter degradation and heating effects. In the worst case, the inner conductor can even fall off. In Ref. 23, Peterschmitt therefore aimed to investigate waveguide coupling as a potential solution to mitigate the erosion problem associated with coaxial-coupled thrusters. The first step involved designing and manufacturing a waveguide-coupled thruster, with the goal of creating two identical thrusters differing only in their coupling structure. This approach allowed for a reliable comparison between the two systems. The second step involved performing experimental comparisons, focusing on ion current angular density, ion energy, and thrust balance measurements. A circular waveguide-coupled ECRT with a 27.5 mm diameter, operating at 2.45 GHz, was successfully designed. Thrust balance measurements showed a thrust of 500 µN for the coaxial-coupled thruster and 240 µN for the waveguide-coupled thruster, both operating at 25 W of deposited microwave power and a xenon mass flow rate of 0.1 mg/s. Ion energy measurements revealed that the difference in thrust can be largely attributed to a discrepancy in ion energy. For the waveguide coupled prototype Peterschmitt did not measure mean ion energies above 90 eV, while for the coaxial coupled thruster for the similar settings 260 eV were determined. The ion energies measured for the waveguide-coupled thruster led to the conclusion that the difference in ion energy is an intrinsic characteristic of the coupling method. However, for us the question arose: How can we circumvent the exposure of an inner conductor to plasma - ergo go for a waveguide coupling - while still achieving similar operation points and performance values as the coaxial reference thruster? To allow for a complete electrodeless plasma production and acceleration, we developed the DEEVA thruster design.

DEEVA prototypes

The first DEEVA prototype under investigation is the DEEVAv1 prototype, shown in Figure 9, realizing plasma ignition by microwaves using a slotted type antenna, a SLAN. In the SLAN, the microwave power is coupled from an annual waveguide (ring cavity) through two resonant coupling slots into the plasma discharge chamber made of quartz. The SLAN is made out of aluminum. It consists of two cylinders functioning as waveguides. The microwave enters the bigger cylinder via a N-type 12.7 mm long launcher made out of copper. As a result, modes develop between the inner and outer waveguide. Under certain conditions, e.g., when the two slots have a suitable angle towards the launcher (about 32°) the microwave is efficiently fed into the inner cylinder. Backplates are applied on both ends of the two cylinders. On the downstream end, a ring magnet with a remanence of 1.3 T is positioned. Typical microwave power ranges for ignition and operation lay between 10 and 100 W. The gas is fed into a quartz glas tube with a diameter of 25 mm via a 1/8″ feed-through.

The improved thruster prototype of the DEEP project, the DEEVAv2 prototype can be seen in Figure 10. Again, the microwave enters the SLAN via a N-type 12.7 mm long launcher made out of copper. As a result, modes develop between the inner and outer waveguide. When the two slots have a suitable angle towards the launcher, now $\approx 45°$, the microwave is fed into the inner cylinder. Backplates are again applied on both ends of the two cylinders. On the downstream end, a ring magnet with a remanence of 400 mT is positioned. In contrast to the DEEVAv1 prototype two disc magnets, each with a remanence of 1400 mT are located upstream. Typical microwave power ranges for ignition and operation lie between 10 and 100 W. The gas is fed into a quartz glas tube with an inner diameter of 45 mm via a in-house designed gas inlet. The gas inlet consists of two parallel plates, one without any holes and the other with 12 holes. The gas is fed into the space between the two plates and is distributed over the whole diameter of the glas tube via the holes. The magnetic field topology of DEEVAv2 can be changed by realigning the permanent magnets (the disc magnets and the ring mag-

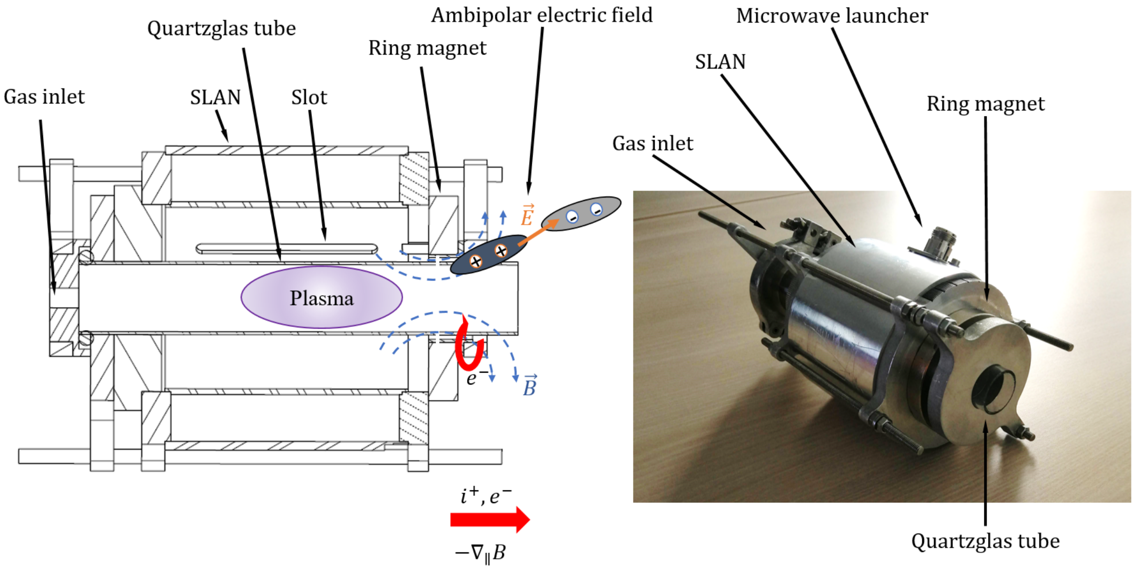

Figure 9: DEEVAv1 prototype. The slot antenna (SLAN) is indicated, it consists of two cylinders, the microwave launcher, and the slots. Furthermore, the quartz glas tube, the ring magnet and the gas inlet are shown. The magnetic field lines are pictured in blue, and the particle motions are indicated in red. The ambipolar electric field is shown in orange.

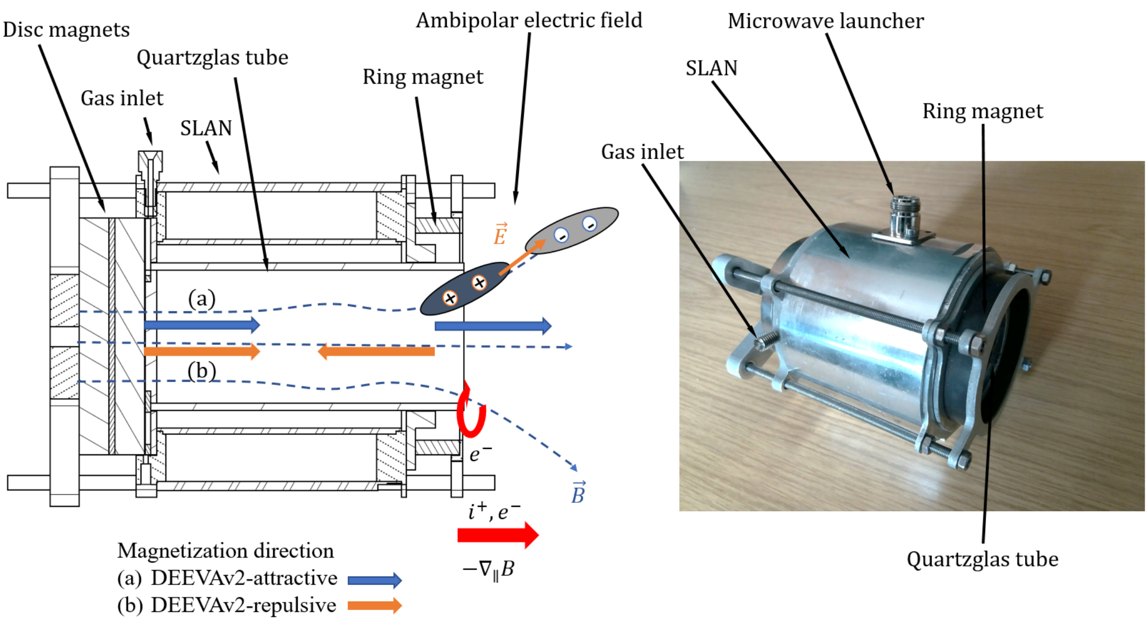

Figure 10: DEEVAv2 prototype. The slot antenna (SLAN) is indicated. It consists of two cylinders, the microwave launcher, and the slots. Furthermore, the quartz glas tube, the ring magnet, the disc magnets, and the gas inlet are shown. The magnetic field lines are indicated in blue, and the particle motions are pictured in red. The ambipolar electric field is shown in orange. The two possible configurations, DEEVAv2-attractive and DEEVAv2-repulsive, with magnetization directions parallel (a) and antiparallel (b) are indicated in blue and orange, respectively.

net), compare Figure 10. In one configuration, the disc magnets and the ring magnet are aligned in an attracting manner. This set up is referred to as *DEEVA-attractive* (case (a)). The second magnetic field set up aligns the magnets in a repulsive manner, and is therefore denoted as *DEEVA-repulsive* (case (b)). These two configurations of the DEEVAv2 prototype show different behavior regarding plasma and thrust parameters and are both discussed in the course of this work.

2.2.2. Test Facilities and Set Ups

Measurements were performed in three vacuum test facilities of different size and pumping capabilities. Facility effects are reported to have a significant influence on thruster performance [64]. Therefore, if results of the thrusters are compared, reference is been made to the chamber in which the thrusters were placed. In larger chambers with lower base pressure during thruster operation, the ion energy and, therefore, the produced thrust has higher values [32, 35, 65].

The largest vacuum chamber *Jumbo*, in which experiments are performed in the context of this thesis is located at the Justus-Liebig-University (JLU) in Giessen [66]. With a length of 6 m and a diameter of 2.6 m it allows to conduct simultaneous measurements with several diagnostic systems [66]. This vacuum chamber is equipped with cryo- and turbopumps with a pumping speed of 150000 l/s. During experiments the cryopumps are not used, leading to a base pressure between 10^{-6} and 10^{-5} mbar during operation. The second chamber, the so called *BigMac-EVO* is also located at JLU [66]. With a length of 3.2 m and a diameter of 1.6 m it allows us to conduct simultaneous measurements with several diagnostic systems, i.e., 2D-positioning systems for electrostatic probes, Faraday cups, etc. [66]. This vacuum chamber is equipped with cryo- and turbopumps to yield a base pressure in its 6.4 m^3 volume of about 10^{-6} mbar [66]. During experiments the cryopumps are used, leading to a base pressure between $2 \cdot 10^{-6}$ and $5 \cdot 10^{-5}$ mbar during thruster operation. In addition to a window (allowing optical access to the chamber) a camera is placed inside in order to observe the thruster and plasma discharge. The third and smallest chamber used in the course of this work is located at the DLR in Göttingen. The vacuum facility *Simulationsanlage für Treibstrahlen Göttingen - Miniatur Triebwerke* (STG-MT) has a length of 1.1 m and a diameter of 1 m. It is equipped with two backing pumps, a rotary vane pump and a roots pump yielding a base pressure of 10^{-3} mbar. For lower pressure ranges, a turbomolecular pump is added yielding pressures in the 10^{-6} mbar range. During thruster operation, the background pressure lies in the range of $2 \cdot 10^{-5}$ to $5 \cdot 10^{-4}$ mbar.

The distances and orientations of the diagnostic devices vary in the different chambers. Additionally not all thruster prototypes are measured in all three chambers. Therefore, the test facility will be specified for all measurement results shown and compared.

Since the magnetic field plays a decisive role in the functioning of the thruster, a mapping of all the prototypes' magnetic field topology with a Hall probe is performed. The set up of the magnetic field mapping can be seen in Figure 14.

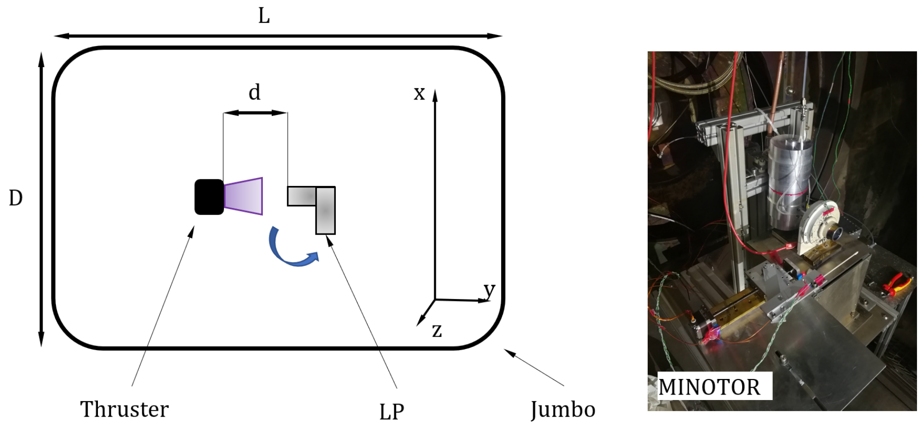

Figure 11: Test set up in JUMBO. The MINOTOR prototype with the circular waveguides can be seen on the right. The Langmuir probe (LP) in different orientations with respect to the magnetic field lines can be seen in the photograph, as well as in the schematic image on the left. The distance d between the probe tip and the thruster exit plane in this case is 6 cm. The dimensions of the vacuum chamber are given as $L = 6\,\mathrm{m}$ and $D = 2.6\,\mathrm{m}$.

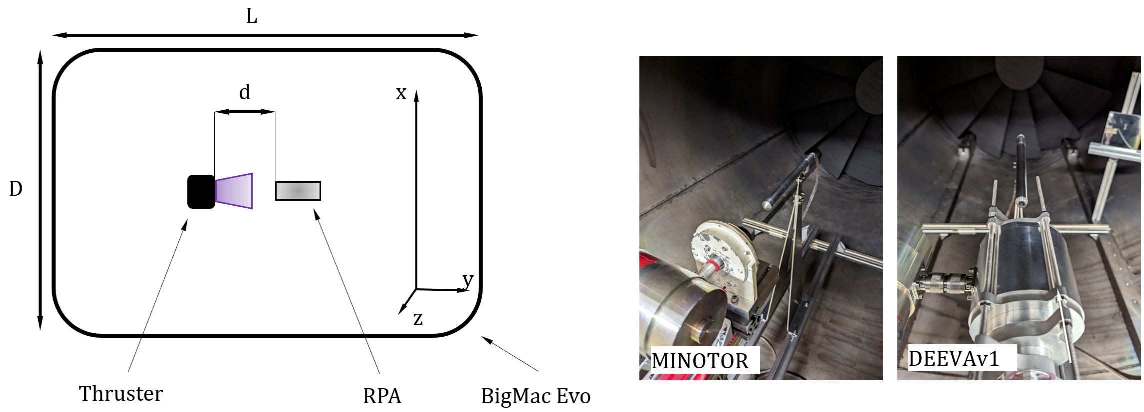

Figure 12: Test set up in BigMac Evo. A schematic of the set up in the vacuum chamber can be seen on the left. Photographs of the MINOTOR prototype with the circular waveguides and the DEEVAv1 prototype can be seen on the right. The retarding potential analyzer (RPA) with collimator can be seen in the photograph, as well as in the schematic drawing on the left. The distance d between the RPA and the thruster exit plane in this case is 30 cm. The dimensions of the vacuum chamber are given as $L = 3.2\,\mathrm{m}$ and $D = 1.6\,\mathrm{m}$.

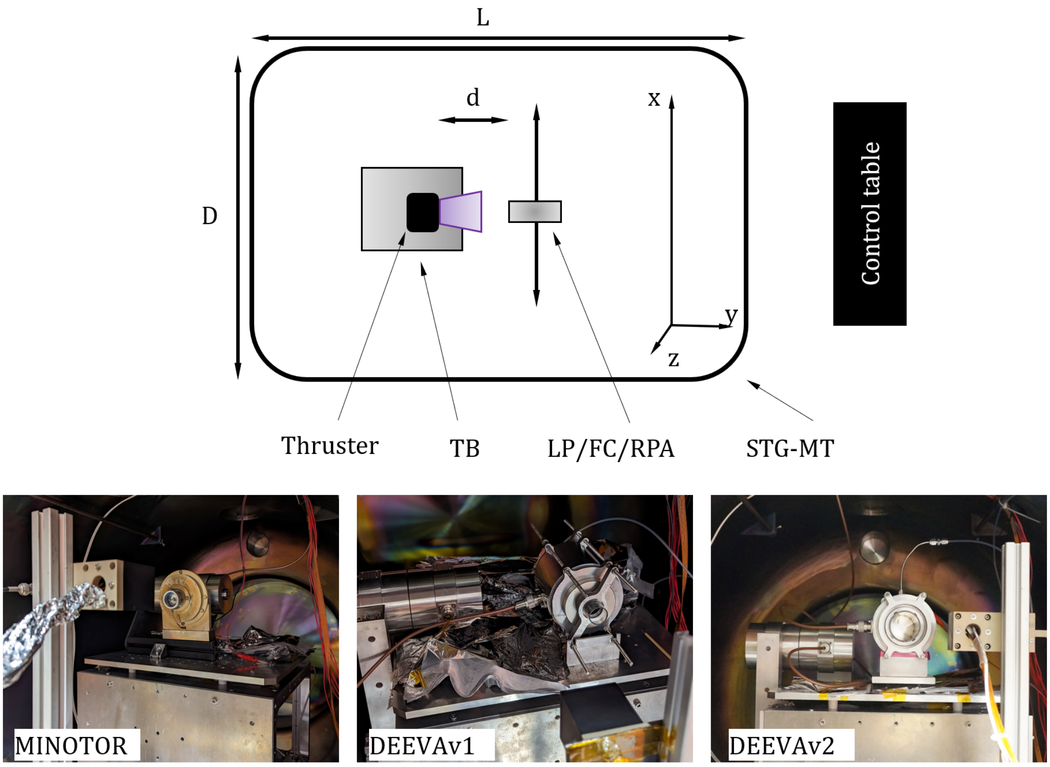

Figure 13: Test set up in STG-MT. A schematic drawing of the set up in the vacuum chamber can be seen on the top. Photographs of the set up with the MINOTOR prototype, the DEEVAv1 and DEEVAv2 prototype can be seen on the bottom. The diagnostics comprising retarding potential analyzer (RPA), Langmuir probe (LP), Faraday cup (FC), and thrust balance (TB) can be seen in the photograph, as well as in the schematic drawing. The distance d between the diagnostics and the thruster exit plane in this case is between 10 cm and 20 cm. The dimensions of the vacuum chamber are given as $L = 1.1$ m and $D = 1$ m.

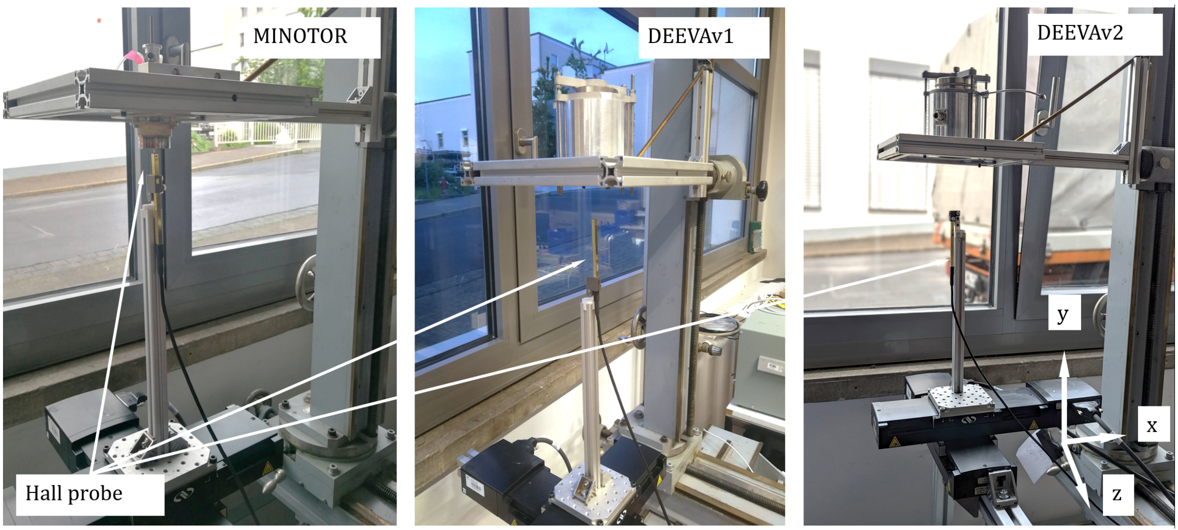

Figure 14: Set up of the magnetic field measurements of the thrusters. The Hall probe, the MINOTOR prototype (left), the DEEVAv1 thruster (center), as well as the DEEVAv2 thruster (right) are indicated in the photographs. Additionally, the cartesian coordinate system used is depicted.

2.3. Diagnostics for Thruster Characterization

2.3.1. Hall Probe

The magnetic field plays a decisive role in the functioning of the thruster, more precisely in the production and acceleration of the quasi-neutral plasma. For this reason, the magnetic field distribution of the thruster is measured in three spatial directions using a 3D Hall probe from the company Projekt Elektronik GmbH. If a current I is applied to a thin strip of metal (Hall sensor) and a magnetic field is applied perpendicular to the direction of the current, the charge carriers are deflected by the Lorentz force F_{L}. The produced difference in voltage (the Hall voltage U_{H}) between the two sides of the strip is proportional to the strength of the magnetic field. For the 3D probe, three of those strips/Hall sensors are used to detect the three spatial components of the magnetic field $\vec{B} = (B_x, B_y, B_z)$, see in Figure 15 on the right. The range of the probe in use is $\pm 200\,\mathrm{mT}$ and the linearity error is given as $\pm 0.1\,\mathrm{mT}$. Additionally to the downstream region, the ECR zone inside the thruster is also mapped. It is possible to move the probe in x, y, z direction with linear stages, see Figure 14. A schematic image of the Hall probe can be seen in Figure 15.

2.3.2. Langmuir Probe

One of the most technically simple, yet difficult to interpret, diagnostics tools is the Langmuir probe (LP) [3]. This probe consists of one, two or three conductive pins, directly brought into the plasma. If a single pin is introduced into the plasma and the voltage U between its tip and a reference potential is varied, the current voltage characteristic can be recorded. It can be divided into three ranges according to Demidov *et al.* [67]: For sufficiently negative probe voltage the probe collects mainly positive ions, called the ion saturation current $I_{\mathrm{i,sat}}$. In the transition part of the characteristic the probe collects ions and electrons [67]. If no current is measured the ion and electron currents are equal, this is the floating potential Φ_{fl} [67]. For the set voltage equal to the plasma potential Φ_{P}, the characteristic may show a kink ('knee') because the potential changes character from attracting ions and repelling electrons to repelling ions and attracting electrons [67]. For higher positive voltages, the probe only collects electrons, yielding the electron saturation current $I_{\mathrm{e,sat}}$ [67]. A schematic of a single Langmuir probe characteristic can be seen in Figure 16.

By measuring this current-voltage characteristic it is possible to capture properties of the plasma, such as carrier temperatures, potentials, carrier densities etc [3]. The analysis of the data requires an appropriate theory. We apply the Druyvestein method for analysing the single Langmuir probe measurements [68, 69]. Using this method we determine directly the electron energy distribution function EEDF $f(E)$ as the second derivative of the measured current voltage characteristic $\mathrm{d}^2 I_e/\mathrm{d}U^2$ with the probe surface A_{P}, the electron mass m_{e} and charge e, and the energy E of the electron hitting the probe:

$$f(E) = \frac{2}{e^2 A_{\mathrm{P}}} \sqrt{(2 m_{\mathrm{e}} E)} \frac{\mathrm{d}^2 I_e}{\mathrm{d}E^2}. \tag{2.40}$$

We correct the measured current I_0 by subtracting the ion current I_{i} prior to calculate the second derivative of the electron current $I_{\mathrm{e}} = I_0 - I_{\mathrm{i}}$. By calculating the moments of the distribution function we derive the electron density n_{e} and temperature T_{e} of the plasma:

$$n_{\mathrm{e}} = \int_0^\infty f(E)\mathrm{d}E, \tag{2.41}$$

$$T_{\mathrm{e}} = \frac{2}{3n_{\mathrm{e}}} \int_0^\infty f(E) E \mathrm{d}E. \tag{2.42}$$

An exemplary evaluation procedure and determination of the EEDF $f(E)$ can be seen in Figure 17. We point out that this model assumes an isotropy of the plasma which is most likely not given in the operating thruster. According to Lobbia *et al.* such an anisotropic effect on the electron current collection is mitigated when the anisotropic drifting beam component is parallel to the electrode

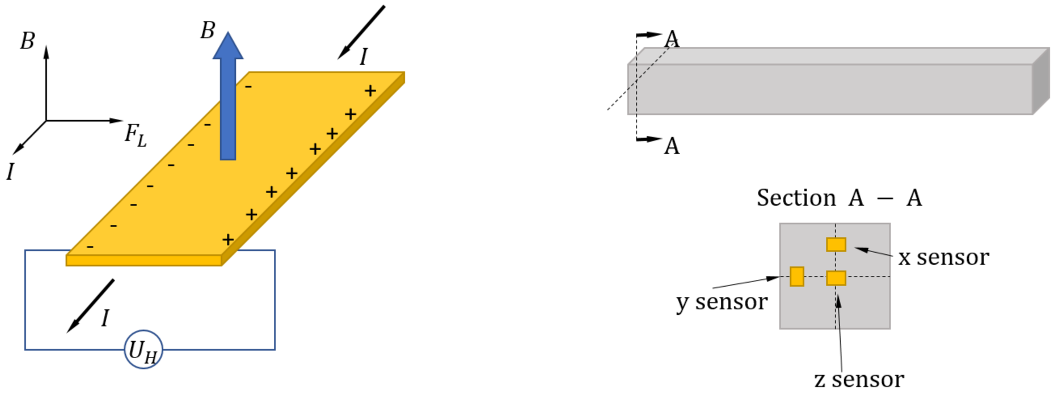

Figure 15: Schematic image of a Hall probe. A current I is applied to the metal strip, indicated in yellow. If a magnetic field is applied orthogonally to the current direction a Lorentz force F_{L} deflects the charge carriers and a Hall voltage U_{H} can be measured, which is proportional to the applied magnetic field. If three of those strips are combined, a 3D magnetic field topology can be measured. Such a 3D Hall probe can be seen schematically on the right.

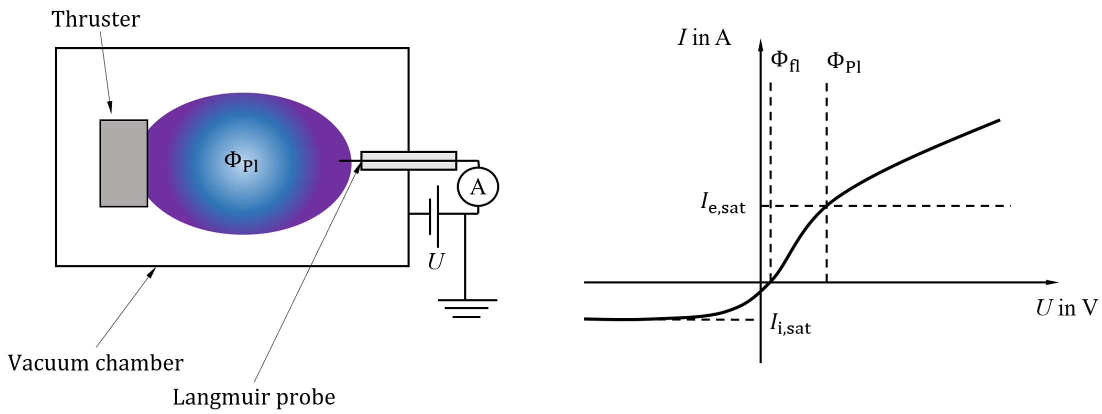

Figure 16: On the left, schematic of the measurement procedure with a Langmuir single probe. The electrode tip is exposed to the plasma exiting the thruster. By applying a voltage U between plasma and reference potential (in this case ground) the current can be measured. On the right, resulting Langmuir current voltage characteristic, showing the saturation currents $I_{\mathrm{i,sat}}, I_{\mathrm{e,sat}}$ as well as the plasma potential Φ_{Pl} and the floating potential Φ_{fl}. The non-saturation behavior after the knee towards higher voltages U is indicated.

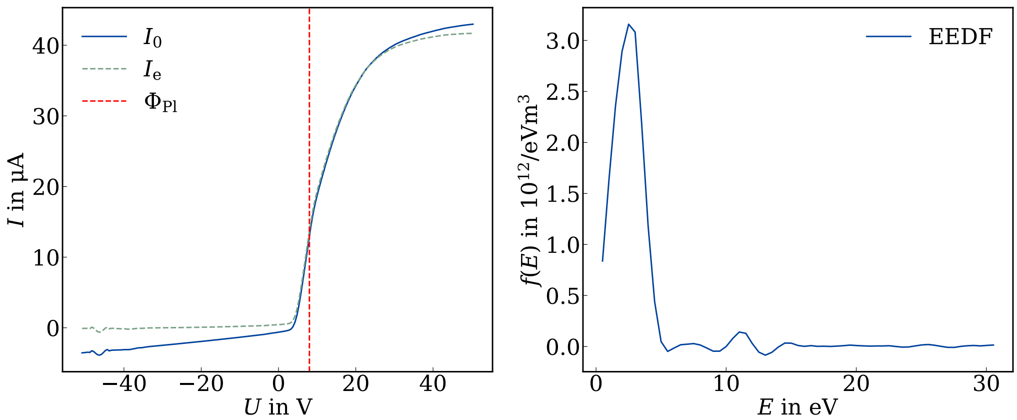

Figure 17: Exemplary evaluation of Langmuir probe data of the first DEEVAv1 prototype. On the left in blue, the raw data of the DEEVAv1 at 30 W, 2.45 GHz and 1 sccm xenon. The green, dashed curve represents the electron current I_e, after subtraction of the ion current I_i. The plasma potential, in this example, is $\Phi_{Pl} \approx 8$ V and is depicted in red. On the right, the resulting EEDF, exhibiting a Maxwellian shape with a maximum at an energy of about 3.5 eV.

surface [68]. Furthermore it is stated in Lobbia *et al.* that the impact of magnetic fields on the movement can be neglected in the limit where the probe radius is much smaller than the local Larmor radius, which is for our plasma most likely the case. Previous studies regarding these contradictory recommendations (measuring parallel or orthogonal to the magnetic field lines) lead to the decision to measure in parallel orientation [57]. Excerpts of this study are shown during the course of this work. These tests are carried out much closer to the thruster, at a distance of about 6 cm. Preliminary measurements regarding the relevance of the distance of the probe to the thruster allowed us to conclude that no anisotropy effects are observed at a distance of 10 to 22 cm [70]. This means that at a greater distance, the orientation of the probe in relation to the magnetic field lines plays a minor role. In addition, the non-Maxwellian character of the plasma could not be confirmed at that distance. This was explained due to the smaller magnetic flux density at greater distance to the thruster [70].

We present results for the distances $y = 6 \pm 0.5$ cm to $y = 10 \pm 0.5$ cm. We determine the surface of the single probe to be $A_P = 3.15 \pm 0.1 \cdot 10^{-5}\,\mathrm{m}^2$. We scan with a SMU unit (Source and Measurement unit) of the company Keysight B2901A over a voltage range of -100 V to $+200$ V and measure the corresponding current of the probe. We choose the vacuum chamber potential/ground as the reference potential. The resolution of the SMU unit for the measurement range $0 \leq |I| \leq 106$ mA is given as 100 nA. Furthermore, a low pass filter on the airside of the chamber is used. The low pass filter in use is a LC-circuit with a capacitance C of 100 nF and an inductivity L of 27 nH.

2.3.3. Retarding Potential Analyzer

A challenge arises when trying to extract information about the ion distribution function from a Langmuir probe, which operates at a positive potential, repelling ions and drawing electron-saturation current [71]. This electron-saturation current is typically significant enough to overshadow any variations in the ion current that could provide insights into the ion temperature or energy distribution [71]. Here, more sophisticated analyzers, such as the "gridded energy analyzer," come into use. Retarding potential analyzers (RPAs) are often employed to obtain information about the ion energy distribution functions of plasmas. These devices employ a system of grids at different potentials [71]. A schematic image showing the operating principle of the RPAs in use, both of them four-gridded RPAs, can be seen in Figure 18. The concept is as follows: the first grid is kept electrically floating, allowing the measurement of a floating grid potential. In post-processing, this enables gaining information about the actual energies measured. The second grid repels essentially all the electrons in the plasma plume,

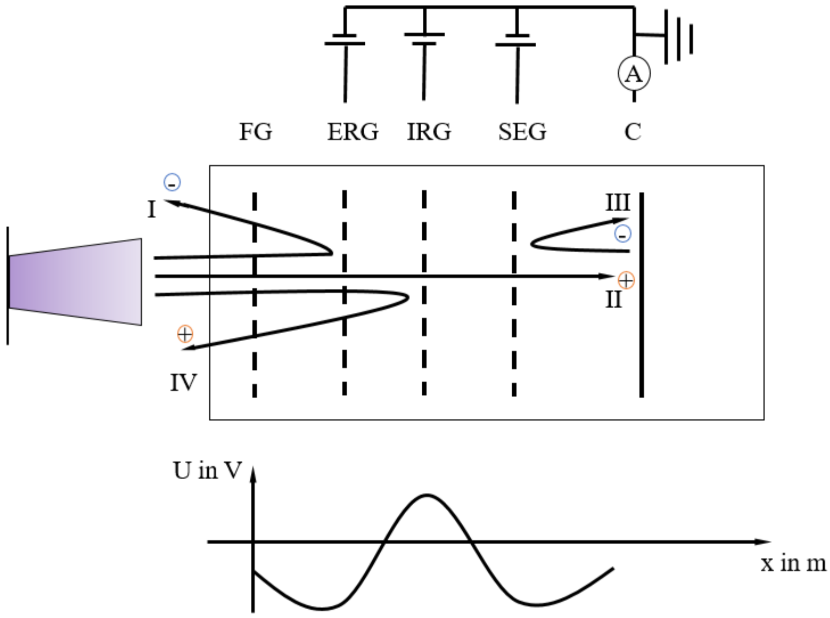

Figure 18: Schematic of a four-gridded RPA. The plasma beam is depicted in violet on the left. The first grid is the floating grid (FG), it is followed by the electron retarding grid (ERG). The third grid is the ion retarding grid (IRG), and the fourth, the secondary electron suppressing grid (SEG). The collector (C) is positioned behind the grid sequence. On top, the electrical wiring is shown, resulting in the exemplary potential curve at the bottom. Possible particle motions are also depicted: Case I marks electrons in the beam deflected by the ERG. Case II marks ions going through all the grids and hitting the collector. Case III shows produced secondary electrons being deflected back to the collector by the SEG. Case IV shows ions being repelled at the IRG because their energy is lower than the potential barrier.

allowing only ions to pass. The third grid is the ion retarding grid, where a positive potential U is sequentially set, allowing only ions exceeding the energy eU to pass and reach the collector [71, 72]. The fourth grid, the secondary electron grid, suppresses electrons that may be produced by the ions hitting the collector [71, 72]. It is possible to gain information about ion temperature and ion density with RPA measurements. However, since we cannot estimate the effect of additional charge densities existing between the grids in this set up (which can change the potential and therefore influence current measurements), we focus on determining the maximum ion energy and IEDF [71]. The latter is determined by the first derivative of the measured current. An exemplary evaluation is shown in Figure 19. The RPA used at JLU is an in-house-built device equipped with a 30 cm long collimator. The RPA used at DLR is a commercial RPA from the company Plasma Controls, LLC. For RPA operation, pico-amperemeters from Keithley with a resolution of 1 nA in the 2 mA range are employed.

2.3.4. Faraday Cup

Faraday cups (FCs) are detectors for measuring ion or electron currents. They are often used in electric propulsion to measure electron or ion beam current densities. The basic operating principle of a FC is as follows: A collector consisting of a conductive material is inserted into the plasma and shielded by a plate with a hole/grid. Ions hitting the surface of the collector cause a measurable current. The FC in use is the Kimball Physics model FC-71A. The FC consists of a hollow stainless steel cylinder closed at the base, with an aperture for collecting electrons or ions. The outer cylinder can be grounded or biased and provides shielding from the opposite charge. The current is then conducted via a vacuum

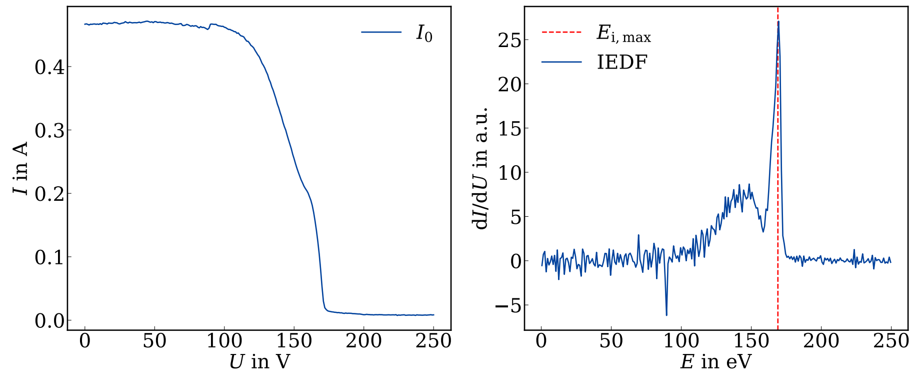

Figure 19: Exemplary RPA evaluation. On the left, raw ion current coming from the MINOTOR thruster, operated with 1 sccm xenon, at 20 W input power, and a frequency of 2450 MHz. With an increase of ion repeller voltage U, fewer ions reach the collector. On the right, the first derivative dI/dU as a function of ion energy E - the ion energy distribution function (IEDF), yielding a bi-Maxwellian shape with an ion energy of maximum probability of $E_{\mathrm{i,max}} \approx 168\,\mathrm{eV}$.

feed-through to a pico-amperemeter from the company Keithley with a resolution of 1 nA in the 2 mA range. The hole diameter for the grid is $r_{\mathrm{P}}= 3\,\mathrm{mm}$. The repeller grid is set to $-40\,\mathrm{V}$ to repel the beam electrons. The beam is then spatially scanned from $x = \pm 75\,\mathrm{cm}$ in a distance $y = 10 \pm 0.5\,\mathrm{cm}$ in 2.5 mm/s. A low pass filter is used with a capacitance of $C = 100\,\mathrm{nF}$ and an inductivity of $L = 27\,\mathrm{nH}$. Main information gained from FC measurements is about the beam shape and beam radius r_{B}. This is done by the following procedure: First, we determine the current density J_{beam} (in A/mm^2) by dividing the measured current by the grid area:

$$J_{\mathrm{beam}} = \frac{I_0}{A_{\mathrm{grid}}} = \frac{I_0}{\pi r_{\mathrm{P}}^2}. \tag{2.43}$$

In the analysis we neglect several factors: Firstly the transparency of the grid. Due to the possible build up of a plasma sheath on the grid, the detected ion current density may be influenced. Furthermore, secondary electrons may be produced, if charged particles hit the collector surface. For both aspects additional factors come into play for the current density determination, compare the work of Brown *et al.* [73].

The line current density profile represents the current density along a one-dimensional axis, denoted as the x-axis. It provides information about how the current density varies along this axis, see Figure 20. For the analysis we sort the current density values in descending order, along with their corresponding x-values. This is done to ensure that the cumulative sum Σ_{I} will be monotonically increasing. The integration under the cumulative sum allows us to determine the beam radius r_{beam}, where 95 % of the total beam current are reached.

It is now possible to determine the beam divergence angle α:

$$\alpha = \arctan\left(\frac{r_{\mathrm{beam}} - r_{\mathrm{thruster}}}{y}\right), \tag{2.44}$$

with the determined beam radius r_{B}, the radius of the thruster exit and the distance $y = 100\,\mathrm{mm}$ to the thruster [74]. For example, the thrusters radii are for MINOTOR $r_{\mathrm{thruster}} = 13.5\,\mathrm{mm}$, for the DEEVAv1 prototype $r_{\mathrm{thruster}} = 12.5\,\mathrm{mm}$ and for DEEVAv2 $r_{\mathrm{thruster}} = 22.5\,\mathrm{mm}$. To convert the line current density profile to a estimated plane current density in the (x, z) plane, we assume rotational symmetry about the y axis. We can extend the line current density to a two-dimensional plane by assuming that the current density is the same for all points at the same distance from the origin. The estimated absolute current I_{beam} is then the total current passing through the entire plane. Since we

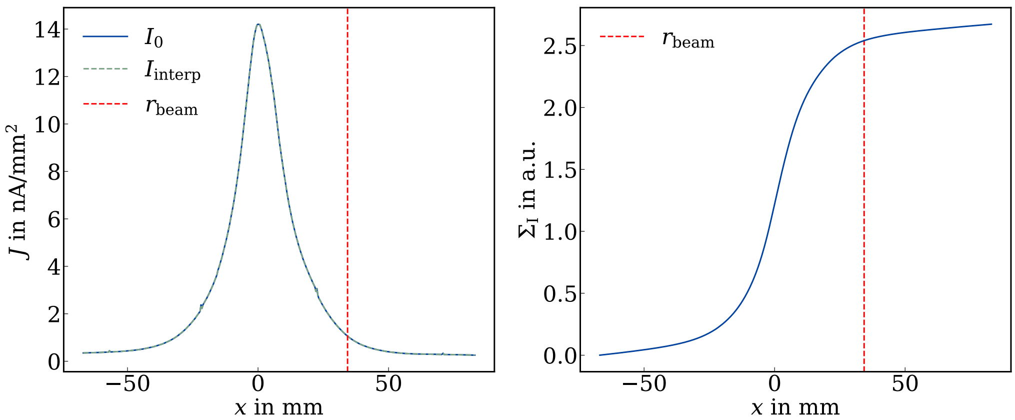

Figure 20: Exemplary determination of beam radius. The raw data beam scan can be seen in the left graph in blue. For the cumulative sum an interpolation is necessary and depicted as green dashed line. On the right plot the cumulative sum Σ_I is depicted in blue, as well as the position where the set fraction of the beam, to be 95%, is reached. In this example the beam radius, where 95% of the current is included, is at $r_\mathrm{beam} \approx 34\,\mathrm{mm}$. The DEEVAv1 thruster settings in this example are 30 W input power, 1 sccm volume flow xenon and a MW frequency of 2.45 GHz.

assume rotational symmetry, we can perform the integration only in the radial direction x from 0 to infinity and in the azimuthal direction from 0 to 2π [73]. The integration will give us the total current passing through the plane:

$$I_\mathrm{beam} = 2\pi \int_0^\infty J(x)x\mathrm{d}x. \tag{2.45}$$

An example of a plane current density profile is given in Figure 21. It is imperative to acknowledge that in the earlier examinations of the MINOTOR thruster, solely Faraday probes (FP), not Faraday cups, were employed for the assessment of ion current densities and beam currents, ranging from $I_\mathrm{beam} = 10$ to $80\,\mathrm{mA}$ [29, 31, 32, 33, 34, 35, 54, 55]. Furthermore, it is also important to note that repeller voltages of $-200\,\mathrm{V}$ to $-300\,\mathrm{V}$ were necessary in those studies, even though usually repeller voltages of -15 to $-35\,\mathrm{V}$ are required for EP plasmas, as it is stated in Ref. 73. Before commencing our measurements, various repeller voltage settings were tested. These experiments revealed that higher repeller voltages lead to an increased occurrence of arcing between the FC and the probe holding system. Consequently, the decision to settle on a repeller voltage of $-40\,\mathrm{V}$ was made. Additionally, the assumed rotational symmetry is not present in case of DEEVAv2. Therefore, the determination of total beam currents should be interpreted as estimations.

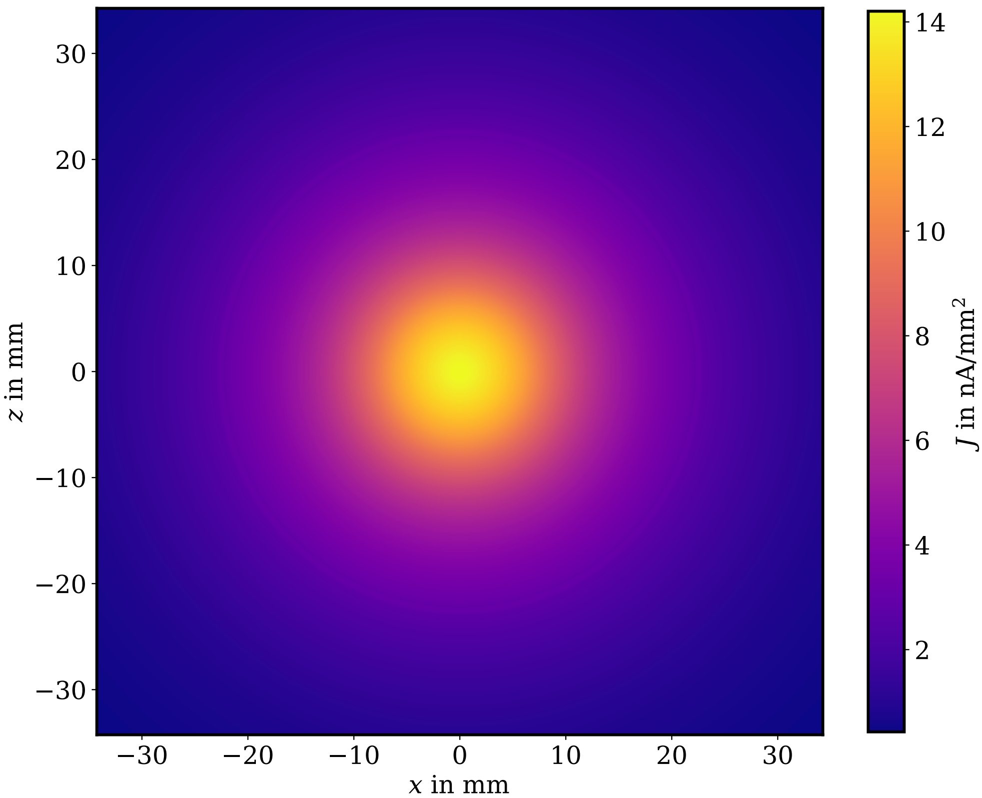

Figure 21: Exemplary determination of total beam current assuming rotational symmetry of the beam. A maximum beam current density of 14 nA/mm^2 is reached in the center of the plane. The DEEVAv1 thruster settings in this case are 30 W input power, 1 sccm volume flow xenon and an excitation frequency of 2.45 GHz.

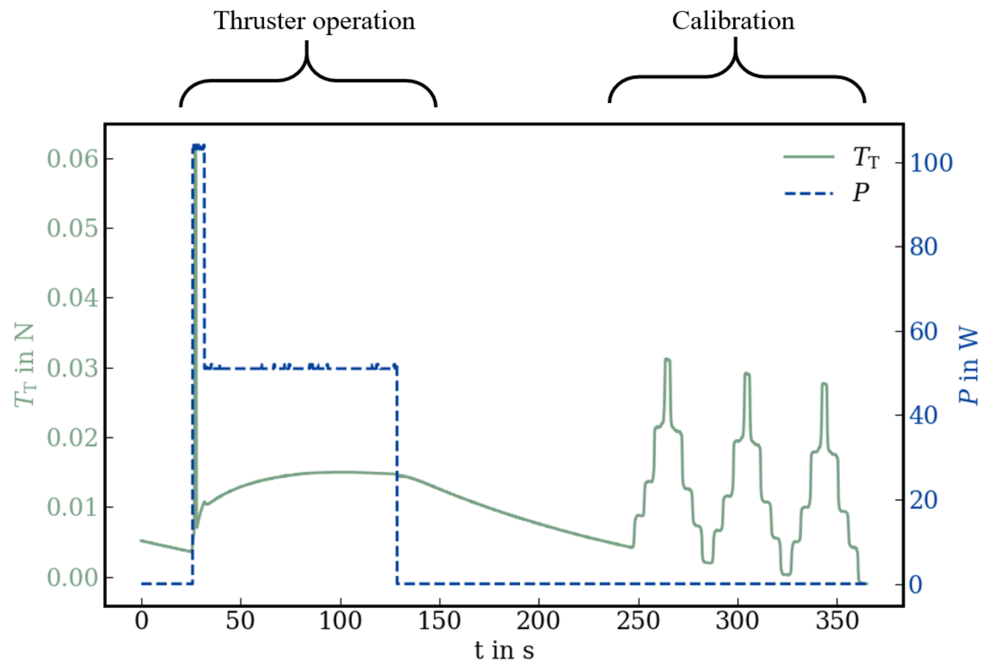

Figure 22: Demonstration of a thrust measurement cycle. The thrust is shown in green, the power set in blue. The DEEVAv2 prototype is turned on with 100 W and then regulated down to 50 W at 1 sccm volume flow xenon and frequency of 2.45 GHz. The ignition is started by a gas shock, which can also be seen in the thrust measurement ($t = 25$ s). The thruster is then kept running for about two minutes. During this time a drift can be observed, most likely due to heating up. If the thruster is then turned off, after approximately two minutes, the drift behavior changes. After another two minutes, a calibration is performed and can be seen on the right in the figure. The calibration is performed three times prior to the next measurement.

2.3.5. Thrust Balance

The thrust balance DEPB (DLR Electric Propulsion Thrust Balance) used in this investigation is described in Refs. 75 and 76. It is an inverted double pendulum, consisting of two pendulums connected by a plate with a given stiffness and elasticity. The TB consists of an aluminium table, casing and eight quartz-glass rods used as flexible bearings for the thruster table. To dampen possible high frequency oscillations an eddy current brake is built in. A micrometer-screw is used to establish the connection between the moving thrust balance table and the Sartorius® WZA224 load cell [76]. For the calibration of the thrust balance, four fine weights are sequential applied as load to the load cell and, by taking the rope and the angle of the rope on the pulley into account, the gravitational force is equal to the thrust shown at the scale [77]. Using this procedure, a calibration is possible. Temperature gradients have a major impact on the thrust measurement. The temperature drift typically causes a linear background in the thrust measurement as a function of time which can be removed by a fitting procedure. Another influencing factor is the possibility to excite eigenfrequencies of the thrust balance by turbopumps or other moving parts. This can lead to overlaying frequency structures. An accuracy of 0.2 mN and a repeatability of 0.1 mN for the DEPB are given [77]. Many measurements are performed to take the mean of the measured thrust values.

The evaluation procedure of the measured data is shown exemplary in the following. In Figure 22 one can see results of a typical testing procedure. In this example the DEEVAv1 prototype is turned on at 120 W, 2.45 GHz, 1 sccm xenon. Then, the power is varied to the wished setting (to 50 W) by keeping the volume flow and frequency fixed. The thruster is turned off and the delta in thrust is measured. After that, the calibration of the system is performed. The thermal drift is prominent and has to be taken into account. For that, a linear fit is applied, before the thruster is turned off, compare

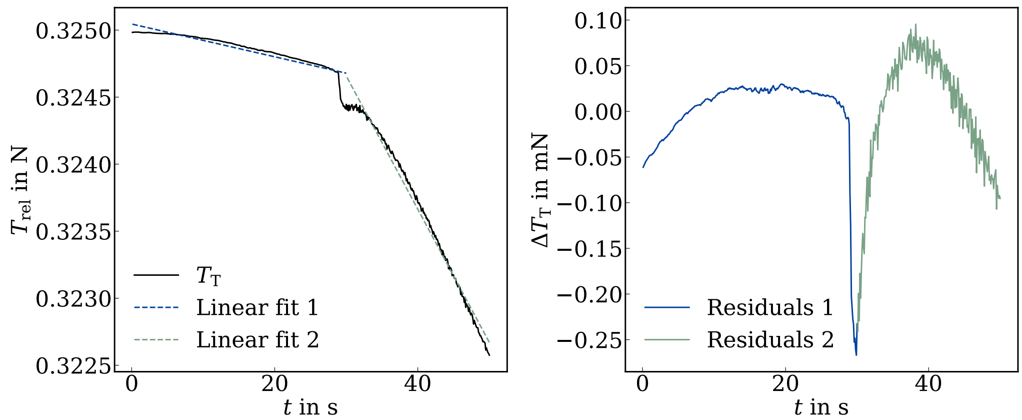

Figure 23: Demonstration of the evaluation procedure of the TB data to take the thermal drift into account. On the left, raw data T_{rel} in blue, showing the drift of the thrust balance. The two linear curve fits applied before and after the thruster turn off are depicted in blue and green. Shown in the plot on the right are the residuals after subtracting the linear curve fits from the raw data. In this example, the DEEVAv2 thruster settings at 50 W, 2.45 GHz, 1 sccm xenon lead to a measured thrust of $T_{\mathrm{T}} \approx 0.25$ mN.

Figure 23 (top). This accounts for the linear part of the thermal drift, caused by heated up cables etc. By that it is possible to subtract the drift and obtain the residual thrust, see Figure 23 (bottom). The same procedure is applied for the calibration, see Figure 24. The mean of the measured plateau values for one cycle is taken, and the measured thrust is plotted against the gravitational force of the fine weights. A linear curve fit yields the calibration factor.

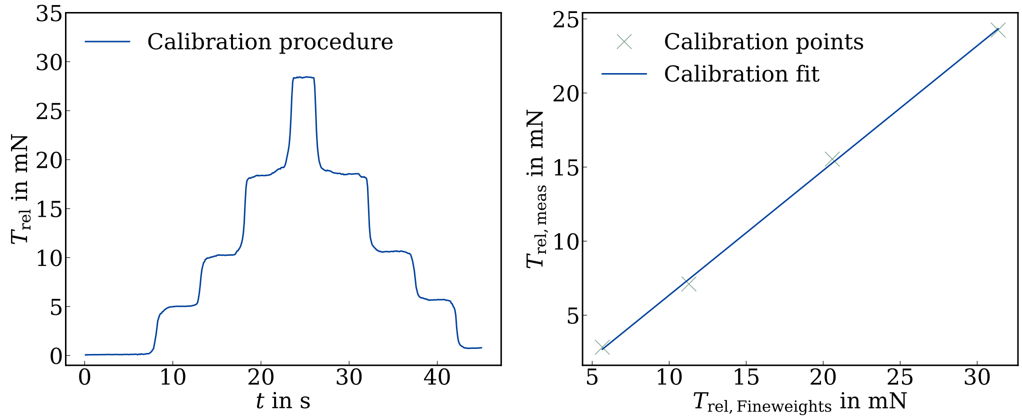

Figure 24: Demonstration of the evaluation procedure for the calibration. On the left, raw data of the four fine weights applied and removed sequentially on the weighing cell. Furthermore the different thrust values of beginning and ending of the calibration procedure show a thermal drift of the thrust balance. On the right plot, the x axis showing the gravitational force of the fine weights as "thrust" $T_{\mathrm{T,Fineweights}}$, on the y axis the measured force/thrust $T_{\mathrm{T,meas}}$. In this example the linear fit (in green dashed) yields the calibration factor of about 1.1.

The procedure involving linear fits must be handled with care for each data set. Given its heightened sensitivity, the thrust balance data requires particularly cautious evaluation and interpretation. However, the thrust efficiency can then be determined, with the measured thrust, the mass flow and the input power as shown in Equation 2.4 [54, 56].

It should be mentioned that it is possible to determine the effective thrust with the knowledge of the ion kinetic energy, i.e. their velocity and the ion current [30]. It is stated in Ref. 55, that thrust determined with electrostatic probes systematically underestimates the thrust of the MINOTOR prototype by about 20% in comparison with the thrust balance results. The force/thrust determined with electrostatic probes F_{P} can be estimated from the corresponding ion current I_{beam} (determined from ion current density measurements, see above) and from the maximum ion velocity v_{i} (determined from the IEDF, see above). The thrust estimated with electrostatic probes F_{P}, neglecting double charged ions, can therefore be formulated with the ion mass m_{i}, the elementary charge e, the total ion beam current I_{beam} and the ion velocity v_{i} as

$$F_{\mathrm{P}} = \frac{m_{\mathrm{i}}}{e} I_{\mathrm{beam}} v_{\mathrm{i}}. \tag{2.46}$$

The ion velocity is determined from the maximum ion energy $E_{\mathrm{i,max}}$ with

$$v_{\mathrm{i}} = \sqrt{\frac{2E_{\mathrm{i,max}}}{m_{\mathrm{i}}}}. \tag{2.47}$$

In previous studies of the 30W-MINOTOR ECRT, thrusts in the range of $T_{\mathrm{T}} = 0.15$ to $2\,\mathrm{mN}$ and a thrust efficiency for the highest thrust ($T_{\mathrm{T}} = 2\,\mathrm{mN}$ at 1 sccm xenon and 50 W) of 35% were determined [31, 32, 35, 54, 55, 65].

3. Characterization of the Thrusters

The outline of this chapter is as follows: First, we present the thruster and propellant combinations investigated in this work, along with motivations and limitations for the selection of the thruster prototype and propellant. Next, we address the research task, focusing on how different microwave coupling methods, along with the associated magnetic field topologies, influence plasma parameters and ultimately affect thrust. Specifically, we explore the measured differences in thrust and plasma parameters and aim to explain these variations using the diagnostic methods available.

In order to do this, we first show typical thrust results obtained for the different prototypes. Additional data is presented in the Appendix. From the thrust results, we come to the question: Why does the MINOTOR thruster exhibit the highest measured thrust? As discussed in Chapter 2, thrust contributions can be attributed to ion current and neutral gas exiting the thruster. For ion-related thrust, the beam ion current, ion velocity, and ion mass contribute to the total thrust (see Eq. 2.46). This contribution can be estimated using probe measurements (such as FC and RPA), as described in Chapter 2. After subtracting the probe-estimated force from the thrust balance measurements, the remaining force can be attributed to neutral gas contribution (either hot or cold gas). The ratio between the force determined via probes and the thrust measured by the thrust balance serves as a metric for evaluating how effectively the magnetic nozzle contributes to thrust production. To address why the MINOTOR thruster produces the highest thrust, we investigate how the thrust production relates to the magnetic nozzle shape. For this purpose, we compare the magnetic field topologies of the prototypes under investigation, focusing on aspects such as magnetic field gradients and the converging/diverging nature of the field lines, as these characteristics can either enhance or reduce thrust production. We also verify whether the ECR condition is met for the chosen microwave frequency. Next, we explore electron temperature, which is assumed to be the driving force behind ion acceleration in the magnetic nozzle (see Chapter 2). We examine whether a correlation exists between electron temperature and ion energy and compare the absolute values of these parameters between the prototypes. Furthermore, we investigate the respective ion and electron energy distribution functions and provide comparison measurements in different vacuum chambers and with different diagnostic tools, to reaffirm the presented results. We then estimate the total ion current exiting the thruster, acknowledging that the assumption of rotational symmetry (as mentioned in Chapter 2) is a key limitation of this study. However, this assumption aligns well with prior FC array measurements, from which we will also present selected excerpts. Using the determined ion energies and beam currents for the prototypes, we can compare the force estimated from probe measurements with the thrust balance results. The ratio of these two force values represents the percentage of thrust attributable to the magnetic nozzle, which can then be compared across all prototypes and propellant combinations. This analysis provides insight into which configurations are better suited for efficient magnetic nozzle operation.

It is important to note that, in the operating principle of a magnetic nozzle, the separation between plasma generation and acceleration is not as distinct as in other thruster types that use alternative acceleration methods. The efficiency of a magnetic nozzle depends on the interplay between the plasma and the magnetic field topology. Both, plasma properties (such as plasma potential and electron temperature) and the magnetic field configuration, play a crucial role in determining the overall performance. Therefore, when we present magnetic field topologies or discuss potential design improvements for the prototypes, further testing and simulation are required to assess whether the combination of plasma and magnetic field topology meets the expectations.

3.1. Configurations and Propellants under Investigation

An overview of the prototypes and their respective propellants is provided in Table 2. The term "DEEVAv2-att" refers to the DEEVAv2 configuration where both the disc magnets and ferrite magnets are polarized in the same direction. In contrast, "DEEVAv2-rep" indicates counter-directional magnetization of the magnets. The terms "float" and "grounded" describe the electrical connection between the thruster body and ground, indicating whether the thruster can charge up (i.e., achieve a non-zero thruster potential, $\Phi_{\mathrm{TW}} \neq 0$) or not ($\Phi_{\mathrm{TW}} = 0$).

Thruster set up		Propellant			Chamber and Diagnostics		
Prototype	Setup	Xenon	Argon	Krypton	JUMBO	BigMac	STG-MT
MINOTOR	floating, grounded	x			LP, FC, RPA	FC, PPA, RPA	LP, FC, RPA, TB
DEEVAv1	floating, grounded	x				RPA	RPA, LP, FC, TB
DEEVAv2-att	floating, grounded	x	x	x			LP, FC, RPA, TB
DEEVAv2-rep	grounded	x	x	x			LP, FC, RPA, TB

Table 2: Thruster configurations, propellants and employed diagnostics. DEEVAv2-att stands for the DEEVAv2 configuration where the disc magnets' and the ferrite magnets' magnetization are pointing in the same direction, while the DEEVAv2-rep stands for the counter directional magnetization of the magnets. Float and grounded refers to the electrical connection between ground and thruster body - i.e. if the thruster can charge up to a thruster potential $\Phi_{\mathrm{TW}} \neq 0$ or not $\Phi_{\mathrm{TW}} = 0$. The facilities and the diagnostic employed there are also shown. LP stands for Langmuir probe, PPA for parallel plate analyzer, RPA for retarding potential analyzer, FC for Faraday cup, and TB for thrust balance.

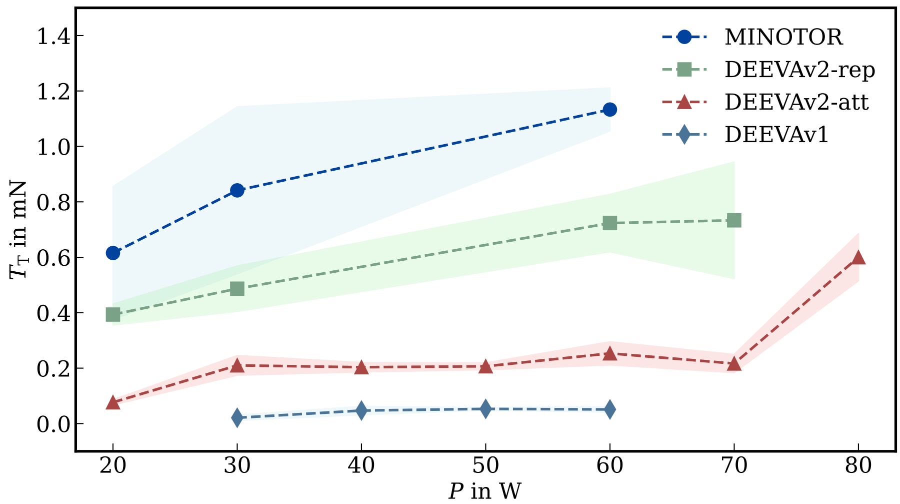

Figure 25: Thrust results for input power variation of the thruster prototypes; MINOTOR in blue, the DEEVAv2-repulsive in green, the DEEVAv2-attractive configuration in red and the DEEVAv1 prototype in light blue. All thruster prototypes were operated with xenon as propellant, at 2450 MHz and 1 sccm. The standard deviation from multiple measurements taken, is depicted as underlying shadows of the measurement points.

In the course of this work, we present results for measurements conducted with argon and xenon as propellants. Additional results for krypton are provided in the Appendix. Details on the facilities and diagnostics used for the measurements are also shown.

In total, six configurations — the prototypes operating with xenon and argon — are measured and compared in this study. Although krypton and air can also be used as propellants with the DEEVAv2 prototypes, these configurations are not included in this analysis. Additionally, initial tests were conducted using the MINOTOR and DEEVAv1 prototypes with argon. These tests demonstrated that a flow rate of 1 sccm was not feasible for these prototypes, as stable operation — required for continuous and repeatable measurements — could not be achieved. Consequently, the results presented here for argon pertain solely to the DEEVAv2 configurations, both in attractive and repulsive arrangement of the magnet magnetizations.

3.2. Thrust Balance Measurements Results

As shown in Figure 25, all prototypes exhibit an increasing trend in thrust with rising input power. The MINOTOR prototype reaches a maximum thrust of approximately 1 mN, followed by the DEEVAv2-repulsive (DEEVAv2-rep) configuration with a maximum thrust of about 0.7 mN and the DEEVAv2-attractive (DEEVAv2-att) configuration of about 0.6 mN. The smallest thrust, at a maximum of 0.05 mN, is measured for the DEEVAv1 thruster. All these measurements are conducted using xenon as propellant. Additional thrust balance results for argon, along with excerpts covering operational variations are provided later in this chapter. In the Appendix, the influence of input frequency and volume flow variation on thrust is discussed.

For the DEEVAv1 thruster, the magnitude of thrust produced approaches that of neutral gas injection. This assumption — that the measured force is primarily due to neutral gas (cold gas) — is confirmed by the results shown in Figure 26. In this figure, the thrust balance signal T_T responds to changes in the volume flow rate $\dot{V}$, with xenon as the propellant. The volume flow is set to 5 sccm for approximately 4 seconds on two occasions, within the time frame 0 to 12 s. Two intervals at a

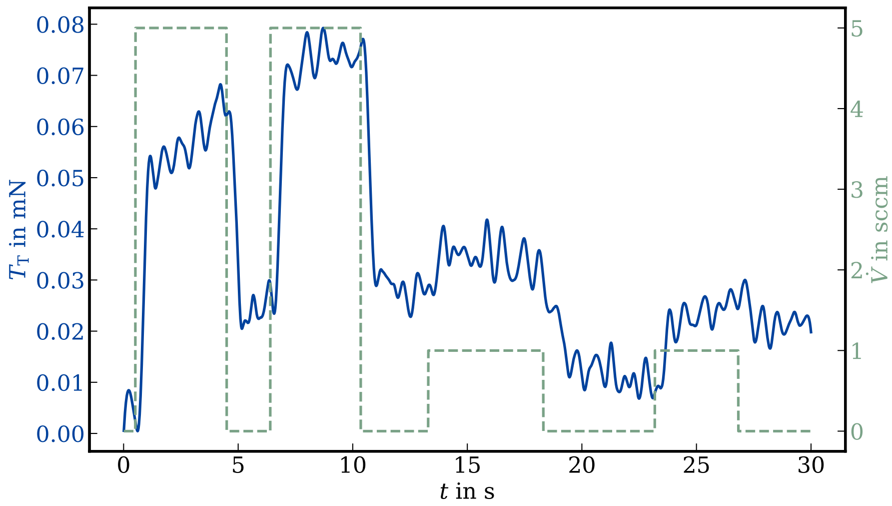

Figure 26: Cold gas test with the DEEVAv1 prototype. The signal of the thrust balance T_T is depicted in blue on the left axis. The volume flow $\dot{V}$ is shown in green on the right axis. The propellant in use is xenon. The volume flow is set to 5 sccm for approximately 4 s and then set to zero. This is repeated one more time. Then, after 3 s break, the flow is set to 1 sccm for 4 s and again set to zero. This procedure is repeated one more time. A cold gas thrust of approximately 0.04 mN is determined for a set volume flow of 5 sccm. We detect a thrust of approximately 0.02 mN for a set volume flow of 1 sccm xenon.

setting of 1 sccm in the time frame 12 to 30 s follow. The underlying drift in the signal is attributable to thermal effects on the thrust balance, while the oscillations superimposed on the signal are likely due to vibrations originating from the chamber and the turbo molecular pump. A cold gas thrust of approximately 0.04 mN is observed for a set volume flow of 5 sccm. Whereas, at a volume flow of 1 sccm xenon, the measured thrust is approximately 0.02 mN. These values correspond closely to the thrusts produced by the DEEVAv1 prototype in operation at these propellant flow rates. Furthermore, observations indicate that no beam exits the thruster body, even when the plasma is ignited. This suggests that the plasma does not significantly contribute to the generated thrust (see also the discharge images in Figure 30).

Although plasma ignition can be realized for the DEEVAv1 prototype, the contribution of ion current to thrust appears negligible. This is further confirmed when comparing the thrust obtained during volume flow variation where all the plasma parameters (ion beam current, electron temperature and ion energy) decrease with increasing volume flow, but the thrust increased, as it can be seen in the Appendix. This differs from the expectation. If the thrust is plasma induced, and if with increasing volume flow a decrease in ion energy and current can be observed, the thrust should also decrease.

In contrast, the DEEVAv2-att configuration shows a clear increase in thrust with increasing power, with significantly higher thrust values compared to the DEEVAv1. Additionally, both the attractive and repulsive configurations of the DEEVAv2 show a visible plasma beam exiting the thruster, which is absent in the DEEVAv1 prototype (see Figure 30). While the DEEVAv2-att configuration already demonstrates improved performance, the DEEVAv2-rep configuration performs even better, approaching the thrust values of the MINOTOR prototype. For comparison across all prototypes, the input power is limited to 80 W in this plot.

Thrust results for the DEEVAv2 prototypes operating with xenon and argon at 1 sccm and a frequency of 2450 MHz, at higher input power levels, are presented in Figure 27. The figure shows that as input power increases, the DEEVAv2 prototypes (in both configurations) achieve thrusts of about

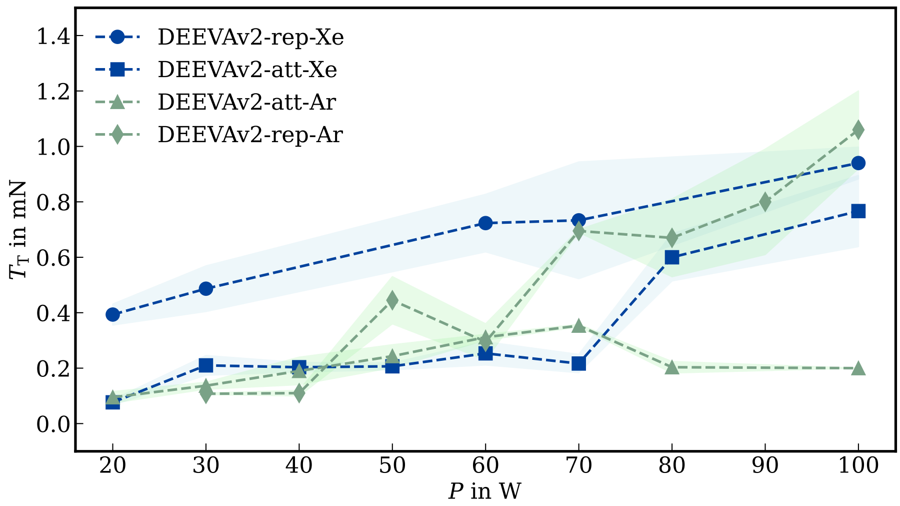

Figure 27: Thrust results T_T determined with the thrust balance, for input power variation of the DEEVAv2 prototypes operated with xenon and argon at 1 sccm and a frequency of 2450 MHz; results of the DEEVAv2-attractive configuration are represented by the squares and triangles, and those of the DEEVAv2-repulsive configuration by the points and diamonds. Results of the thruster operation with xenon is shown in blue, with argon in green. The standard deviation from multiple measurements taken, can be seen as underlying shadows of the measured data points.

1 mN with both xenon and argon at approximately 100 W of input power. The operation with xenon is represented in blue, while argon operation is depicted in green. The standard deviation of multiple measurements is indicated by the shaded regions around the data points. At higher power levels, argon produces higher thrust in repulsive configuration compared to xenon. In both cases, the thruster in repulsive configuration slightly outperforms the thruster in attractive configuration. The higher thrust observed with xenon at lower power settings can be attributed to the higher mass of xenon ions compared to argon ions. The higher input power required by the DEEVAv2 prototypes to achieve thrust levels similar to those of the MINOTOR prototype, as seen in Figure 25, can be explained by power losses due to the waveguide characteristics of the SLAN antenna. The issue of waveguide coupling was discussed in Chapter 2 where a decrease in performance due to power losses was observed in earlier studies. The electrodeless coupling mechanism in DEEVA appears to necessitate higher power input compared to the coaxial coupling used in MINOTOR.

Thruster Efficiencies

Using the thrust balance results shown in Figure 25, we can calculate the thrust efficiencies based on Equation 2.4, which takes into account the input power, xenon volume flow, and measured thrust. In this calculation, we assume that the gas is at room temperature to convert the volumetric flow in sccm to a mass flow in kg/s. Figure 28 displays the thrust efficiencies across different input power settings for the four prototypes, all thrusters were operated with xenon flow rates of 1 sccm and at a frequency of 2450 MHz. The MINOTOR prototype demonstrates efficiencies of around 10 to 11 %. The DEEVAv2 prototype in its repulsive configuration shows a stable efficiency of approximately 4 % across varying power levels. The DEEVAv2-attractive configuration exhibits a slight increase in efficiency at higher power settings, from about 0.5 % up to 3 %. The DEEVAv1 prototype shows much lower efficiencies of about 0.1 %. The shaded regions in the figure represent the standard deviations from multiple thrust measurements. As expected, given that the MINOTOR prototype produces the highest thrust in the selected power range, its efficiency is the highest. However, when compared to the literature (see Chapter 2), our measured efficiencies are slightly lower: while the literature reports efficiencies as high as 16 % for the MINOTOR prototype, our results do not exceed 12 %. If

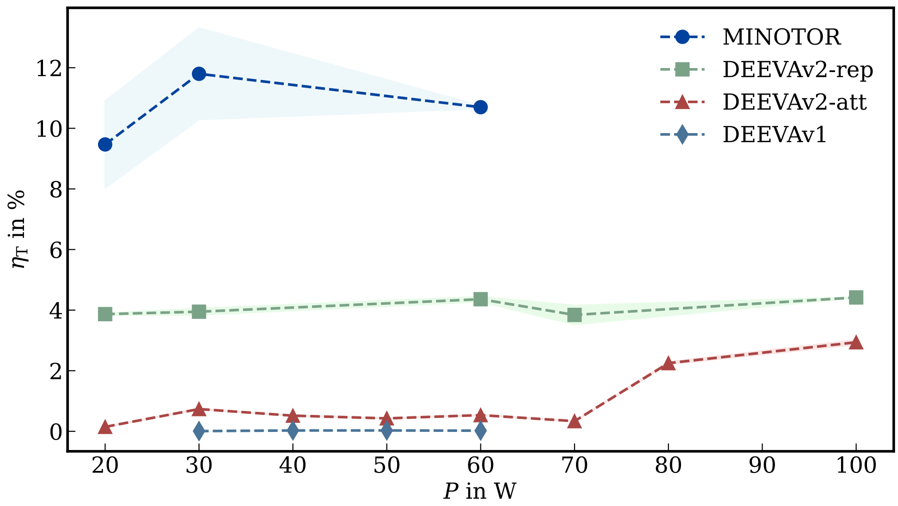

Figure 28: Thrust efficiency over different input power of the prototypes operated with xenon flow rates of 1 sccm and a set frequency of 2450 MHz. The efficiencies are calculated by Eq. 2.4. The underlying shadow shows are the standard deviation of the results from multiple thrust measurements.

this is due to the smaller chamber and therefore indeed decreased performance of the MINOTOR prototype - or due to the different diagnostic tools and methods employed, is still open for discussion. However, this discrepancy between literature values and results determined with our set-up gives additional motivation to perform comparison measurements between the two EP-concepts within the same vacuum chambers with the same diagnostic tools. The adjustment of the magnetic field topology in the DEEVAv2-repulsive configuration seems to improve its performance compared to the attractive configuration. The DEEVAv1 prototype exhibits the lowest efficiency of all the prototypes tested.

However, as the microwave coupling is not the only contributing factor to the overall performance of the prototypes and given the results in the smaller power ranges, the question remains: Why does the MINOTOR prototype produce the highest measured thrust?

3.3. Magnetic Field Topology

First, we discuss the magnetic field topologies of the four thruster prototypes under investigation. In Figure 29, the magnetic field topologies of the thruster prototypes in the x, y plane is shown. The colormap represents the magnetic flux density (the absolute value based on $B_\mathrm{x}, B_\mathrm{y}, B_\mathrm{z}$), while the streamlines are guides to the eye to illustrate the magnetic field lines in the x and y directions (i.e., $B_\mathrm{x}, B_\mathrm{y}$). The black masks indicate the parts of the prototypes inaccessible to the Hall probe. The line $y = 0$ marks the downstream plane of the ring magnet, and in case of MINOTOR, it also marks the tip of the inner conductor - this is referred to as the thruster exit plane for all the prototypes. This plane represents the wall-free region of the thruster system, where the beam can expand without wall losses. The line $x = 0$ marks the centerline of the thruster. To indicate where the ECR condition is met for the frequency of 2450 MHz (requiring a field strength of 87.5 mT), white lines are used to show the ECR zone. These white lines represent the constant-value line of 87.5 mT.

For the MINOTOR thruster, the ECR condition is met right at the back wall of the thruster. Additionally, the strictly diverging nature of the magnetic field lines supports the direct acceleration of the quasi-neutral plasma. A qualitative comparison with literature values indicates that the ECR zone has shifted slightly towards the back wall in recent years, likely due to the degradation of the permanent magnets in use. Magnetic field degradation has also been observed in the DEEVA prototypes. Comparative measurements show that after roughly 30 hours of operation, measurable degradation of the magnets occurs which is reflected in smaller magnetic field values. The primary cause of this degradation is believed to be the thrusters' operating temperature. Already below the Curie temperature (about 350°C for neodymium-iron-boron magnets) at about 80°C, a permanent degradation of the permanent magnets is to be expected. Thruster temperatures approaching 70°C were determined after prolonged operation of the DEEVA prototypes at higher power levels in earlier campaigns. To ensure accurate correlation between the magnetic field topology and the measured thrust, plasma, and beam parameters, another magnetic field mapping was conducted just before the measurement campaigns. Excerpts of the magnet degradation measurement campaigns are detailed in the Appendix.

As seen in Figure 29 on the top right, the ECR condition for the DEEVAv1 prototype at 2450 MHz is not met, since the maximum field strength only reaches 60 mT. Therefore, no white line is shown for this prototype. It should be clarified that the measured magnetic fields are those detectable by the Hall probe. Due to an unavoidable distance from the quartz glass wall, it may be possible that the ECR condition is met closer to the quartz walls. This aligns with observations that, in the case of the DEEVAv1, the discharge takes the form of a ring, as shown in the photograph in Figure 30. Since, if fulfilled at all, the ECR condition is met in a small region of the quartz tube only, plasma production will be weaker compared to the other prototypes. Furthermore, since the magnetic field lines strongly converge where the ring magnet is located, plasma particle reflection will occur due to the magnetic mirror effect, as described in Chapter 2. Moreover, when the thruster potential for this prototype was investigated, a negative thruster floating potential of about -5 V was observed, which can be explained by the cusp field forming around the ring magnet. It leads to the capture of electrons and a negative thruster potential, which in turn can negatively influence ion acceleration. These observations are discussed in the next subsection in more detail.

For the DEEVAv2-attractive configuration, the ECR condition is met on the upstream part of the SLAN, extending across the entire diameter of the quartz tube. The magnetic field lines exhibit a slight asymmetry, which may be due to probe misalignment with the magnets or changes in the magnets' properties after extended operation. Nonetheless, the field lines show a diverging pattern towards the thruster exit plane. After a small converging section immediately following the thruster exit at $y = 0$, the magnetic field becomes strictly divergent.

In the DEEVAv2-repulsive configuration, the magnetic field lines display greater symmetry and maintain a strictly diverging pattern toward and beyond the thruster exit plane. Around $-20\,\mathrm{mm} < y < -10\,\mathrm{mm}$ parallel behavior of the magnetic field lines can be observed. The absence of a converging region ensures that no particle reflection back into the plasma vessel occurs at the bottleneck of the magnetic bottle, as described in Chapter 2.

To better understand the influence of the magnetic field gradient on plasma acceleration, according to Equation 2.38 - Figure 31 shows the magnetic flux density along the centerline of each thruster. Since the MINOTOR prototype has a much shorter discharge chamber compared to the DEEVA prototypes, its curve starts at y = -20 mm. In contrast, the probe can access the SLAN of the DEEVA prototypes (v1 and v2) to a much greater depth. The exit planes for all four configurations are marked at $y = 0\,\mathrm{mm}$. Additionally, the ECR zones for the MINOTOR and DEEVAv2 prototypes are indicated by the two dotted lines. Since the magnetic flux density for the DEEVAv1 prototype does not reach 87.5 mT along the centerline, no ECR indication is provided for this prototype. For the DEEVAv1 prototype, the magnetic flux density increases towards the thruster exit plane, as indicated by the red region of converging magnetic field lines in Figure 31. Although the magnetic flux density decreases beyond the exit plane, its gradient is much lower compared to that of the MINOTOR prototype. The magnetic field gradient in the MINOTOR case is very steep, even in the area outside the thruster where the beam can expand freely without wall losses. In fact, even when compared to the DEEVAv2-repulsive configuration, which has a higher gradient than the attractive configuration, the magnetic field gradient of the MINOTOR is steeper than in any DEEVA version. The ECR zones for the DEEVAv2-attractive and repulsive configurations are located at the same position, which is expected since the strong disc magnets at the back of the thruster, responsible for the magnetic flux

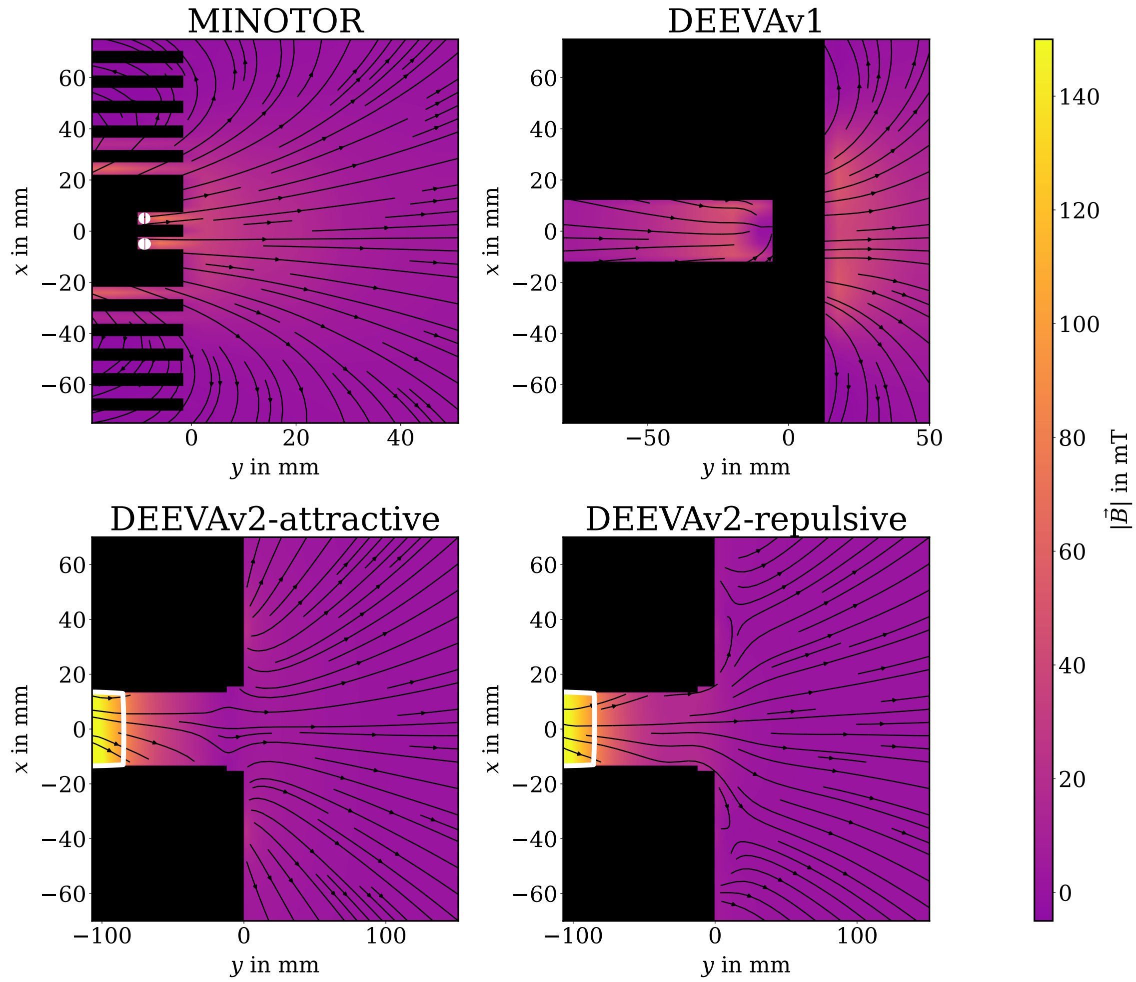

Figure 29: Magnetic field topologies of the thruster prototypes in the x, y plane. On the left of the top row are the measured results of the MINOTOR thruster, on the top right are those of the DEEVAv1 prototype. On the left on the bottom row are the results of the DEEVAv2 thruster in attractive configuration, on the bottom right those of the DEEVAv2 prototype in repulsive configuration. The black masks mark the part of the prototypes inaccessible to the Hall probe. The position $y = 0$ marks the position of the downstream plane of the ring magnet and in case of MINOTOR the tip of the inner conductor - ergo the thruster exit plane. The position $x = 0$ denotes the centerline of the thruster. The colourmap depicts the magnetic flux density, while the streamline vectors indicate the magnetic field topology in x and y direction. The white line corresponds to a magnetic flux density of 87.5 mT and marks the ECR zone for the set microwave frequency of 2450 MHz for all the prototypes beside DEEVAv1, as here 87.5 mT is not reached.

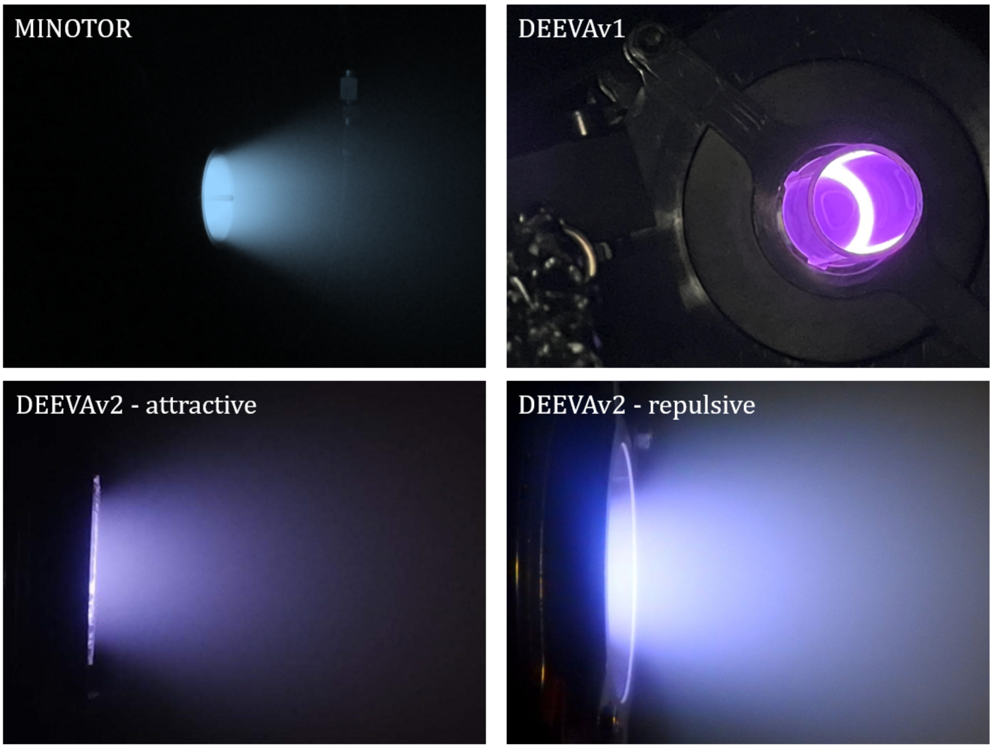

Figure 30: Photographs of the beam exiting the thruster prototypes during operation. On the left on the top row the MINOTOR prototype can be seen, with the inner conductor visible and the divergent beam. On the right on the top row, the discharge of the DEEVAv1 prototype is shown. The discharge takes the form of a ring and no extracted beam is visible. In the bottom row, the two configurations of the DEEVAv2 prototype are depicted. On the bottom left, the plasma beam of the DEEVAv2-attractive configuration can be seen, and on the right the extracted plasma of the DEEVAv2-repulsive configuration. All images are taken in the small STG-MT vacuum chamber. MINOTOR and DEEVAv1 were operated with xenon when the photographs were taken, while the DEEVAv2 prototypes were operated with argon as propellant.

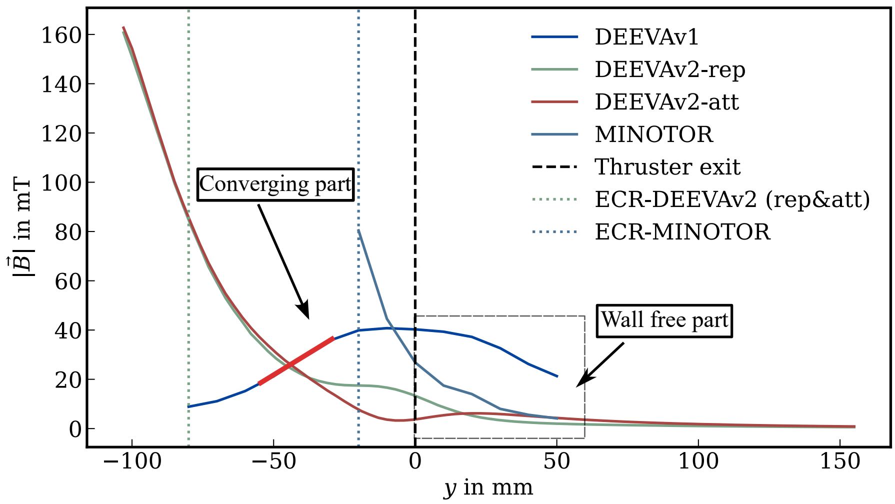

Figure 31: Magnetic flux density along the centerline of the ECR thruster configurations. Due to the shorter discharge chamber of the MINOTOR prototype, the magnetic field curve starts at y = -20 mm, while the probe can access the slotted antenna to a greater depth in the DEEVA prototypes (v1 and v2). The exit planes for all four configurations are marked at $y = 0$ mm by a black dashed line. The ECR zones corresponding to the frequency of 2450 MHz for the MINOTOR and DEEVAv2 prototypes are shown as dotted lines. Since the magnetic flux density of the DEEVAv1 prototype does not reach 87.5 mT along the centerline, no ECR indication is provided. The converging part of the magnetic field lines of the DEEVAv1 prototype is highlighted in red. Additionally, the free expansion region of the prototypes, beyond the thruster exit, is marked by the grey-dashed box.

density required for the ECR condition, are identical in both versions. Both configurations exhibit a high magnetic field gradient, but still within the walls of the quartz glass tube. In the case of the DEEVAv2-attractive configuration, we observe an increase in magnetic flux density just after the thruster exit plane, where acceleration is intended to occur. However, downstream of the thruster, there is almost no further change in magnetic flux density. The DEEVAv2-repulsive configuration behaves differently. Its magnetic field distribution exhibits a plateau just before the thruster exit plane, indicating an area where the magnetic field lines are parallel. Right at the thruster exit, a decrease in magnetic field creates a gradient that contributes to particle acceleration. This observation reinforces the assumption that the DEEVAv1 prototype is less suited for plasma production or acceleration, as its magnetic flux density is insufficient for efficient plasma generation, and its converging-diverging magnetic field topology may cause particle deflection at the magnetic bottle neck. Although the DEEVAv2-attractive configuration approaches the ideal/reference topology of the MINOTOR prototype - ensuring the ECR condition is met - it lacks a sufficiently high magnetic field gradient to accelerate the plasma efficiently. The DEEVAv2-repulsive configuration appears better suited, as it not only fulfills the ECR condition but also avoids converging magnetic field lines, and the gradient outside the thruster allows for plasma acceleration comparable to that of the MINOTOR prototype.

3.4. Magnetic Nozzle Effects

3.4.1. Energy Distribution Functions

Examples of the determined ion energy distribution functions ($\mathrm{d}I/\mathrm{d}U$) for all the thruster prototypes can be seen in Figure 32. The MINOTOR and DEEVAv1 prototype were operated with xenon as propellant, the DEEVAv2 configurations were operated with xenon and argon as propellant. Observation reveals that the measured current value of the MINOTOR prototype exceeds the current of the plume of the DEEVA prototypes by a factor of 10^6 (MINOTOR in the A range, DEEVA in the µA range).

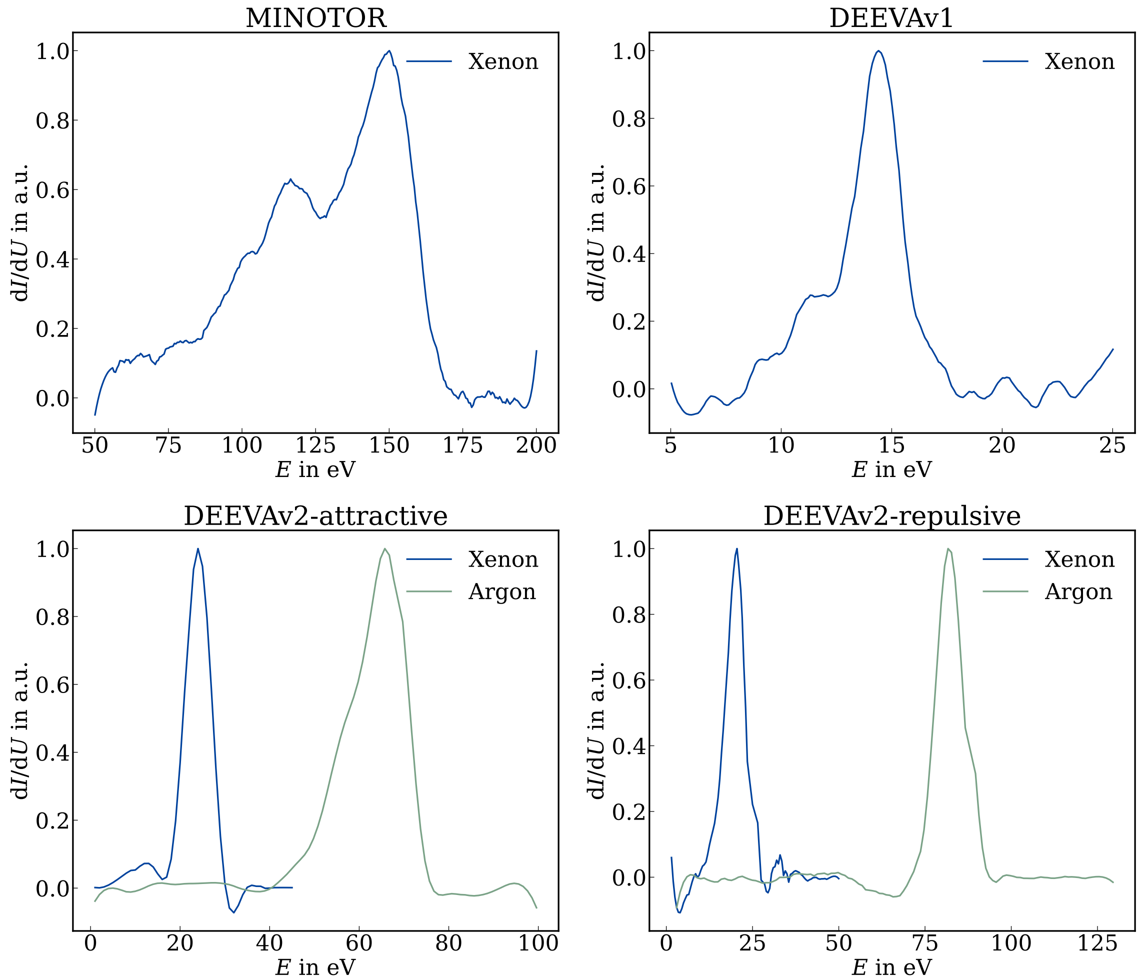

Figure 32: Ion energy distribution functions ($\mathrm{d}I/\mathrm{d}U$). The MINOTOR and DEEVAv1 prototype (results in the top row) were operated with xenon as propellant, the DEEVAv2 configurations (results on the bottom row) were operated with xenon or argon as propellant. All prototypes and configurations were operated at 2450 MHz, 1 sccm and 30 W microwave power. The energy E on the x-axis can be interpreted as kinetic energy of the ions. The y axis shows the first derivative of the voltage sweep and its absolute value has no significance with respect to the determined ion energy of maximum probability, it is therefore normalized and without units.

This shows that there is much more ion current exiting the MINOTOR prototype than the DEEVA thruster. However, since we cannot estimate the effect of additional charge species existing between the grids (which can change the electric potential and therefore influence current measurements), a quantitative determination of the ion density in the beam is not reliably possible with this set up. We therefore normalize the current values and give no units on the y axis in Figure 32. We show sections of the spectrum as a demonstration. The measurement procedure includes a scan of the spectrum from 0 to 200 V to identify the drop in the raw current measurement. Afterwards several measurements with a higher resolution of up to 0.1 V are performed, from which standard deviations of the most probable ion energies can be determined. Examples of these high-resolution measurements are shown in Figure 32. We focus on determining the ion energy of maximum probability and the ion energy distribution function (IEDF). The latter is determined by the first derivative of the measured current, the maximum of this distribution function is then the most probable ion energy $E_{\mathrm{i,max}}$. In these examples the determined ion energy with the maximum probability in case of MINOTOR is $E_{\mathrm{i,max}} \approx 150\,\mathrm{eV}$ and in case of DEEVAv1 is $E_{\mathrm{i,max}} \approx 15\,\mathrm{eV}$ for xenon. For DEEVAv2 in attractive configuration, it is $E_{\mathrm{i,max}} \approx 22\,\mathrm{eV}$ with xenon and $E_{\mathrm{i,max}} \approx 65\,\mathrm{eV}$ with argon as propellant. For the DEEVAv2-repulsive configuration, it is $E_{\mathrm{i,max}} \approx 24\,\mathrm{eV}$ for xenon and $E_{\mathrm{i,max}} \approx 85\,\mathrm{eV}$ for argon operation. In the here presented examples for MINOTOR a bi-Maxwellian character of the IEDF is determined, while for the DEEVA prototypes mostly Maxwellian distributions are observed. In particular, we find that for all DEEVA configurations the operation with xenon yields Maxwellian distributions of the ion energies, while when operated with argon in some cases we also observe bi-Maxwellian distributions.

Examples of the determined electron energy distribution functions $f(E)$ can be seen in Figure 33. Again, the MINOTOR and DEEVAv1 prototype were operated with xenon as propellant, the DEEVAv2 configurations were operated with either xenon or argon as propellant. The Langmuir probe was placed at a 10 cm distance from the thruster exit. The voltage U can then be interpreted as energy E in eV of the electrons. In these examples the determined electron temperature - derived from integration of the function (see Equation 2.42) - is $T_{\mathrm{e}} \approx 16\,\mathrm{eV}$ in case of MINOTOR. In case of DEEVAv1, it is $T_{\mathrm{e}} \approx 3.5\,\mathrm{eV}$, for DEEVAv2 in attractive configuration, it is $T_{\mathrm{e}} \approx 3\,\mathrm{eV}$ with xenon and $T_{\mathrm{e}} \approx 5\,\mathrm{eV}$ with argon as propellant. For the DEEVAv2-repulsive configuration, it is $T_{\mathrm{e}} \approx 2\,\mathrm{eV}$ for xenon and $T_{\mathrm{e}} \approx 9.5\,\mathrm{eV}$ for argon operation. We observe a broadened Maxwellian shaped distribution function for MINOTOR, leading to the highest temperature in this set of examples. The DEEVA prototypes operated with xenon all exhibit sharp Maxwellian-like shaped distributions of electron energy, at the very low energy range (below 10 eV). The non-physical values below zero in the energy distribution are a consequence of the difficulty to measure at extremely low electron energies and is therefore an artifact from the filtering process. Interestingly in the here presented examples the peak heights for the operation with xenon are higher than for the operation with argon in DEEVAv2-attractive and DEEVAv2-repulsive case. However since the distributions in case of argon operation lie in the 10 to 30 eV range, the resulting electron temperature is higher, if the DEEVAv2 prototype is operated with argon. Furthermore, in the repulsive configuration of the DEEVAv2 prototype, we observe a broadened peak that may even be interpreted as a bi-Maxwellian character of the EEDF with one peak in the range of 20 eV and the other in the range of 10 eV. In some of the results shown in what follows, this bi-Maxwellian character is more pronounced.

3.4.2. Influences of Experimental Set Up

To support the credibility of the presented results, we would like to emphasize that the LP and RPA measurements have been confirmed using different probes in different chambers during preliminary tests. The results presented in Figure 32 and Figure 33 are obtained in the small STG-MT chamber, but RPA measurements were also conducted at the BigMac facility at the JLU Giessen using a custom-built four-grid RPA. Additionally, LP measurements were performed in the JUMBO facility at JLU.

Comparison of the RPA measurements on the MINOTOR prototype performed in the BigMac facility and the STG-MT facility can be seen in Figure 34. The observation is made that even though the distance is higher within the BigMac facility and a collimator is used (automatically reducing the

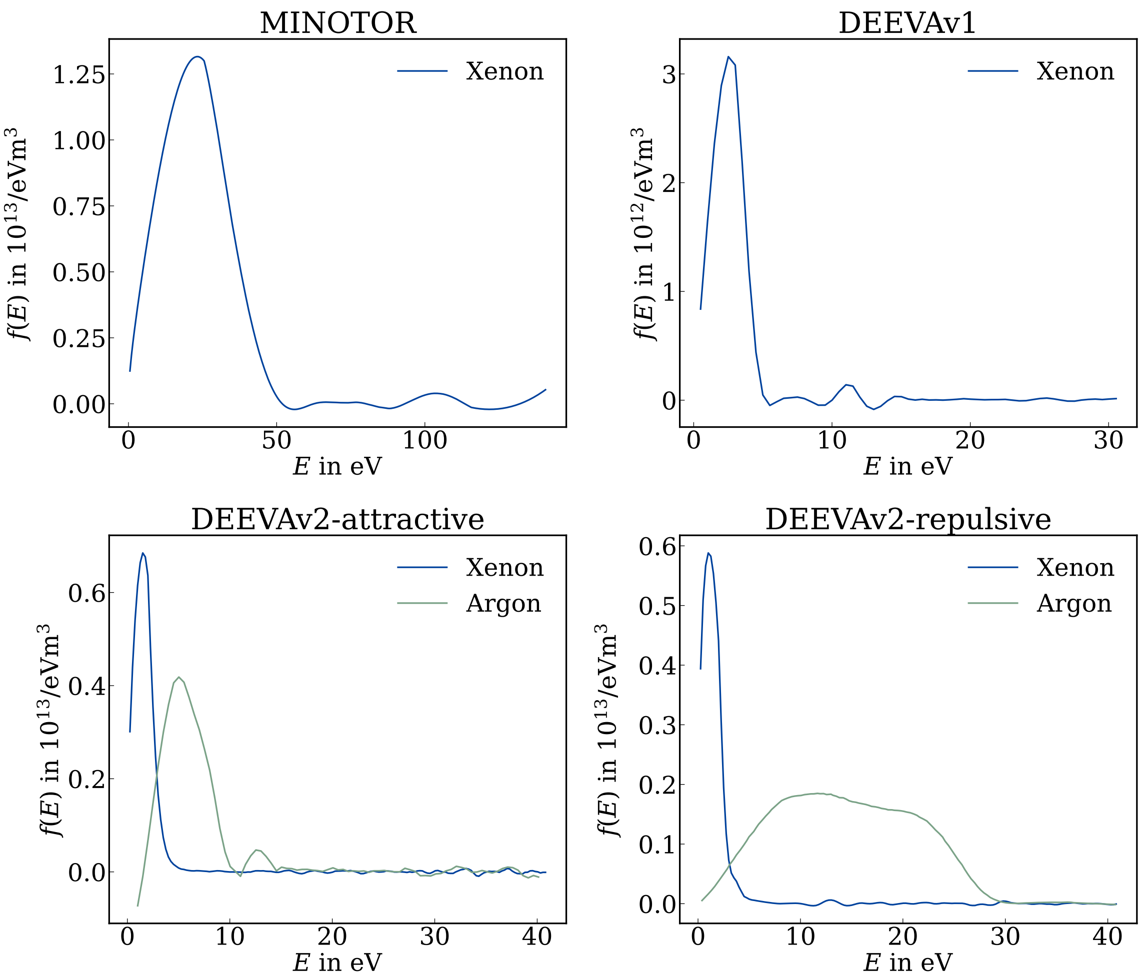

Figure 33: Examples of the determined electron energy distribution functions $f(E)$. The MINOTOR and DEEVAv1 prototype (results on the top row) were operated with xenon as propellant, the DEEVAv2 configurations (results on the bottom row) were operated with either xenon or argon as propellant. All prototypes and configurations were operated at 2.45 GHz, 1 sccm and 30 W microwave power.

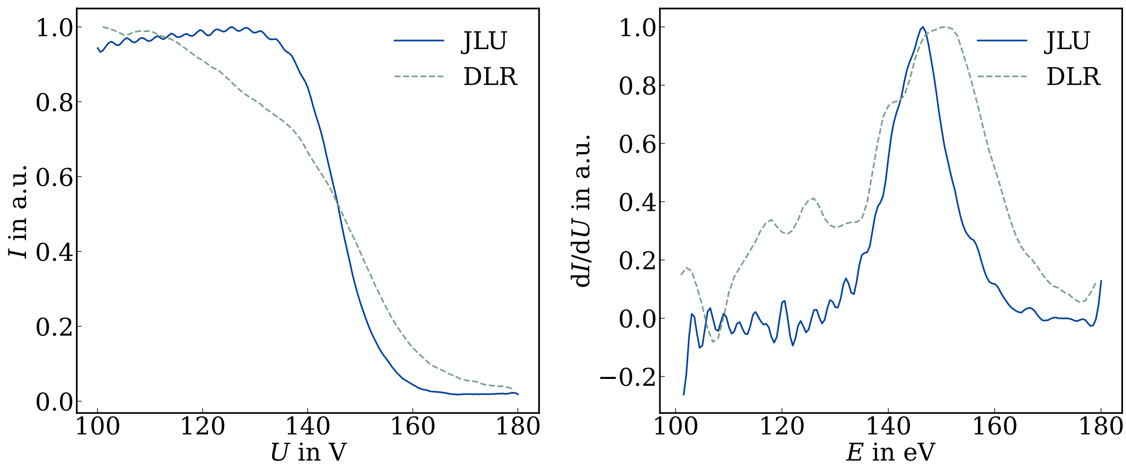

Figure 34: Comparison of IEDF measurements on the MINOTOR prototype performed in the BigMac facility (labeled as JLU) and the STG-MT facility (labeled as DLR). The MINOTOR prototype was operated with xenon at 1 sccm, 30 W input power and a microwave frequency set of 2450 MHz. The thruster was operated in both cases in floating condition. The RPA at JLU was placed at a distance of 30 cm from the thruster's exit plane and in the STG-MT at 10 cm. The RPA used at JLU is an in-house built 4-grid RPA, equipped with an 22 cm long collimator - i.e. the tip of the collimator, with an aperture of 1 mm was placed at a distance of 8 cm from the thruster exit plane. As the absolute current values are not necessarily relevant in this investigation, the current I is normalized and set to arbitrary units for comparison. The same holds for the first derivative shown in the plot on the right. On the left, we see the raw current measurements versus the sweeping voltage U. On the plot on the right we see the first derivative $\mathrm{d}I/\mathrm{d}U$ of this measurement, i.e. the IEDF. The voltage on the x axis on the left can be interpreted as energy in eV, as shown as E on the right plot.

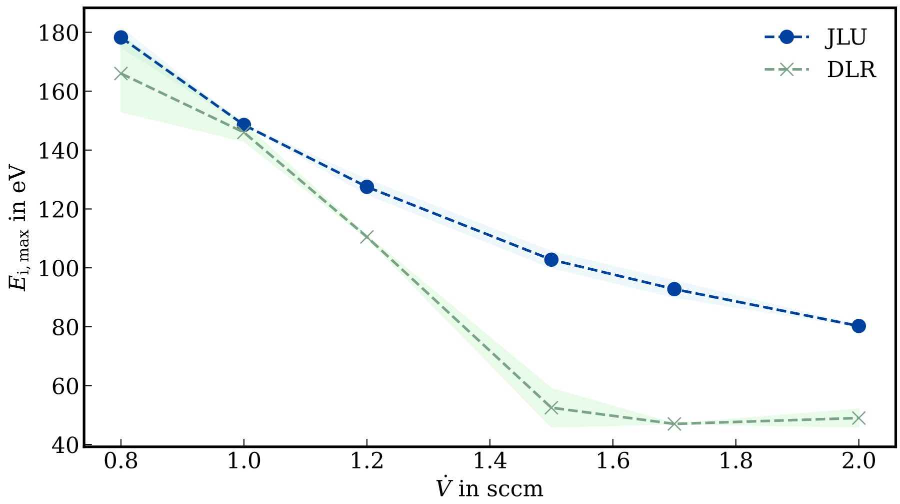

Figure 35: Comparison of the ion energy of maximum probability $E_{\mathrm{i,max}}$ of the MINOTOR prototype, determined from measurements performed in the BigMac facility (labeled as JLU) and the STG-MT facility (labeled as DLR). The MINOTOR prototype was operated with xenon at 30 W input power and a microwave frequency set of 2450 MHz at varying volume flow $\dot{V}$. The thruster was operated in both cases in floating condition. The set ups were the same as those used to acquire the data shown in Figure 34. The measurement uncertainty is depicted as underlying shadow - it is derived as the standard deviation from multiple measurements.

amount of charged particles entering the analyzer), the absolute current value is higher than in the STG-MT chamber. This can be explained by the larger size of the BigMac facility allowing smaller back-pressures, which is inherently linked to the thruster performance. The ion energy of maximum probability extracted from the measurements at JLU in the BigMac facility is about $E_{\mathrm{i,max}} \approx 145\,\mathrm{eV}$, whereas that obtained from measurements at DLR in the the STG-MT with the commercial RPA is somewhat higher, i.e. $E_{\mathrm{i,max}} \approx 153\,\mathrm{eV}$. This may be due to the smaller chamber, or due to the different RPAs in use.

Figure 35 shows a comparison of the ion energy of maximum probability $E_{\mathrm{i,max}}$ obtained for the MINOTOR prototype from measurements in the BigMac facility (labeled as JLU) and in the STG-MT facility (labeled as DLR). In the measurements performed at the JLU, we determine slightly higher ion energies of maximum probability. The difference is bigger especially for the higher volume flow regions, while for the smaller volume flows the difference lies within the error bars. It is expected that the volume flow variation is the most sensitive operational variable with respect to background pressure. As we present results in the lower volume flow ranges in course of this work, the similarity of the ion energies determined in two chambers using different RPAs confirms the accuracy of our detection methods and supports the values presented in this work in the lower volume flow range.

The comparison of the LP measurements, specifically the results of the EEDF analysis of the data of the MINOTOR prototype, conducted at the JUMBO facility (labeled as JLU) and the STG-MT facility (labeled as DLR), are shown in Figure 36. In both cases, a bi-Maxwellian energy distribution of the electrons is observed, suggesting the presence of two distinct electron temperatures. This bi-Maxwellian characteristic seen in this example but not in those shown in Figure 33, can be explained by the proximity of the probes to the thruster, where the influence of the magnetic field is more pronounced. The EEDFs presented in Figure 33 are measured at a distance of 10 cm using the same chamber and probe, but here no bi-Maxwellian behavior is detected. This indicates that, as the distance from the thruster increases and the influence of the magnetic field decreases, the electrons thermally relax and their energy distribution becomes more uniform. Further details on the effect of

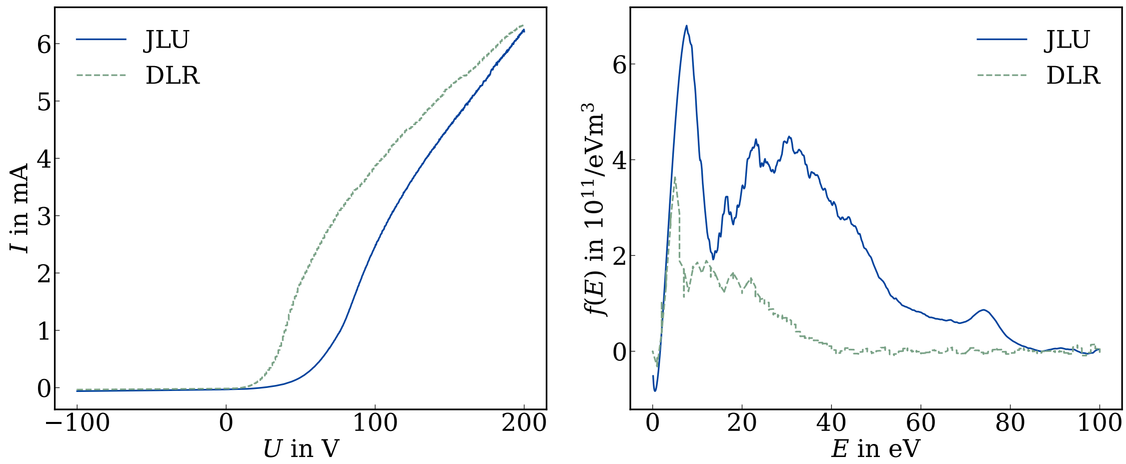

Figure 36: Comparison of the EEDF measurements on the MINOTOR prototype performed in the JUMBO facility (labeled as JLU) and the STG-MT facility (labeled as DLR). The MINOTOR prototype was operated with xenon at 1 sccm, 22 W input power and a microwave frequency set of 2450 MHz. The thruster was operated in both cases in floating condition. The single LP at JLU was placed at a distance of 6 cm from the thruster exit plane and in the STG-MT at 7 cm. In both cases, a parallel orientation with respect to the magnetic field lines was employed. On the left, we see the raw current measurements I versus the voltage sweep U. On the plot on the right, we see the determined EEDFs $f(E)$ over the energy E.

the magnetic field on probe measurements are discussed below. In this example, the measurement data obtained at JLU show a slightly higher electron temperature, around $T_e \approx 19\,\mathrm{eV}$, while at STG-MT (DLR), the electron temperature is approximately $T_e \approx 16\,\mathrm{eV}$.

Figure 37 presents a comparison of the electron temperature determined from measurements on the MINOTOR prototype conducted at the JUMBO (JLU) and STG-MT (DLR) facilities. In both vacuum chambers we observe a decrease in electron temperature of the plasma plume as the volume flow increases. The measurement results obtained at JLU consistently yield slightly higher electron temperatures, which can be attributed to the larger size of the JUMBO facility, resulting in lower and more stable background pressure, thereby improving the performance of the prototype.

As we measure a bi-Maxwellian electron energy distribution in close proximity to the thruster exit (compare Figure 33 and 36), we conclude that the influence of the magnetic field is in close proximity to the thruster very important. With increasing distance from the thruster the electrons thermally relax and distribute equally, compare Chapter 2. The influence on probe orientation with respect to the magnetic filed lines in close proximity to the thruster exit plane is exemplary shown in Figure 38. The single LP was placed at a distance of 6 cm in parallel and orthogonal orientation. We observe for parallel orientation a bi-Maxwellian character of the energy distribution of the electrons - leading to the assumption of two electron temperatures present. In the orthogonal orientation we see a nearly Maxwellian distribution. In parallel orientation - at the same position, at the same thruster operational point, in the same chamber with the same diagnostic tools - we determine a higher electron temperature - around $T_e \approx 19\,\mathrm{eV}$, while in orthogonal orientation an electron temperature of only $T_e \approx 16\,\mathrm{eV}$ is determined.

Investigations indicate that the orientation of the probe only influences measurements when placed very close to the thruster. Therefore, in the presented LP results, the probe is consistently oriented parallel to the magnetic field lines and positioned at least 10 cm from the thruster exit. Overall, it can be concluded that, despite differences in test chambers and diagnostics, similar values for both RPA and LP measurements are obtained, with results falling within the same order of magnitude.

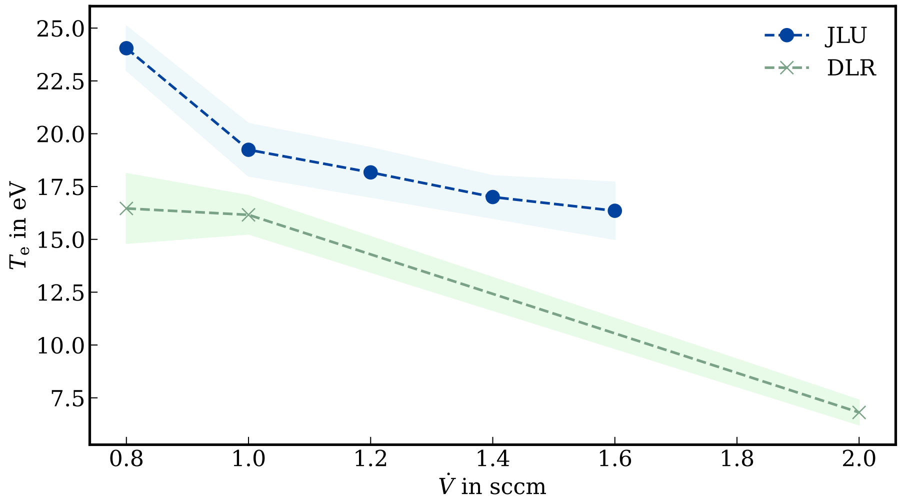

Figure 37: Comparison of the electron temperature measurements on the MINOTOR prototype performed in the JUMBO facility (labeled as JLU) and the STG-MT facility (labeled as DLR). The MINOTOR prototype was operated with xenon at 22 W input power and a microwave frequency set of 2450 MHz at varying volume flow $\dot{V}$. The thruster was operated in both cases in floating condition. The single LP at JLU was placed at a distance of 6 cm and in the STG-MT at 7 cm. In both set ups, the probe was oriented parallel with respect to the magnetic field lines.

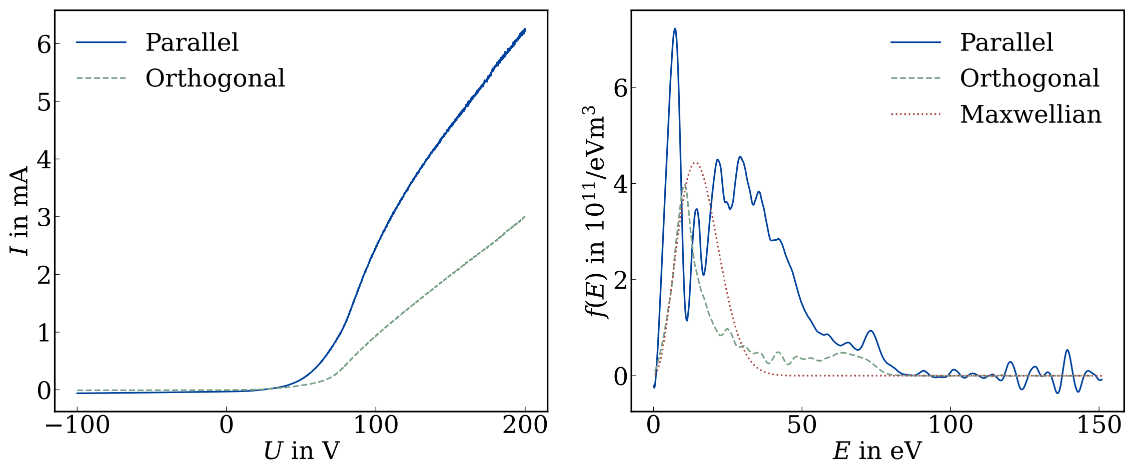

Figure 38: Excerpts of the EEDF comparison measurements on the MINOTOR prototype performed in the JUMBO facility in parallel and orthogonal orientation of the LP towards the magnetic field lines. In this example the MINOTOR prototype was operated with xenon at 1 sccm, 22 W input power and a microwave frequency set of 2450 MHz. The thruster was operated in both cases in floating condition. The single LP was placed at a distance of 6 cm in parallel and orthogonal orientation. On the left we see the raw current measurements I over the voltage sweep U. On the plot on the right we see the determined EEDFs $f(E)$ over the energy E. Additionally, an exemplary Maxwellian distribution for the determined electron temperature of 16 eV in orthogonal case is shown as dotted red line.

This consistency can be seen as further validation of the data, indicating that the measurements are not only reproducible using the same experimental setup (as evidenced by the presented standard deviations) but also reproducible across different set ups.

3.4.3. Correlation of Electron Temperature and Ion Energy

The correlation between electron temperature and ion energy is a key factor in magnetic nozzle design. Following previous research, we compare the trends and ratios of two important plasma parameters: electron temperature and ion energy of maximum probability [56, 78]. Figure 39 illustrates a simple comparison of these trends. The left axis shows the electron temperature T_e, while the right axis displays the ion energy E_i as a function of volume flow. With increasing volume flow, both the electron temperature and ion energy decrease for all prototypes. This aligns with literature findings for the MINOTOR prototype [34], and can be attributed to a reduction in the mean free path length of ions due to higher neutral gas density. A clear correlation between electron temperature and ion energy is observed across all prototypes. However, in the case of the MINOTOR prototype, higher electron temperatures (up to 16 eV) and ion energies (up to 180 eV) are recorded. In contrast, the DEEVAv1 prototype shows lower values, with electron temperatures between 3 to 4 eV and ion energies of about 19 eV. Similar values are observed for the DEEVAv2 prototype when operated with xenon. Interestingly, when the DEEVAv2 prototype is operated with argon, higher electron temperatures are measured, reaching up to 7 eV in the attractive configuration and up to 10 eV in the repulsive configuration. Corresponding higher ion energies, up to 140 eV, are also observed in both configurations. According to the literature, a correlation factor between ion energy E_i and electron temperature T_e can be defined as the ratio E_i/T_e [56, 11]. As an example, Figure 40 presents the correlation factors for the four prototypes in dependence of volume flow. In the DEEVAv2-attractive configuration, ratio values between 15 and 20 are found, while for the DEEVAv2-repulsive configuration, values between 10 and 15 are measured. For the MINOTOR prototype, ratio values of about 10 are determined, whereas for the DEEVAv1 prototype, values closer to 5 are observed. As already discussed in Chapter 2, literature reports correlation values of about 4 to 6 for the MINOTOR prototype [56, 11]. The discrepancy with our measurements may be due to the lower electron temperatures and ion energies we observe. Whether this is a result of chamber effects or differences in probe and analysis methods remains open for discussion.

In the analysis of the RPA results, it is noted that while bi-Maxwellian IEDFs are often observed for the MINOTOR prototype, the DEEVAv1 prototype typically exhibits a single Maxwellian distribution, as shown in Figure 32. This is also true for the DEEVAv2 prototype when operated with xenon. However, for DEEVAv2 operation with argon (in both attractive and repulsive configurations), we observe both bi-Maxwellian and Maxwellian IEDFs, depending on the operating conditions. When discussing ion energies, we refer to the ion energy at the maximum peak - therefore as the ion energy with maximum probability.

3.5. The Ion Energy with Maximum Probability

A comparison of the maximum ion energies for varying power inputs, including DEEVAv2 operation with xenon, is shown in Figure 41. The ion energy increases for all prototypes with rising power, though at different rates. MINOTOR shows the highest values overall, and the increase with input power is greater than those of the other prototypes. The measured values are generally consistent with those reported in the literature, except for the 30 W setting, where the values are slightly lower. Literature reports over 200 eV at 30 W for a similar MINOTOR prototype [63]. Whether this difference arises from the use of a different MINOTOR prototype, magnetic field degradation, chamber effects, probe sensitivity, or different analysis approaches remains open for discussion. We observe a maximum ion energy of up to 250 eV in case of the MINOTOR prototype, while the second-highest energy (DEEVAv2-repulsive-argon operation) reaches up to 100 eV. Argon operation in DEEVAv2

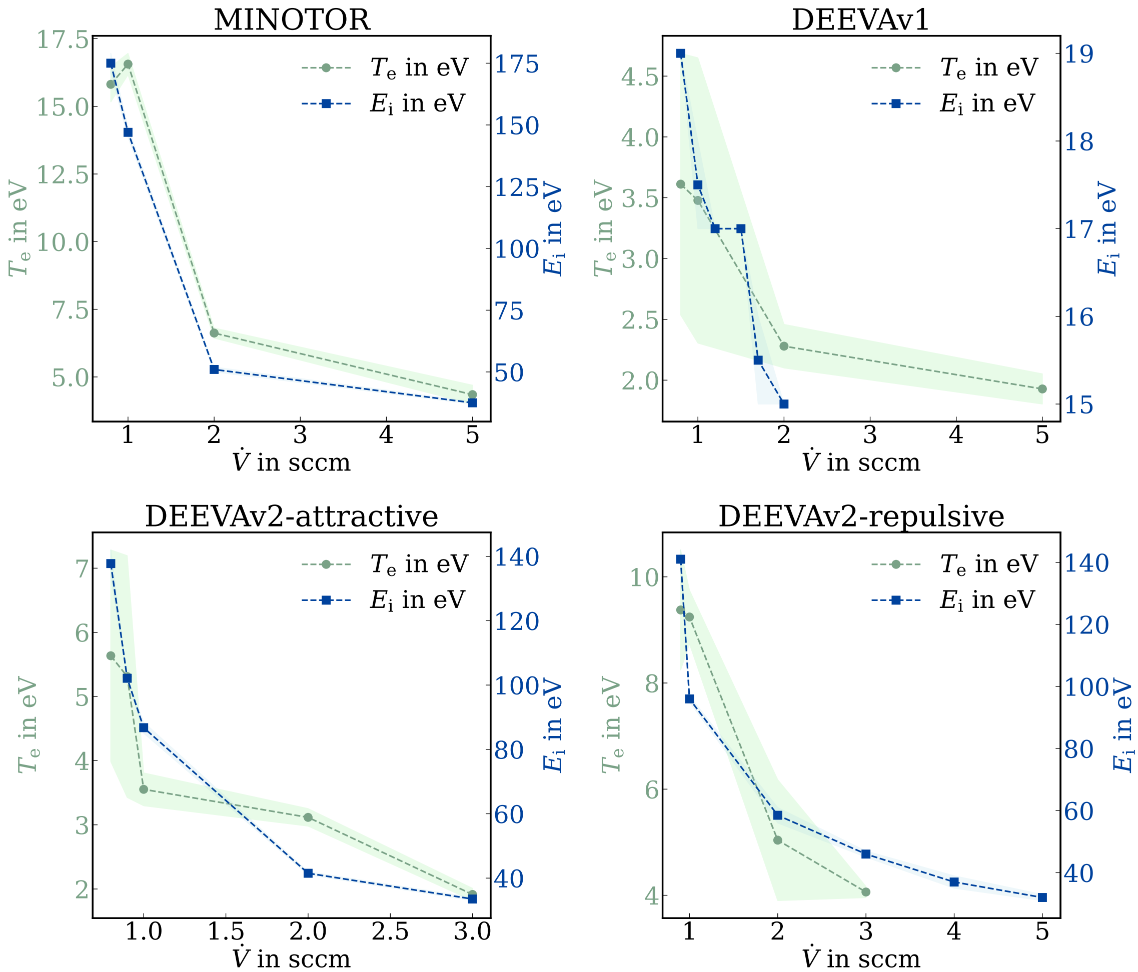

Figure 39: Electron temperature T_e and ion energy with maximum probability E_i measured for the four thruster configurations as a function of volume flow $\dot{V}$. The electron temperature can be seen in green on the left scale, the maximum ion energy in blue on the right scale. The MINOTOR and DEEVAv1 prototype were operated with xenon as propellant, the DEEVAv2 configurations were operated with argon as propellant. All prototypes were operated at 2450 MHz and 30 W microwave power. The standard deviation from multiple measurements taken, can be seen as underlying shadows of the measurement points.

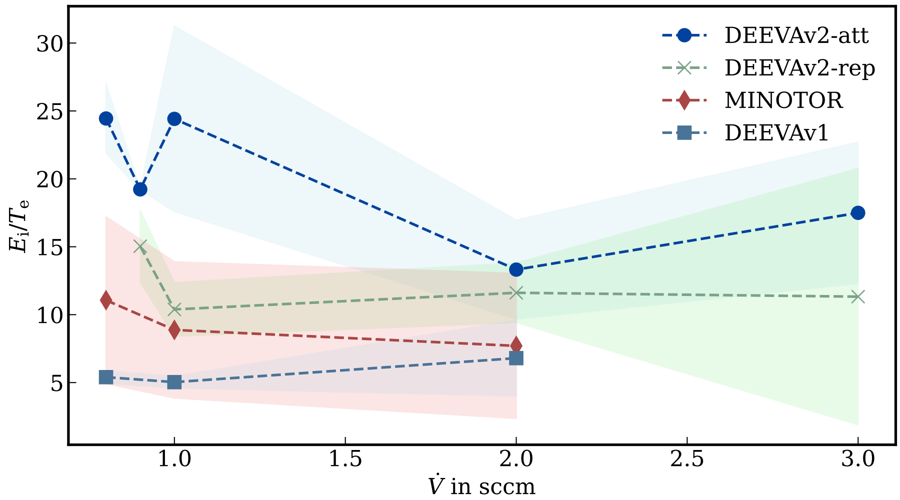

Figure 40: Ratio of electron temperature T_e and ion energy E_i for the four thruster configurations as a function of volume flow $\dot{V}$. The MINOTOR and DEEVAv1 prototype were operated with xenon as propellant, the DEEVAv2 configurations were operated with argon as propellant. All prototypes were operated at 2450 MHz and 30 W microwave power. The standard deviation from multiple measurements taken, can be seen as underlying shadows of the measurement points.

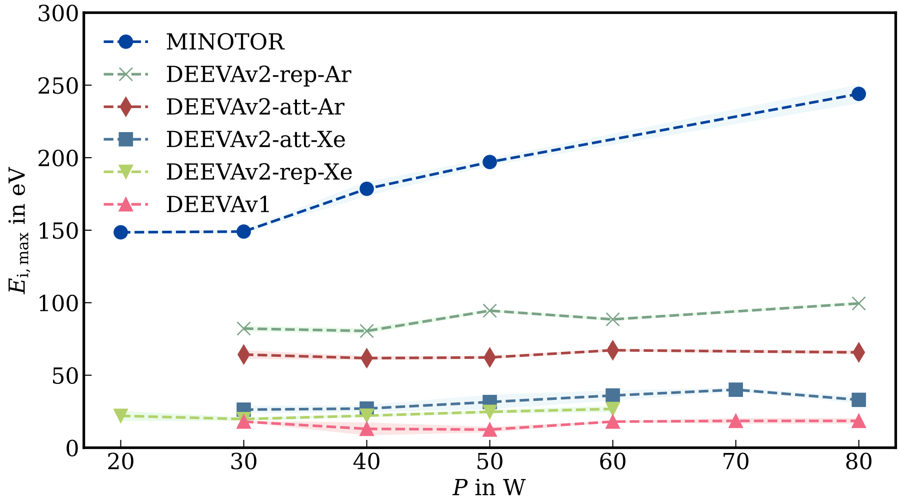

Figure 41: The ion energy of maximum probability $E_{i,max}$ measured for the different prototypes as a function of input power P. All prototypes were operated at 1 sccm of propellant and a microwave frequency of 2450 MHz. Xenon was used as propellant for MINOTOR and DEEVAv1; either argon or xenon were used as propellant for the two DEEVAv2 configurations. The standard deviation from multiple measurements taken, can be seen as underlying shadows of the measurement points.

configurations clearly yields higher ion energies than for xenon. The DEEVAv2-repulsive configuration with argon also produces higher energies than the attractive configuration. Due to the low ion energies in xenon operation, the difference between the repulsive and attractive configuration is not significant. DEEVAv1 consistently shows the lowest maximum ion energy. Although the differences in performance for the two propellants require further investigation, we can already correlate the magnetic field topologies to the observed magnetic nozzle effects, specifically the relationship between electron temperature and ion energy, and the magnitude of the ion energy itself. A strong argument can be made that the magnetic field topology with the steepest gradient (MINOTOR) produces the highest values of ion energy of maximum probability. Similarly, DEEVAv2-repulsive, with the second steepest gradient, shows the second-highest values of ion energy of maximum probability. DEEVAv2-attractive, with the third steepest gradient and ECR condition met, delivers lower values of ion energy of maximum probability, and the prototype with a converging-diverging magnetic field and possibly unfulfilled ECR condition (DEEVAv1) shows the lowest values of ion energy of maximum probability.

A comparison of the results depicted in Figures 39 and 41 shows that varying the volume flow has a greater effect on maximum ion energy than varying the power input as one would possibly assume. Of course microwave power influences plasma production, which indirectly affects plasma acceleration in the magnetic nozzle. Therefore, although the amount of absorbed microwave power does not directly accelerate the plasma, it still indirectly influences the acceleration process through its role in plasma production and heating. However, the dependencies observed as a function of volume flow of the propellant and power suggest that plasma dynamics play a significant role, beyond just the introduced power.

It should also be noted that in the raw data from the RPA and LP measurements, the signal for MINOTOR and DEEVAv2 with argon is much higher (in the mA range) than for the other configurations and the DEEVAv1 prototype. This indicates a higher current exiting the MINOTOR prototype compared to the DEEVA thruster. However, we cannot quantitatively determine ion density in the beam with the setup used, due to potential charge densities between the RPA grids, which may affect current measurements. Since ion current estimates are needed to determine the force contributions from MN effects, we performed FC measurements. Corresponding results are presented in the next subsections.

Potential Gradients

It is assumed that MN effects cause charge separation and the buildup of space charges, leading to ion acceleration. The potential gradients causing the acceleration of the ions can be related to the thruster floating potential (left graph in Figure 42) and the floating potential of the RPA (right graph in Figure 42, for the thruster in floating and grounded mode). As stated in the literature and in Chapter 2, the thruster potential can be directly correlated with ion energy, and hence with thrust. We compare the thruster potentials of the MINOTOR prototype, the DEEVAv2 prototype (in attractive configuration and operated with argon), and the DEEVAv1 prototype, as a function of volume flow. The MINOTOR prototype reaches thruster potentials exceeding 40 V at low flow rates. A positive thruster potential likely caused by heavier ions exiting the thruster body more slowly than electrons, contributes to ion acceleration. The DEEVAv2-attractive configuration also exhibits a positive thruster potential, though it remains below 20 V. In contrast, the DEEVAv1 prototype displays a negative potential, falling below -10 V. This negative potential can be explained by the cusp magnetic field surrounding the ring magnet, which traps electrons and prevents them from escaping the thruster body, thereby resulting in a negative thruster potential (see Figure 29). This negative potential will decelerate ions, further explaining the much lower ion energies observed for DEEVAv1 compared to the other prototypes. Additionally, we investigate the floating potential within the ion beam, measured using the floating grid of the RPA. When the thrusters are operated in floating mode, allowing the buildup of a thruster potential (as shown in the left plot of Figure 42), the floating potential is recorded simultaneously. This potential, denoted as $\Phi_{\mathrm{TW}} \neq 0$ in floating mode, affects ion acceleration: a negative floating potential results in a potential gradient that accelerates the ions, with larger

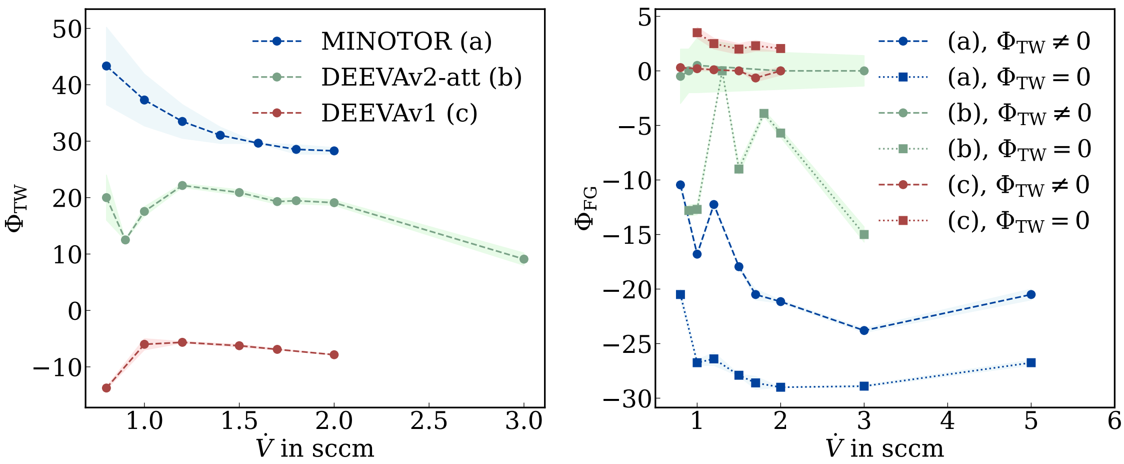

Figure 42: Study of the potential gradients causing ion acceleration in the three prototypes as a function of volume flow $\dot{V}$. All prototypes were operated at 2450 MHz and 30 W microwave power. The DEEVAv2 prototype in attractive configuration was operated with argon. On the left; thruster potential Φ_{TW}, the charged up potential for thruster operation in floating mode. In blue we see the MINOTOR prototype (a), in green the DEEVAv2 prototype - attractive configuration and operated with argon - (b), and in red the DEEVAv1 prototype (c). On the right; floating potential of the floating grid of the RPA Φ_{FG}. The dashed curves with the circle as markers show the potential when the thrusters are operated in floating mode, $\Phi_{TW} \neq 0$. The dotted lines show the floating potential when the thrusters are operated in grounded mode, $\Phi_{TW} = 0$. The filled space in the background shows the standard deviation of the mean when recording the potential for the durance of one minute.

gradients yielding larger acceleration. The shift from floating mode ($\Phi_{TW} \neq 0$) to grounded mode ($\Phi_{TW} = 0$) produces observable changes in the floating potential. As shown on the right in Figure 42, the MINOTOR prototype in floating mode exhibits a floating potential of approximately -20 V, which decreases to -30 V when the thruster is grounded. In floating mode, this results in a potential difference of $\Delta V \approx 60$ V, compared to $\Delta V \approx 30$ V in grounded mode. This explains why MINOTOR's performance is higher in floating mode, as space charge effects contribute positively, enhancing ion acceleration. The purely divergent magnetic field allows electrons to exit the thruster body, pulling ions along with them. Similar behavior is observed for the DEEVAv2 prototype. When operated in grounded mode ($\Phi_{TW} = 0$), the floating potential is about -10 V, yielding a potential difference of $\Delta V \approx 10$ V. In floating mode, the thruster potential increases to 20 V, with a small negative floating potential of around -1 V, resulting in a total potential difference of $\Delta V \approx 21$ V. This indicates that, while the potential gradients are smaller than those for MINOTOR, operating DEEVAv2 in floating mode still results in higher ion energies due to the increased potential difference. For DEEVAv1, the situation is reversed. In floating mode ($\Phi_{TW} \neq 0$), the floating potential is around ± 0.1 V, leading to a potential difference of $\Delta V \approx -10$ V, which decelerates the ions. When switching to grounded mode ($\Phi_{TW} = 0$), the floating potential becomes positive, around 3 V. This indicates that, for DEEVAv1, grounded mode results in less ion deceleration, suggesting that grounded mode operation leads to a higher ion acceleration in case of this thruster.

It is important to note that these observations of the electric potentials and gradients depend on specific operating conditions and are presented here as exemplary cases to demonstrate the underlying correlations.

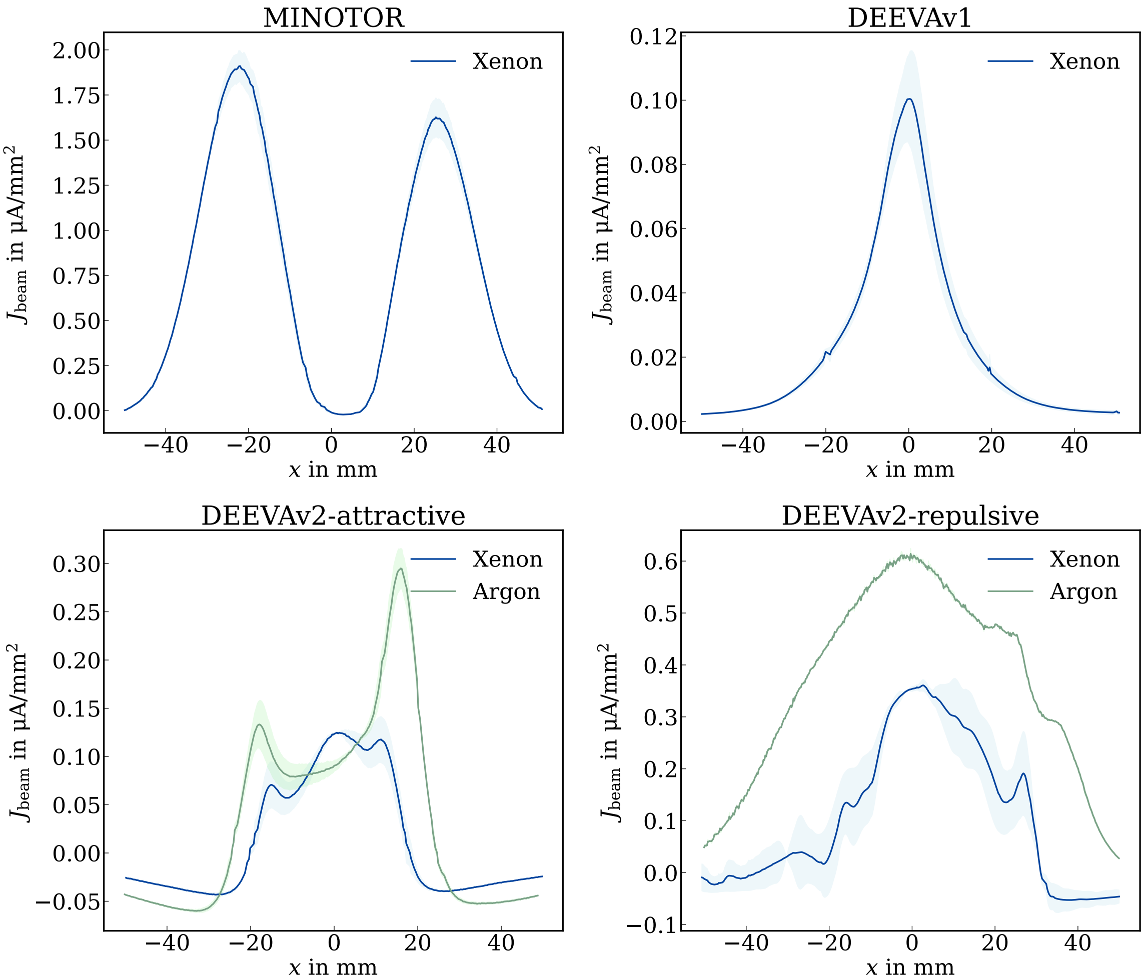

Figure 43: Examples of the current density J_{beam} line scans with a FC along the x-axis at a distance of 10 cm to the thruster exit plane. The MINOTOR and DEEVAv1 prototype were operated with xenon as propellant, the DEEVAv2 configurations were operated with xenon and argon as propellant. All prototypes and configurations were operated at 2.45 GHz, 1 sccm and 30 W microwave power.

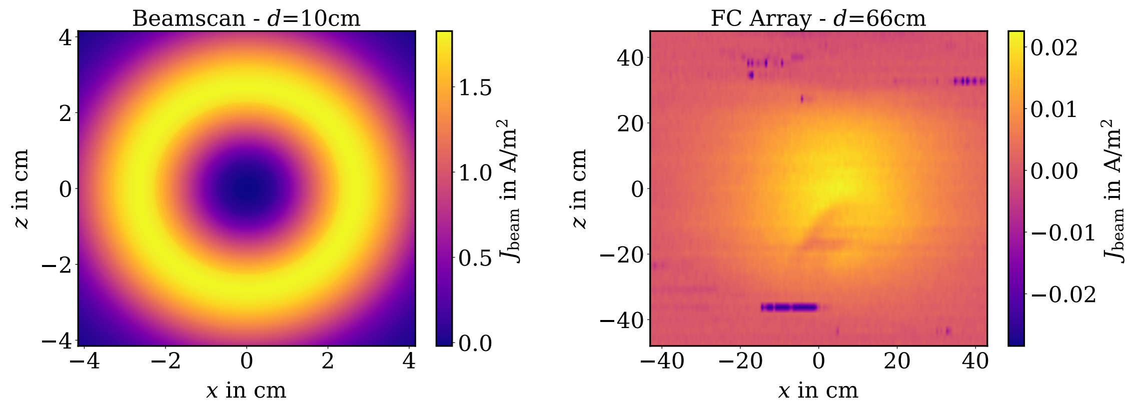

Figure 44: Comparison of the 2D profile of the current density J_{beam} of the MINOTOR prototype, obtained by a linear scan assuming rotational symmetry (left) and a 1D FC array (right). The linear scan was conducted along the x-axis at a distance of 10 cm to the thruster exit plane. The beam profile scan, shown on the right at a distance of 66 cm to the thruster exit plane. The MINOTOR prototype was operated with xenon as propellant, at 2.45 GHz, 1 sccm and 25 W microwave power in both cases. The total beam current determined in case of the beam scan (left) is $I_{\mathrm{beam}} \approx 10.12$ mA. In case of the recording with the FC array (right), the integration over the plane leads to an estimated total ion current of $I_{\mathrm{beam}} \approx 8.9$ mA. In the beam profile recorded with the FC array, one can see around -20< x <0 cm at y=38 cm the holding arm of the Langmuir probe disturbing the current measurement.

3.6. Influences on Ion Current

The total beam ion currents presented in the following are estimates, as they assume rotational symmetry of the ion beam, which is often not the case, see discussion in Chapter 2. For DEEVAv1, we observe a single-peak beam profile in line scans across the beam, as already shown in Chapter 2, while MINOTOR shows an asymmetric beam profile with two maxima, caused by the gas inlet hole positions. DEEVAv2 has an even more asymmetric beam profile with multiple peaks of different heights, caused by uneven distribution of the neutral gas across the diameter of the quartz tube. Examples of such linear beam scans are provided in Figure 43. In the case of DEEVAv2, the ion beam shape and current level also change depending on whether the thruster is operated with argon. The total beam current is determined using Equation 2.45 - in case of MINOTOR is $I_{\mathrm{beam}} \approx 20$ mA. In case of DEEVAv1 it is $I_{\mathrm{beam}} \approx 0.15$ mA, for DEEVAv2 in attractive configuration it is $I_{\mathrm{beam}} \approx 0.5$ mA with xenon and $I_{\mathrm{beam}} \approx 1.5$ mA with argon as propellant. For the DEEVAv2-repulsive configuration it is $I_{\mathrm{beam}} \approx 1$ mA for xenon and $I_{\mathrm{beam}} \approx 4$ mA for argon operation. The operation of the DEEVAv2 prototype with argon in both configurations leads to higher ion currents as well as changes in the beam shape. A high asymmetry can be observed. To confirm the assumption of rotational symmetry, a comparison can be made between total currents postulated from linear beam scans and total current values determined from a FC array. We had the opportunity to carry out such a comparative measurement for the MINOTOR thruster - examples from this measurement campaign are presented in the following - but we did not have access to such an FC array for all measurement campaigns of all the prototypes and therefore cannot yet conclusively clarify the question of the correctness of the rotational symmetry assumption.

Figure 44 depicts a comparison between beam profiles of the current density J_{beam} obtained with a 1D Faraday cup array and a linear scan with a single FC, assuming rotational symmetry of the beam. The linear scans with the single FC was conducted along the x-axis at a distance of 10 cm to the thruster exit plane. The 2D current density plot in case of the linear scan is derived assuming rotational symmetry of the beam. The 1D array with 53 FCs was placed at a distance d=66 cm to the thruster exit plane.

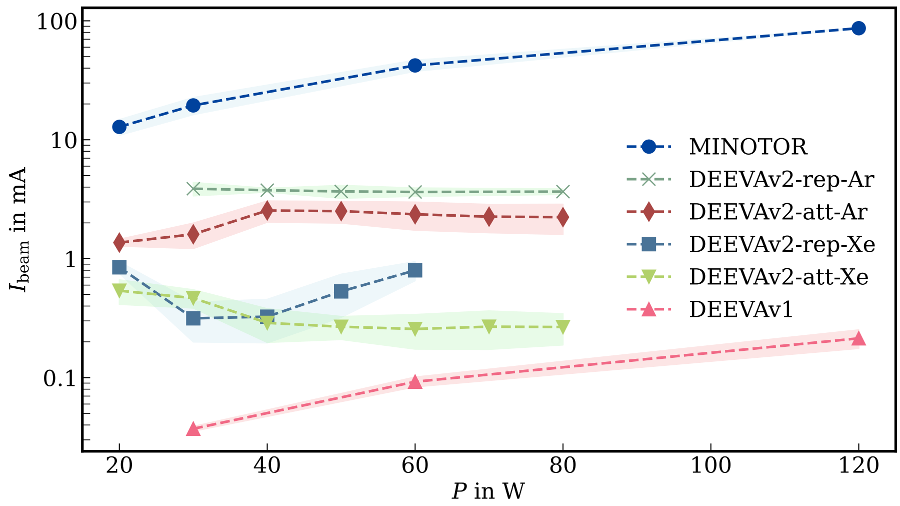

Figure 45: Semilogarithmic plots of the estimated ion current I_{beam} exiting the prototypes for various power settings P. All prototypes were operated at 1 sccm propellant and at a frequency of 2450 MHz. These current estimations are based on the assumption of a rotational symmetry of the beam. The standard deviation from multiple measurements taken, can be seen as underlying shadows of the measurement points.

The total beam current determined in case of the linear scan is $I_{\mathrm{beam}} \approx 10.12\,\mathrm{mA}$. In case of the 1D FC array, the integration over the plane yields an estimated total ion current of $I_{\mathrm{beam}} \approx 8.9\,\mathrm{mA}$. The chosen distances result from practical restraints. As the linear beam scans are performed in the smaller STG-MT chamber and the 1D FC array measurements are performed in the larger JUMBO facility (and the FC array is mounted on a fixed linear stage), the distances are fixed. The different measurement distances of course explain the smaller current density measured in the 1D FC array measurement compared to the linear beam scan with the much closer single FC. The asymmetric shape with two peaks translated in a hollow circle profile in the 2D plot can only be observed at the closer distance.

This means, the estimated total beam current from the scan with the single FC is quite comparable to that determined by the 2D scan, even though we might overestimate the ion current exiting the thruster with the assumption of rotational symmetry in case of the scan with the single FC. This is important to keep in mind for the following discussions.

The estimated ion beam currents from such linear beam scans employing a single FC and assuming rotational symmetry are shown in Figure 45, where we compare current measurements as a function of power for the various thruster prototypes. For MINOTOR, the ion beam currents measured (10 to 100 mA) are consistent with those reported in the literature (see Table 1). DEEVAv1 exhibits the lowest ion beam current, with values up to 0.2 mA only. For DEEVAv2, the repulsive configuration with argon reaches currents in the mA range, up to 4 mA, with no significant power dependence. In contrast, the attractive configuration with argon shows an increase in ion current with increasing microwave power. DEEVAv2 with xenon as propellant produces a low beam current of only 0.4 mA, which interestingly decreases with increasing power. Figure 45 depicts just a subset of the measured data, additional results on frequency and volume flow dependence are included in the Appendix. We also want to highlight the influence of FC orientation relative to the thruster exit plane. When measuring at a distance of approximately 1 m and larger, the thruster can be assumed to be a point plasma source, allowing angle correction based on the probe's setup. In the preliminary Faraday cup array measurements at the JUMBO facility, this correction is applied, and the details can be found in the

Appendix. However, in the smaller STG-MT chamber, where the distance between the thruster's exit plane and the FC is restricted to 10 to 20 cm only, probe orientation may cause an underestimation of the current, particularly at the edges of the scan range where particles may not reach the collector. In a separate campaign, this effect was analyzed by rotating the Faraday cup at different beam positions, and the scans were corrected using the maximum ion current values from these rotations. The procedure is detailed in the Appendix. The corrected current values fell within the error margins of the uncorrected measurements, so no angle correction is applied in this study.

Together with the maximum ion energies shown in Figure 41, we can now estimate the thrust produced by the ions exiting the thruster, using both the ion beam current and ion energy data.

3.7. Magnetic Nozzle Contribution to Measured Thrust

First, we want to emphasize again that the force values below are estimates, as they assume rotational symmetry of the ion beam as well as a beam consisting of single charged ions only. We use the previously determined ion energy of maximum probability to estimate the ions' velocity, and in turn, their force contribution to thrust. This allows us to compare the thrust values from thrust balance measurements (T_{T}) with the force estimates from probes (F_{P}). On the one hand, since we use the ion energy of maximum probability determined and not the whole energy distribution, we very likely overestimate the ion velocity and in turn the force estimated from probe measurements. On the other hand, it is expected that the probe-based force values will underestimate the thrust, as they do not account for the contribution of neutral gas particles. As mentioned in Chapter 2, literature reports a thrust underestimation of about 20% for probe measurements in the case of the MINOTOR prototype [55]. Thus, probe measurements could capture around 80% of the thrust measured by the thrust balance. We, however, observe a factor of 5 difference between the thrust balance values and the probe force values. In other words, the thrust measured by the thrust balance is about five times higher than the force measured by the probes. This corresponds to a 20% contribution to thrust due to MN effects. Determining whether this discrepancy is due to inaccuracies in the thrust balance, the probe estimates, or both, is not straightforward. Knowing the magnetic nozzle effect's contribution to thrust in the MINOTOR case, we can carefully compare the discrepancies between probe and thrust balance measurements for the other prototypes and try to correlate it with the MN effects. Figure 46 shows the comparison for all prototypes operated with xenon. The MINOTOR results are closer to the expected factor of 5 difference, indicating that about 20% of the thrust can be attributed to magnetic nozzle effects (excluding charge exchange effects). Both T_{T} and F_{P} increase with input power, showing consistent trends. However, for the DEEVAv2-attractive and DEEVAv1 prototypes operated with xenon, we see a much larger discrepancy, with thrust balance values being roughly 100 times higher than probe values. DEEVAv2 shows higher thrust and probe values than DEEVAv1. This suggests that magnetic nozzle effects are not the main contributors to the thrust in these cases, and neutral gas must play a significant role. In the case of DEEVAv1, the assumption that cold gas is the primary source of thrust, which has been proposed earlier, is confirmed. For DEEVAv2-attractive with xenon, an explanation, for this large difference between the thrust balance determined thrust and the force value determined with probes, is not immediately available, but this observation is discussed in the next section.

When the DEEVAv2 thruster is operated with argon, the situation changes significantly. In Figure 47, we see the comparison of T_{T} and F_{P} for MINOTOR as well as the DEEVAv2 prototype in both attractive and repulsive configuration operated with argon. The DEEVAv2-attractive configuration shows slightly higher thrust values than DEEVAv2-repulsive, though the difference is not substantial. However, it is clear that the contribution of magnetic nozzle effects to the measured thrust is much lower in the attractive configuration compared to the repulsive configuration. This aligns with the ion current and maximum ion energy data, which suggest better performance in the repulsive configuration, indicating more effective use of MN effects. It remains unclear why the thrust balance shows slightly higher values for the attractive configuration. At higher power settings, the repulsive configuration yields higher thrust than the attractive one. A comparison at higher power levels is provided in the Appendix. Additionally, for other operational variations, such as frequency, similar

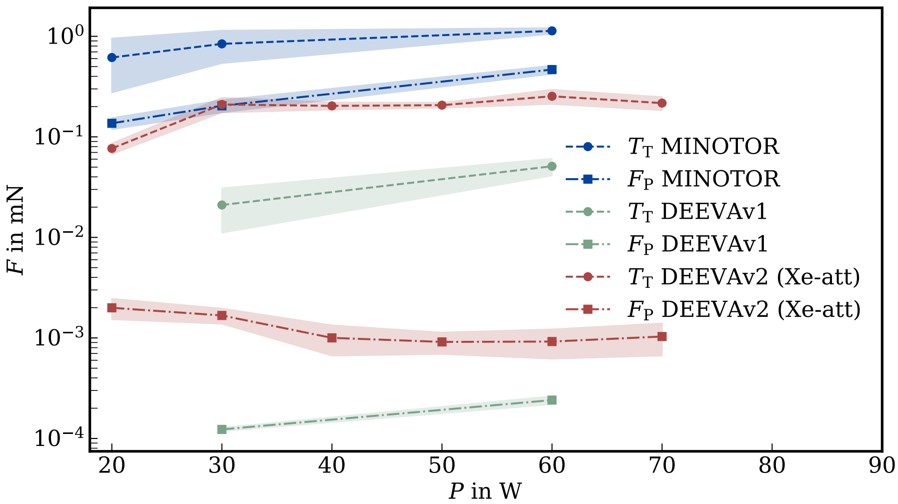

Figure 46: Comparison between thrust F measured with the thrust balance T_{T} and estimated thrust by probe measurements F_{P}. Prototypes under investigation are the MINOTOR, DEEVAv1 and the DEEVAv2 (att-Xe). All thruster prototypes were operated at 2450 MHz and 1 sccm xenon for varying input power P.

thrust values are observed for both configurations. These trends and operational variations are also detailed in the Appendix. While these observations are interesting, they are not directly relevant to the main question of how significant MN effects are in contributing to thrust. Therefore, we focus here on that question and refer to the Appendix for further details. What we can already see is that the correlation factor between the measured and calculated thrust for DEEVAv1 is about 100 or more, while for MINOTOR it is around 2 to 5. For the DEEVAv2-repulsive configuration with argon, we also reach factors of about 2 to 5, though with lower overall thrust values.

A clear overview of the contribution of MN effects to the produced thrust is shown in Figure 48. This completes the explanation of why the MINOTOR prototype achieves the highest thrust compared to the DEEVA thruster development stages. Starting with the magnetic field topology of MINOTOR, which fulfills the ECR condition and exhibits a strictly diverging magnetic field, we observe a contribution of MN effects to the measured thrust of 20 to 50%, corresponding to a $T_{\mathrm{T}}/F_{\mathrm{P}}$ ratio of about 2 to 5. For the first DEEVA prototype, DEEVAv1, which does not sufficiently fulfill the ECR condition and includes a strongly converging magnetic field, the measured thrust mainly comes from the cold gas inlet. This is evident from the large ratio of about 200 between the thrust balance measurement and the probe-estimated thrust. The second development stage, DEEVAv2-attractive configuration, shows better ECR conditions and less converging magnetic field lines. However, with xenon as a propellant, the ratio worsens to almost 300, indicating a large contribution of neutral gas to the thrust. Thrust values approach 1 mN, while the probe-estimated thrust remains in the 1 µN range. The situation changes significantly when operating the same DEEVAv2-attractive configuration with argon, where the ratio improves to about 10. Even more notable is the improvement when switching to the DEEVAv2-repulsive configuration. Here, the ECR condition is also fully met, the small converging part of the MN is avoided, and a steeper magnetic field gradient yields higher electron temperatures, leading to higher ion energies and greater particle extraction. In this configuration, the ratio of force determined by thrust balance to probe results improves to about 2 to 5, similar to the MINOTOR prototype.

The MINOTOR prototype continues to show slightly higher thrust values, particularly in the power ranges discussed. However, the developmental stages of the DEEVA concept and the demonstrated effects highlight which adaptations lead to performance changes in the DEEVA prototype versions.

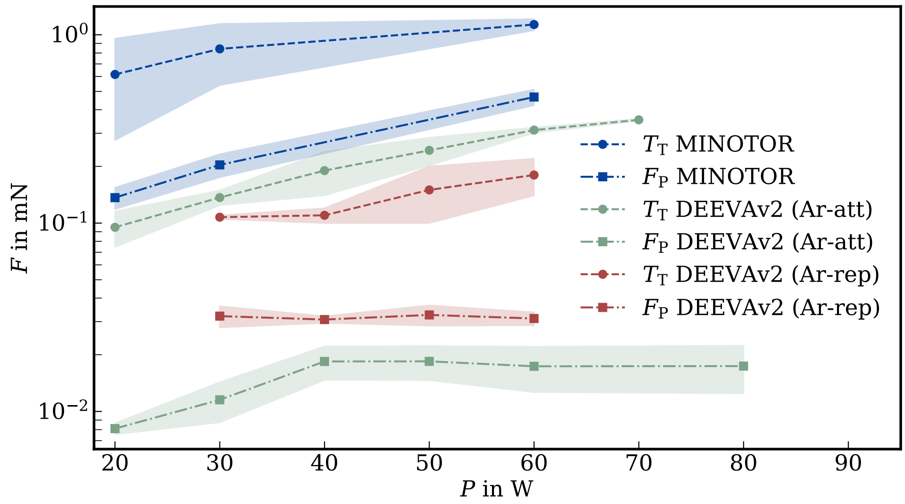

Figure 47: Comparison between measured thrust with the thrust balance T_T and determined thrust by probe measurements F_P. Prototypes under investigation are the MINOTOR and the DEEVAv2 in attractive and repulsive configuration. All thruster prototypes were operated at 2450 MHz and 1 sccm for varying input power P. MINOTOR was operated with xenon as propellant, DEEVAv2 was operated with argon.

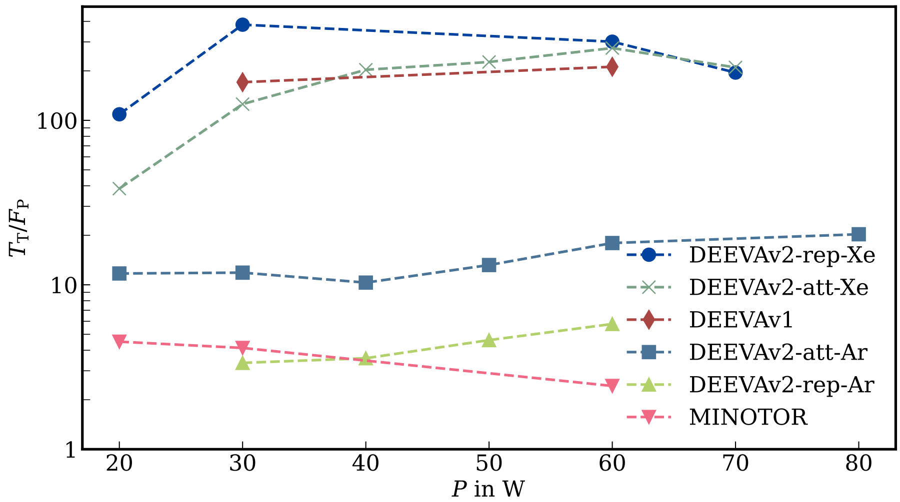

Figure 48: Ratio between thrust measured with the thrust balance T_T and determined by probe measurements F_P for all prototypes as a function of input power P. All thruster prototypes were operated at 2450 MHz and 1 sccm. MINOTOR and DEEVAv1 were operated with xenon as propellant, DEEVAv2 was operated either with xenon or argon.

This clarity points to the necessary improvements for the DEEVA prototype, which will be discussed in the next section. The results presented here illustrate the progress made at each development stage and how plasma and thrust parameters can be effectively adjusted and interpreted.

4. Discussion

In this chapter we want to briefly summarize the results and observations that are made in this work. We capture the main findings and compare the observations made with literature results and models. For this purpose, we discuss the magnetic field topologies of the DEEVA prototypes in comparison to the reference thruster, the MINOTOR prototype. We continue discussing the influence of microwave coupling on thrust and plasma parameters, like the ion energy and ion beam current. We furthermore state the main limitations that have been identified in the course of this work. We then discuss the main open question coming forward based on the results obtained. This covers the performance of the different propellants as well as a possible explanation for the fraction of the measured thrust which is not due to the MN contributions. We propose first steps to tackle the posed open questions, covering necessary adaptions on existing measurement methods as well as necessary supplementary measurements to further confirm the findings made in our investigations. We also give some ideas about next new experiments to close knowledge gaps. As this study presents development stages of the DEEVA prototype, further improvements based on these investigations are proposed, covering magnetic field topology improvements as well as antenna adaptions. Of course this is to be understood as an outlook, and needs to be realized and tested before confirmation can be given. We then conclude this work with the recapitulation of the posed research questions and the answers delivered during the course of this work.

4.1. Summary of Results and Observations

4.1.1. Summary

During the course of this work the central question of this study was: What influence does the electrodeless microwave coupling, in conjunction with the magnetic field topology, as realized in the DEEVA prototypes, exerts on plasma parameters, and ultimately on thrust in comparison to the MINOTOR prototype? To adress this question we firstly assess the thrust parameters of the development stages of the DEEVA prototype (DEEVAv1, DEEVAv2-att, and DEEVAv2-rep) as well as the MINOTOR prototype.

The results show that the thrust in case of MINOTOR is the highest in the low to mid power range of 20 to 80 W. Furthermore we can deduce that the thrust production in case of DEEVAv1 can be attributed to the neutral gas injection. This is consistent with the observation that there is no plasma beam ejected from the DEEVAv1 prototype, as shown in the beam photographs. We see that with an increase in input power in case of the DEEVAv2 prototypes we reach thrust values comparable or even higher than for MINOTOR. Such high powers (above 60 W) are not feasible for the MINOTOR prototype in use, as its inner conductor starts to glow and sputter and is eroded during those prolonged high power measurements. However, what is extremely important to note, is that the coupling via a waveguide leads to higher power losses, that were already observed with the MINOTOR prototypes [23]. This explains why we need higher input powers in case of the DEEVA prototypes to reach thrust and plasma parameter values comparable to the MINOTOR prototype. Nevertheless, the behavior of power coupling seems to be almost comparable for both, the MINOTOR and the DEEVA prototypes. Namely, an increase in input power leads to higher plasma densities, higher electron temperatures, higher ion energies, thrust, etc. Therefore, the concept of converting the energy coupled into the plasma by heating and stored in the electron motion (i.e. the electron temperature) into ion energy and thus into thrust seems to be comparable for both prototypes.

As we can already see in DEEVAv1 case, the DEEVA prototypes are less sensitive to a variation of the excitation frequency than MINOTOR. Due to DEEVA's waveguide like microwave coupling, certain frequencies are more efficiently coupled into the plasma than others. Nevertheless, an ignition and operation is still possible for a broader bandwidth of frequencies with the DEEVA prototype in comparison to the MINOTOR prototype. Furthermore frequency variation does not show a significant influence on thrust or plasma parameters (like electron temperature, ion energy, etc.), while it seems that MINOTOR exhibits an optimum performance at the design frequency of 2450 MHz.

Another aspect explored is the dependence of performance on the choice of propellant. In particular we focused on the operation of the DEEVAv2 prototype with argon as propellant. What was observed repeatably is that the operation with argon delivered better performance levels for the same power settings, resulting not just in higher thrust values but also in plasma parameter values. We observe higher ion energies, electron temperatures, and ion currents when DEEVAv2 in both configurations is operated with argon. Furthermore we detect high thrust values for the operation of the DEEVAv2-repulsive configuration with argon. We found the highest thrust efficiency for MINOTOR of about 11 % followed by the DEEVAv2-repulsive configuration of about 4 %.

The central question can therefore be refined to why is the thrust in case of MINOTOR the highest in the low to mid power range? In order to answer this question, the various contributions to the thrust have to be investigated - this includes the magnetic field topology.

The magnetic field topology exhibits a strictly diverging character in case of the MINOTOR prototype, a converging-diverging character in case of DEEVAv1, a divergent-convergent-divergent character in case of DEEVAv2-att, and a divergent-parallel-divergent character of the DEEVAv2-rep prototype.

We see the ECR condition fulfilled in case of MINOTOR. However, since it is not known which type of magnet topology is used at the available prototype a comparison of the magnetic field topology to literature values is not as easy, as different magnet configurations lead to different topologies. This is investigated and described in Refs. 23 and 61. A decrease in magnetic flux density is observed after many hours of operation of the MINOTOR prototype, which can be attributed to heating up of the thruster as well as possible physical shocks due to handling of the magnets. The strictly diverging character of the MINOTOR prototype leads to an immediate acceleration of the electrons, therefore a positive thruster potential and a negative floating potential in 10 cm distance to the thruster exit can be measured, further accelerating the ions.

The situation is entirely different for the DEEVAv1 prototype; First of all the ECR condition is not fulfilled over the whole diameter of the discharge chamber, if fulfilled at all. This leads to a less efficient plasma production, especially in comparison to the MINOTOR prototype. The ignition and operation of this prototype is not as easy and steady as for the other DEEVA prototypes. Furthermore it is found that the shape of the magnetic field in case of the DEEVAv1 prototype (converging-diverging) leads to hardly any extraction of the electrons, either not produced in the first place, or not extracted due to the magnetic field gradients leading to mirror effects, reflecting the electrons back into the plasma instead of accelerating them out of the thruster. Thus the electrons can also be trapped by the cusp field of the ring magnet, which explains the negative thruster potential building up in DEEVAv1 case.

By adapting the DEEVA prototype and placing a stronger magnet in the back of the thruster, the ECR condition is now fulfilled over a larger region, i.e. over the entire diameter of the quartz glas tube, and also allows for a higher frequency bandwidth, as the ECR zone can now easily shift along the centerline of the thruster. The better plasma production in DEEVAv2 case is manifested by an easier ignition process, without the need for a gas shock or very high powers, and by the possibility to also operate with argon as propellant. As the electron temperature is not influenced directly by the magnetic nozzle but by the ignition and the plasma potential, its higher value in case of the DEEVAv2 prototype further confirms a better plasma production. What is safe to say is that the combination of the ECR condition fulfilled and the plasma extraction with the magnetic field topology of the DEEVAv2 prototype, leads to higher ion beam current and higher electron temperatures in the beam when operated with argon.

One challenge which is inherent for the SLAN/DEEVA configuration, is that the antenna and thus the discharge region is longer than the discharge chamber of the MINOTOR prototype. Therefore the gradient of the magnetic field produced by the magnets which are responsible for meeting the ECR condition, cannot just simply be used to accelerate the plasma by its own, since the magnetic field lines would mostly cross the glass chamber walls. A consequence are immense wall losses. Therefore, the magnetic field lines have to be stretched in a way to confine the plasma (and keep it away from the walls) and to accelerate it just at the thruster exit, i.e. show a high negative gradient outside the thruster exit only. To realize such a topology is quite challenging but can be realized by a ring magnet of a smaller magnetization downstream at the thruster exit. The first configuration where the magnetization's of the magnets point in the same direction leads to a diverging-converging-diverging character of the magnetic field topology. In this case, we observe a strong gradient in magnetic flux density, however near the thruster exit plane, where the actual acceleration and expansion of the plasma should happen, we see converging magnetic field lines. This leads to similar effects as for the DEEVAv1 prototype, where part of the plasma cannot leave the thruster or is decelerated. Furthermore the diverging part outside of the thruster, now shows just a very small gradient, leading to an insufficient acceleration for this prototype. To circumvent the converging part, in the DEEVAv2-rep configuration the magnetization's of the magnets are oriented antiparallel. We believe that this compromise ensures a sufficient level of confinement of the plasma, without the converging part, possibly decelerating the plasma particles at the thruster exit that should be accelerated at this point.

In Refs. 79 and 80 the effects of plasma confinement on plasma momentum are investigated, showing that a critical magnetic flux density for efficient plasma confinement in helicon plasma thrusters exist and demonstrating that the radial momentum flux to the plasma source wall is significantly reduced by increasing the magnetic flux density. Therefore, to better confine our plasma and reduce radial momentum flux we could increase the magnetic flux density, i.e. use stronger magnets. However, for both DEEVAv2 configurations a cusp field around the front ring magnet still forms, leading to a thruster potential which is not as high as in MINOTOR case. The thruster potential of the DEEVAv2 prototype is positive and within the beam a negative floating potential can be observed.

As it is reported Ref. 23 the thruster potential has an impact on the performance of the prototype. As the thruster potential depends on the electron temperature in the source and is directly proportional to the mean ion energy, it is reported that a factor of 1.4 is found between the thruster potential and the ion energy (e.g. a thruster potential of 100 V would correspond to an ion energy of 140 eV) [23, 55, 56]. We could not confirm this ratio, as the approximate ratio between ion energy and thruster potential lies in our case at 3.9. This higher ratio between thruster potential and ion energy probably results from the higher background pressure in our measurements. A higher background pressure leads to a decrease of thruster potential [23]. If the ratio of thruster potential and ion energy really changes with increasing background pressure, is still open for discussion and needs to be investigated further. Also for the DEEVAv2 prototype an influence on the performance can be seen if one allows the thruster to charge up. The impact of the space charge effects on thruster performance needs further investigation, as it was repeatably observed, that when changing the thruster from floating to grounded mode the floating potential in the beam is affected and other way around. If these differences in space charge effects affect ion energy and thrust, still needs to be investigated. However, at this point, we already can correlate the highest thrust to the highest gradient in magnetic flux density. Based on this observation, the MINOTOR prototype should have the highest and the DEEVAv2-rep the second highest thrust. This is confirmed by direct thrust measurements as well as thrust estimated on the basis of probe measurements.

We further can state that the highest gradient in magnetic field (again MINOTOR) leads to the highest ion energy. This is not very surprising as the gradient in magnetic field is proportional to the particle acceleration as shown in Equation 2.38 and Refs. 3, 23 and 60. We see bi-Maxwellian characters of the IEDF in case of the MINOTOR prototype and Maxwellian shaped ion energy distributions for the DEEVA prototypes. For the DEEVAv2 operation with xenon similar ion energies with maximum probability are determined as for the DEEVAv1 prototype. Surprisingly the operation with argon leads to significantly higher ion energies in both DEEVAv2 configurations. The same observations hold true with respect to the EEDFs. Comparison of RPA and LP measurements in different test facilities using different probes deliver reasonably similar results of the ion energy and electron temperature. In closer vicinity to the thruster bi-Maxwellian shaped EEDFs are determined in case of the MINOTOR prototype. However, the orientation of the LP in close vicinity of the thruster exit plane with respect to the magnetic field topology plays a role, in such a way that the measured EEDF show a highly anisotropic, non-Maxwellian character. We observe for several operating points of the thruster that the determined EEDF in parallel orientation shows a stronger non-Maxwellian character than in orthogonal orientation. The resulting differences between plasma parameters obtained for the two different orientations are therefore explained. It is not possible to state, that the orientation of the probe with respect to the magnetic field lines does not play a role in ECRT with MN, even if the Larmor radius and probe size should assure that according to Lobbia *et al.* [68]. We determine a Larmor radius of about $4 \cdot 10^{-3}$ m vs a probe radius of $0.5 \cdot 10^{-3}$ m. The differences in the determined electron temperatures and densities lie, however, within typical theoretical probe accuracies, in the order of around 50% [68]. Overall we determine in every parallel orientation a non-Maxwellian, at least bi-energy distribution. Apparently anisotropy leads to just detecting the non-Maxwellian distribution with the probe orientated parallel to the magnetic field lines. If the acceleration process is explained by the ambipolar process, the energy distributions of electrons and ions are connected. If that is the case, information gets lost if in the EEDF just one energy species is detected while for the ions two energy species are determined. We therefore state, that due to the non-Maxwellian distribution mainly visible in parallel orientation, a parallel orientation of Langmuir probes with respect to magnetic field lines is preferable for ECRT with MN. However, to mitigate the relevance of the orientation of the probe, the probe location for the measurements is set further away from the thruster exit to a minimum distance of 10 cm. The finding of bi-Maxwellian distributions (EEDF and IEDF) is also reported in literature, and can be explained by the ignition and the heating of the plasma itself. The microwave is absorbed in a polarized way, leading to a different electron energy gain parallel and orthogonal to the magnetic field lines. As it can be assumed that the electron dynamics influence the ion dynamics as well, a bi-Maxwellian character of the EEDF could be the reason for the bi-Maxwellian character of the IEDF. The reason for the prominence of a bi-Maxwellian shape in case of MINOTOR could again be an indication that the absorption of the microwave in case of the SLAN coupling is more complex, as there is not just the R wave to be expected to lead to a heating of the plasma but also the X-wave (compare Chapter 2). A plasma model would be necessary for the SLAN plasma to confirm this hypothesis.

As for the correlation between the electron temperature and the ion energy, we see a clear correlation between ion energy and electron temperature for all the prototypes, characteristics indicative of a MN. We note a similar constant ratio in the case of the MINOTOR prototype, albeit with a ratio more than twice as high as previously reported values. This discrepancy can be attributed to higher electron temperatures reported in the literature, where measurements exceeding 20 eV were recorded alongside similar or even smaller ion energies than in our case [56]. Understanding the variance between the results of the ECR thruster prototype in literature and our observations is challenging. Factors such as the thruster set up (including magnetic field topology, microwave generator, cabling, and mass flow control unit), LP position, data acquisition and evaluation methods, ion energy detection method, and facility effects (e.g. chamber size, pumping rates, etc.); all play significant roles in determining plasma parameters and performance. This motivated our analysis on comparing the MINOTOR and DEEVA prototypes, both examined under identical conditions in the same vacuum chamber, with consistent background pressures, thruster set ups, and diagnostic tools and methods. Our findings reveal a relatively constant ratio of electron temperature to ion energy in the MINOTOR case, suggesting that expansion is predominantly driven by electron dynamics, with higher electron temperatures resulting in higher ion energies. However, taking the MINOTOR results measured by us as a reference and comparing the DEEVA prototypes with this ratio, we reach similar ratios with the DEEVAv2-rep prototype.

Based on ion velocity and ion current we can infer the contribution to thrust of the ions leaving the thruster. We see a smaller contribution to thrust detected by the probes in case of MINOTOR than reported in literature [55]. We see a contribution to up to 50% of the ions to the total thrust while 80% are reported in Ref. 55. However, if we compare the results of the development stages of the DEEVA prototype to those of the MINOTOR prototype operated with xenon under identical test conditions, we reach similar ion contributions to total thrust in case of DEEVAv2-rep operated with argon. Even though the absolute thrust values of the DEEVA prototype lie below the MINOTOR prototype in the chosen power range, for higher power settings of DEEVAv2 we reach the same thrust values.

In summary, the magnetic field topology and the coupling method in case of MINOTOR leads to an efficient plasma production and immediate plasma acceleration, yielding thrust supporting space charge effects and therefore thrusts in the mN range where the thrust contribution of ion currents can be detected and associated to be 50% of the produced total thrust. For the DEEVA prototypes it can be concluded that the magnetic field topology needs to be more complicated in order to reach similar performance values. This is due to the SLAN antenna design which causes an extended discharge region. This extended discharge region leads to increased requirements for plasma confinement and the location of acceleration. As a consequence of the SLAN microwave coupling, the DEEVA design needs higher levels of power for comparable operational performance. Nevertheless, we also reach a contribution of the ion current to the total thrust of about 50% for the latest development stage, the DEEVAv2-rep operated with argon.

4.1.2. Critical Points

First of all we want to summarize the assumptions made in this study, which have to be taken into account in the discussion. We will also give motivation for future measurement improvements.

For all our measurements we use invasive diagnostic methods. It is well known that the insertion of a LP or the positioning of a RPA in the thruster plume may change the plasma parameter and the discharge significantly. Non invasive methods, like laser induced fluorescence (LIF), Thomson scattering and optical emission spectroscopy (OES) would be of immense interest, to compare the values determined in this study with those determined by non invasive methods. Of course a plasma model for quantitative OES evaluation is necessary, which again must be based on plasma properties which have to be known. These either have to be simulated by first-principle calculations or be measured by invasive methods. As for the LIF method, if a two-photon set up is used also the doubly charged ions could be detected, which are not taken account in our investigations and analysis at the moment.

When characterizing thruster operation we always give the power output of the microwave generator. It is known that the standing wave ratio of the signal changes depending on plasma properties, antenna placement and configuration. Preliminary studies regarding reflected power were conducted. However, these effects are not taken into account during this study as the directional coupler for this kind of measurement was not always available. We therefore rely on the power measurement of the generator itself, which has an error margin of 5 W. For future experiments such a directional coupler could be very useful to actually determine what power is actually coupled into the plasma. The same holds for verification of the set frequency. Although we frequently checked the microwave signal of the generator with a spectrum analyzer, a permanent measurement of the excitation frequency would eliminate questions regarding frequency shifts when the plasma ignites. Another factor relevant for the actual coupling of power into the plasma is the heating up of the thruster. At least for the DEEVA thruster it is known that with an increase in temperature the best suited frequency for operation changes as the electromagnetic characteristics of the SLAN change with increasing temperature. To fully assess this performance dependence more temperature sensors should be placed on the structure of the antenna, or an infrared camera should be used to analyze the heating up of the DEEVA prototype. The heating up process is of course also relevant for the MINOTOR prototype. Furthermore, after extended time of operation and heating up of the prototypes the magnets degrade. This occurs for the MINOTOR as well as for the DEEVA prototypes. Therefore, a certain degree of insecurity comes into play regarding the present magnetic field topology, even though we try to mitigate this, by frequently mapping the magnetic field topology. The same holds for the microwave cabling. With heating up and length of the cables noticeable changes in performance can be observed. These should also be characterized in more detail by using a direction coupler at a suitable position, or calibrating the power line during operation.

As for the thruster characteristics, here we need to mention changes of the MINOTOR prototype after longer operational times. As we see (especially for higher power levels) sputtering of the inner conductor occurs as well as deposition of ablated stainless steel at the boron nitride backplate. If this layer of metal is not removed frequently, it can lead to a failure of the thruster. How this ablation over time changes the electromagnetic behavior of the MINOTOR prototype remains an open question. As for the DEEVA prototypes; their modular design causes weaknesses, as slight changes, e.g. tightness of screws, can lead to the in-operability of the thruster. A more consolidated design, with less possibilities for changes is therefore desirable as a next step. Motivation for the current set up was the development character of the prototype. Therefore, it was easy to change components like magnets, quartzglas tube, etc.. As we now reach the requirements of the DEEP project with the DEEVA prototype a more consolidated version is essential.

Also of importance is the reliability of the diagnostic tools and the analysis. The probes are exposed to plasma and can also heat up or get sputtered. Especially the thrust balance shows high thermal drifts. Also the influence on the probes from their surroundings - the magnetic field, as well as the microwave signals - may not be known in detail. Already investigated is the influence of the magnetic field on Langmuir probe measurements. Although steps are initiated to circumvent influences, like the usage of low pass filters in the current measurements and a minimum distance of the probe to the thruster exit plane, some limitations of the probe measurements remain unclear. For example in case of the FC and RPA measurements, particles that enter the cups may be trapped and change the pressure within the probe, which can lead to erroneous current measurement data due to an altered potential profile within the gridded analyzer.

Furthermore the assumptions in the force estimation; we just take singly charged particles into account and we assume that all ions possess the same energy, that of maximum probability. Therefore we do not take the velocity distribution into account in the thrust determination. As a consequence we neglect the changes of ion energy depending on the position within the beam. Even though beam scans with the RPA were undertaken and do not show a significant decrease of ion energy towards the edges of the beam, it would be more accurate to take the spatial velocity distribution of the beam into account. Additionally we assume rotational symmetry for the ion current measurements. A 1D FC array measurements which can be moved in front of the thruster exit plane, as it is established in the JUMBO facility should be used in future experiments in order to avoid the necessity of assuming a rotational symmetry about the plume axis in the determination of the total ion current. By scanning with such a 1D FC array in the beam plane, the assumption of the rotational symmetry could be confirmed, or rejected.

This leads us to one of the most crucial open points. We estimated a thrust contribution of the ion current of up to 50%. The remainder of the thrust must come from neutral gas. Neutral gas can be the cold gas from the gas inlet as in the DEEVAv1 case. However this force contribution was tested and calculated to be around 0.02 mN at our volume flows [81]. Therefore, this value is not sufficient to explain the higher thrust levels of about 0.2 mN in case of the DEEVAv2 prototype. The second possibility is hotter gas, heated by the plasma or the antenna structure and exiting the thruster body. However, since we assume a rarefied gas system and do not have a classical nozzle design (like a naval nozzle), to produce a thrust in this magnitude would require a temperature above the melting temperature of quartzglas, and seems unlikely. Simulations could be useful, which aim to answer the question how hot the gas must be to produce that amount of thrust. A third possibility is that the neutral gas is composed of fast neutrals which originate from charge exchange processes between high energy ions and neutrals. Such charge exchange processes are assumed to take place in MNs and high energy plasma sources [50]. To assess if the plasma conditions are met for charge exchange processes within the DEEVA thruster two approaches are possible. First, a thruster model needs to be set up and a simulation including the microwave coupling and the magnetized plasma behavior be conducted. The development of such a model even on a low level would be very useful, also in adapting the magnetic nozzle design. However, to access the plasma parameter inside the thruster structure a probe insertion could be the easier way. This second approach requires that the influence of the invasive probes is taken into account. The three neutral gas contributions proposed here are only partly investigated to date. In a finer step it has to be verified that the other 50% of the thrust are really contributed by neutral gas. This can be done by measuring with a neutral gas probe, like a Patterson probe. If it shows that the produced thrust cannot be explained by the neutral gas, the only explanation left is a malfunction of the thrust balance. However, as the balance is tested with a cold gas thruster with a known thrust (see Ref. 76) and shows similar values as reported in literature in case of MINOTOR (see Ref. 55 and 23), a malfunction seems unlikely. However, a validation of the thrust balance measurements, with for example thrust pendulum measurements, could be advantageous.

We have to state, that the conversion of the electrons movement into the ion kinetic energy happens in close vicinity to the thruster exit plane. Since we are measuring at a distance of 10 cm the electrons may have cooled down already at the measurement position. The chosen position for the Langmuir probe is primarily determined by practical constraints. Indeed, it would be ideal to measure plasma parameters closer to - or even inside - the source. However, several factors limit our ability to do so. First, the DEEVA thruster has geometric restrictions that prevent probe insertion into the discharge vessel, in contrast to the MINOTOR prototype, which has a more accessible structure. Invasive measurement methods, like the Langmuir probe, also tend to disturb plasma parameters near the thruster's exit plane. While electron temperature and plasma potential near the source are, of course, crucial for ion acceleration, our study focuses on comparing the ratios of plasma parameters between two prototypes using the same measurement methods and detector positions for both thrusters. A detailed spatial mapping of plasma parameters within the source and the plume (e.g. with a LP) is crucial in understanding the processes within or near the magnetic nozzle and the plasma source. These measurements are planned in future experiments.

Finally we will discuss the differences in thruster performance using xenon or argon as propellant. Different possibilities are suggested to explain the better performance for argon. At first sight, though, this finding seems counterintuitive. Argon is lighter than xenon, therefore the same velocity of the ion leads to a smaller thrust. Furthermore, it is harder to ionize, see Chapter 2. However in all plasma parameters besides the thrust, argon outperforms xenon in case of the DEEVAv2 prototype. In case of MINOTOR an investigation with argon was reported in Ref. 63, however at higher volume flows. Unfortunately in our investigations the MINOTOR prototype could not be operated at stable conditions with argon therefore a comparison of operation with argon and xenon was not possible with this prototype. DEEVAv2, however, operates even better with argon. One possible reason could be the confinement condition. As xenon is heavier, it could be that stronger magnetic fields are necessary to keep the plasma away from the walls and reduce the wall losses. Furthermore the difference in ionization energy could lead to a difference in electron temperature. At least for DEEVAv2-att case, this difference in electron temperature could lead to a reflection of the electrons at the converging part of the magnetic field topology that they cannot leave the thruster body. Of course this statement should lead to a comparable performance of argon and xenon in DEEVAv2-rep configuration, which is not the case. Additional investigations with krypton as propellant lead to performances between those of the other two gases (xenon and argon), supporting the assumption that the differences in performance originate from the differences in mass and ionization energy. However, since the krypton results are closer to those of xenon than to argon, despite the fact the the ionization energy and mass of krypton is more similar to argon than it is to xenon, the question of why the performances differ so much is still unanswered. The electron temperature is crucial for the ion acceleration. If (in dependence on the ionization energy) the electron temperature inside the plasma source changes, its effect should be visible in the plume. As a result in case of xenon we would expect a lower electron temperature, and a lower plasma potential inside the source. These assumptions need to be checked with a simulation and with a LP inserted into the discharge chamber. Furthermore the hypothesis of wall losses could be investigated with such a probe to map the plasma properties over the whole length and diameter of the discharge chamber. Additionally in the area outside of the thruster such a mapping would be interesting, as the correlation between electron temperature and ion energy established in this study was recorded at one position inside the beam only.

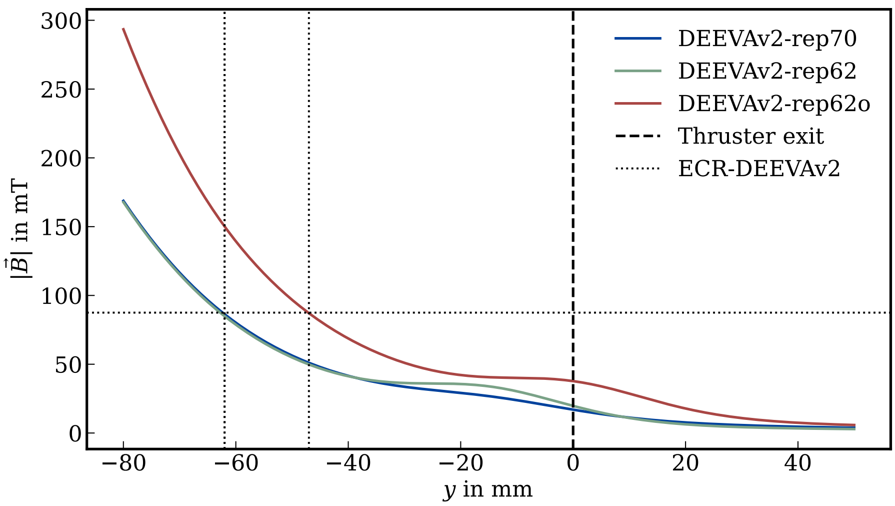

Figure 49: Calculated magnetic flux density along the centerline of three different DEEVAv2 configurations. DEEVAv2-rep70 corresponds to the presented version of the DEEVAv2 prototype. DEEVAv2-rep62 shows the simulated results for the current configuration (distance between disc magnets and ring magnet is 110 mm), but with a smaller inner diameter of 62 mm of the ring magnet, and kept magnetization of the magnets. DEEVAv2-rep62o refers to the optimized DEEVAv2 configuration of repelling magnets, with an inner diameter of 62 mm of the ring magnet which is placed 5 mm closer to the disc magnets. In this configuration the disc magnets are simulated to be magnetized up to 2.5 T. The ECR zones are indicated by the dotted lines. Since the magnetic flux density in case of DEEVAv2-rep62o is larger, its ECR zone lies closer to the thruster exit. Furthermore the gradient after the thruster exit plane outside of the thruster is higher than for any other DEEVAv2 configuration.

4.2. Outlook

It was shown during this study that the conducted adaptions of the prototypes lead to the desired performance improvements. The focus was on the characterization and optimization of the magnetic field topology. Still, the thrust and performance of the DEEVA prototype can be further improved. Besides the next step turning the modular built prototype into a more consolidated version, further adaptions regarding magnetic field topology are currently undertaken.

First of all the diameter of the ring magnet can be adapted to a diameter of 62 mm instead of the 70 mm currently in use. This already leads to a steeper gradient in magnetic field at the thruster exit, as it can be seen in Figure 49. In The corresponding curves are simulated data using the magpylib package in python. We compare results of the DEEVAv2-rep version discussed in this work (DEEVAv2-rep70) and the adapted version of a smaller inner diameter of the ring magnet of 62 mm (DEEVAv2-rep62). For these two configurations the ECR condition is still met at the same position. One of the conclusions drawn from the presented research is that wall losses inside the quartz glass tube are larger than for MINOTOR due to the length of the discharge chamber. Bringing the ECR condition closer to the thruster exit should therefore reduce such losses, since a stronger magnetic field will lead to a better plasma confinement. This would include possible improvements in operating the DEEVAv2 prototype with xenon. Bringing the ECR zone closer to the thruster exit can be achieved by using a stronger magnet at the back, and/or by shortening the antenna. Here we reach some limitations due to the waveguide character of the antenna. As it can be seen in Figure 50, a change in length leads to a shift in frequency of the antenna. The scattering parameter S_{11}, calculated here using COMSOL, describes the electrical behavior of linear networks under steady-state electrical signals. This parameter is exemplified for various SLAN lengths at constant radii and launcher position. A frequency shift is observed when the waveguide is shortened by two centimeters; specifically,

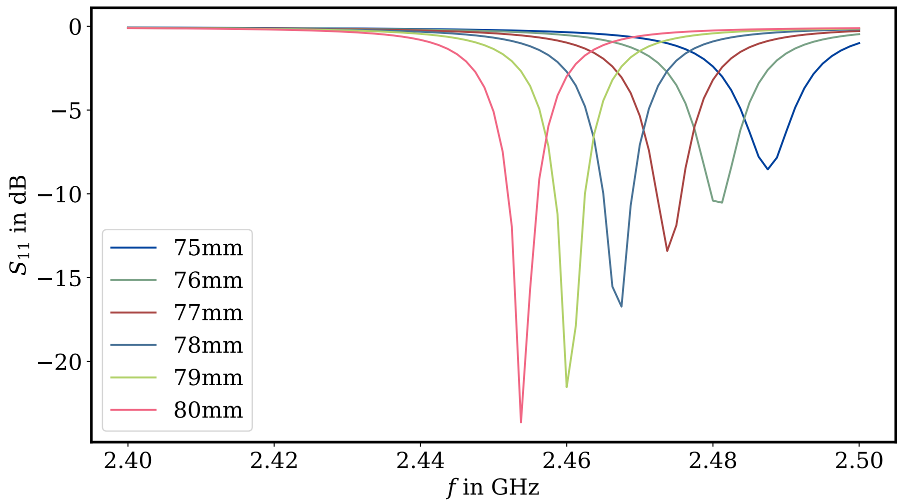

Figure 50: Simulated S_{11} parameter for different lengths of the SLAN with the COMSOL tool. We see a frequency shift, when the antenna is shortened by 5 mm. The best matched frequency increases with a decrease in length.

the best-matched frequency increases as the length decreases. For the multiple SLAN adaptations, detailed simulations at various parameters must be conducted to determine suitable length, radius, slot configuration, slot positions, launcher sizes, and angles relative to the slots. It has been observed that these parameters are interconnected. Thus, making a comprehensive simulation using tools such as COMSOL is essential for identifying the optimal dimensions of the SLAN.

It is found that with a shortened antenna the best matched frequency increases. As the microwave generator used in this study can go as high of 2500 MHz (with a resonance magnetic field required of 89.3 mT) an upper limit is given by the equipment available. As one can see a shortening of the antenna of about 5 mm of the antenna would still be usable with a frequency of 2490 MHz, therefore the ECR zone for 2490 MHz is shown in Figure 49.

If it is possible to shorten the antenna by 5 mm, applying 2.5 T disc magnets (instead of 1.4 T as currently in use) and placing the smaller ring magnet of 62 mm in repulsive configuration at the thruster exit, a magnetic field topology is reached as shown as DEEVAv2-rep62o in Figure 49. This configuration would allow for a steeper gradient in magnetic flux density than the MINOTOR prototype, and bring the ECR zone closer to the thruster exit reducing possible wall losses. Additionally its stronger magnetic field should lead to a better confinement and therefore an even better performance using xenon as propellant. Of course these are only ideas for possible improvements of the DEEVA prototype. If the performance and plasma parameter indeed improve with these adjustments needs to be tested.

4.3. Conclusion

The central focus of this work is to investigate how electrodeless microwave coupling, when combined with a specific magnetic field topology, affects plasma parameters and, ultimately, the thrust produced by the thruster system. This investigation is conducted using the DEEVA prototypes and compared to the MINOTOR prototype. The overarching goal is to understand the differences in performance between these systems, particularly in terms of thrust efficiency and plasma dynamics.

Five conclusions can be drawn:

MINOTOR Produces Higher Thrust in the Lower Power Range: MINOTOR is more efficient at producing thrust when operating at lower power levels. This is primarily because it harnesses MN effects more effectively than the current DEEVA prototypes, which enables a higher portion of the generated thrust (up to 50%) to be attributed to a high-energy ion beam. In contrast, the DEEVA prototypes, specifically in their early development stages, have not yet matched MINOTOR's thrust capabilities in this power range. However, the DEEVAv2-rep configuration using argon comes close to achieving a 50% ratio as well but still falls short in terms of absolute thrust output when compared to MINOTOR at similar power levels.

SLAN Coupling Requires a More Complex Magnetic Field Design: SLAN coupling, used in the DEEVA prototypes, requires a more intricate magnetic field topology to achieve similar plasma parameters and thrust levels than MINOTOR. Specifically, the SLAN design requires a larger region with parallel magnetic field lines, which later diverge to guide and accelerate the plasma effectively. This means the role of magnetic confinement and how well the magnetic field controls the plasma density and energy gradient is even more critical in SLAN-based systems compared to MINOTOR. In MINOTOR, the design of the magnetic field topology is more straightforward, making plasma confinement and acceleration easier.

SLAN Coupling Requires More Input Power: To achieve plasma parameters and thrust levels comparable to those produced by MINOTOR, SLAN coupling demands more input power. This is due to inherent power losses in SLAN's waveguide-based design. The waveguide character of SLAN means that energy is lost in the transmission process, reducing the overall efficiency. As a result, it takes more power to achieve similar results. The energy transfer mechanisms in MINOTOR's design is more efficient in comparison to the current development stage of the DEEVA prototype.

Power-Dependent Thrust and Plasma Characteristics Are Comparable: Despite the differences in coupling methods (electrodeless microwave coupling in DEEVA vs. coaxial coupling in MINOTOR), the overall effect on plasma parameters and thrust is comparable for both systems when input power is increased. In both cases, increasing power leads to a denser plasma population, and ultimately more thrust. This suggests that while the underlying mechanisms differ, the basic relationship between power and plasma production is consistent across both methods.

SLAN Offers Greater Flexibility in Operation: One key advantage of SLAN coupling, when combined with its specific magnetic field topology, is that it allows for greater flexibility in operation. This flexibility comes in the form of a wider range of power, frequency, volume flow rates, and choice of propellants. SLAN's ability to accommodate these variations makes it potentially more adaptable for different mission requirements or operational conditions compared to MINOTOR, which might be more limited in terms of the operational range or flexibility of propellant options.

In summary, while MINOTOR is more efficient at lower power levels due to its superior use of MN effects, SLAN coupling (as in the DEEVA prototypes) requires more input power and a more complex magnetic field design to achieve comparable thrust and plasma parameters but offers more operational flexibility. As the DEEVA thruster is a part of the DEEP project, its design has come to a point where demonstration on a satellite mission is in prospect. However its further development exhibits the immense opportunities: the DEEVA thruster consists of a simple design, can be operated in a repeatable manner with state-of-the-art performance on a level comparable to other technologies, without the lifetime limiting aspects of electrode erosion, and the circumvention of the need for a neutralizer. Given the number of unanswered questions raised by this work, it seems clear that the technological development is running ahead of the physical understanding of the system. However, the understanding of the thruster as a system is expected to strongly improve in future years with detailed investigations and simulations. The DEEVA concept making use of electrodeless microwave coupling into the plasma, electrodeless acceleration with a magnetic nozzle and avoiding the necessity for a neutralizer is a modern electric propulsion system. It potentially paves the way for long-term space missions employing ECR thrusters.

A. Appendix

We present and discuss additional relations and observations that support the results of the investigations described in the main text. While not essential to the primary narrative addressing the research questions, these elements provide valuable context. Topics include the analytical approach to estimating the thrust produced by the cold gas from the inlet, as well as investigations into magnet degradation and performance changes caused by variations in prototype operating parameters.

A.1. Additions to Fundamentals

In this section, we want to briefly discuss the analytical approach in estimating the thrust produced by the cold gas from the gas inlet.

We assume first of all an adiabatic expansion of an ideal gas to estimate analytically the thrust produced by the neutral gas injection. That means that we have to use the expansion/flow equations, for the temperature (T_0 in the reservoir and T_e at the nozzle exit), density (ρ_0 and ρ_e) and pressure (p_0 and p_e), as also shown in Figure 51:

$$\frac{T_\mathrm{e}}{T_0} = (1 + \frac{\kappa - 1}{2} M^2)^{-1}, \tag{A.1}$$

$$\frac{\rho_\mathrm{e}}{\rho_0} = (1 + \frac{\kappa - 1}{2} M^2)^{\frac{1}{\kappa - 1}}, \tag{A.2}$$

$$\frac{p_\mathrm{e}}{p_0} = (1 + \frac{\kappa - 1}{2} M^2)^{\frac{\kappa}{\kappa - 1}}, \tag{A.3}$$

which yield the relation of the exhaust velocity:

$$c_\mathrm{e} = \sqrt{\frac{2}{\kappa - 1} \kappa R (T_0 - T_\mathrm{e})} \tag{A.4}$$

$$= \sqrt{\frac{2}{\kappa - 1} \kappa R \left(T_0 - \left(\frac{p_\mathrm{e}}{p_0} \right)^{\frac{\kappa - 1}{\kappa}} T_0 \right)}. \tag{A.5}$$

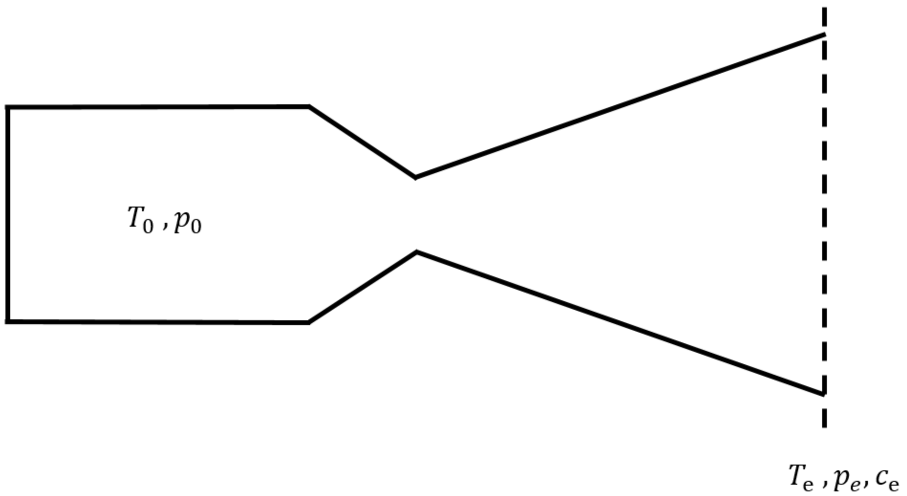

Figure 51: The gas is expanded from the reservoir at a pressure p_0 and a temperature T_0 (at mean velocity $c_0 = 0$) through the nozzle throat. From here, the gas is accelerated by expansion to the exit plane with area A_e- At the exit plane the temperature is T_e and the mean velocity is c_e.

With the adiabatic coefficient $\kappa = 1.67$, a gas constant $R = 63.33\,\mathrm{J/(kg\,K)}$ for xenon, a pre-pressure of $p_0 = 150\,\mathrm{kPa}$, a background/exit pressure within the chamber of $p_\mathrm{e} = 0.1\,\mathrm{Pa}$, at a temperature of $T_0 = 290\,\mathrm{K}$, we obtain an approximate exhaust velocity of $c_\mathrm{e} \approx 300\,\mathrm{m/s}$. What we now need is the mass flow of the gas (xenon in our case) - we therefore need to transform the volume flow sccm in a mass flow in kg/s. A mole of gas consists of $6.02\ \times 10^{23}$ particles (Avogadro's number) at standard pressure of 1 bar and standard temperature 0° C (273.15 K). With the mass of xenon of 131.293 u, we arrive to the equivalent mass flow rate of $1\,\mathrm{sccm} \approx 9.76 \times 10^{-8}\,\mathrm{kg/s}$. With the exhaust velocity and the mass flow of xenon (in this example at 1 sccm), we can derive the thrust produced by the cold gas injection with Equation 2.2:

$$T_\mathrm{T} = \dot{m}\,c_\mathrm{e} \tag{A.6}$$

$$\approx 3 \times 10^{-5}\,\mathrm{N} = 0.03\,\mathrm{mN}. \tag{A.7}$$

This simple estimation of thrust produced by the cold gas injection fits the measured thrust with cold gas obtained by the thrust balance quite well. The measured value of the thrust just by cold gas (so no plasma ignition) was determined to be $T_\mathrm{T} \approx 0.02\,\mathrm{mN}$, compare Figure 26. Besides the analytical estimation of the cold gas thrust and measuring the thrust by thrust balance, additional numerical investigations, covering a Fokker-Planck approach on the DEEVAv2 prototype, were performed. All three methods were compared and yielded a reasonable agreement in the lower flow rate regimes [81].

A.2. Additional Investigations and Results

A.2.1. Magnetic Field Degradation

Results of the degradation measurements of the DEEVAv2-attractive configuration can be seen in Figure 52 and Figure 53. Figure 52 shows a representation of the degradation of the magnets used in DEEVAv2-attractive case, and its effect on the magnetic field topology. The mask employed is in the simulation case not necessary but serves comparison reasons. In comparison to the simulation on the left, we see already after 5h operation (center plot) a decrease in magnetic field strength, coming together with a shift of the ECR zone in negative y-direction - closer to the strong disc magnets. The center plot is the magnetic field topology of the DEEVAv2 attractive configuration in Figure 29.

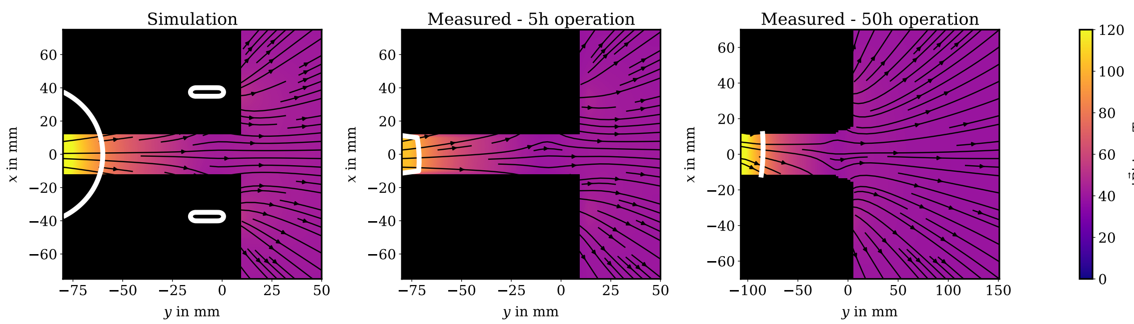

Figure 52: Representation of the degradation of the magnets used in DEEVAv2-attractive case, and its effect on the magnetic field topology. On the left plot we see a simulation of the magnetic field topology with the nominal parameters of the magnets - 1.4 T remanence for the disc magnets and 400 mT remanence of the ring ferrite magnet. The center plot depicts the magnetic flux density of the DEEVAv2-attractive prototype measured after approximately 5 h of operation. On the right hand side plot, we see the magnetic field topology after approximately 50 h of operation. $y = 0$ marks the position of the downstream plane of the ring magnet - ergo the thruster exit plane. As for $x = 0$ marks the centerline of the thruster. The colormap depicts the magnetic flux density, while the streamline vectors depict the magnetic field lines in the x, y plane. The white line indicates where the ECR condition is fulfilled at 2450 MHz - ergo a magnetic flux density of 87.5 mT.

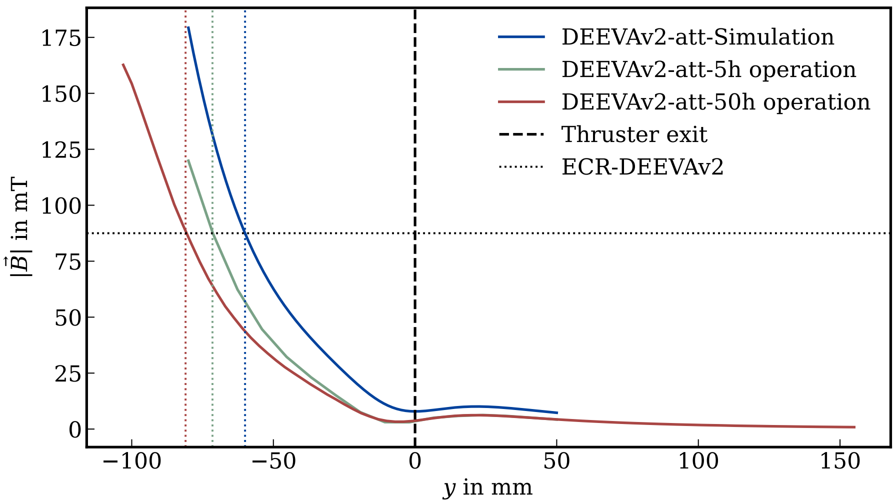

Figure 53: Representation of the simulated and measured magnetic flux density $|\vec{B}|$ along the centerline of the DEEVAv2-attractive thruster for different operational durations. The exit plane is marked at $y = 0\,\mathrm{mm}$ by the black dashed line. The ECR zones for the frequency of 2450 MHz are shown with dotted lines.

After 50h of operation (right plot), the magnetic flux density further decreases and the ECR zone shifts further to the gas inlet of the prototype. We see that the shape of the magnetic field lines (the diverging, converging-diverging character) seems to be preserved, however the strength of the magnetic field is rapidly decreasing with operational time of the thruster. We attribute these changes primarily to handling and the heating of the thruster. It is well known that mechanical impact on permanent magnets can lead to a change in their remanence and, consequently, their magnetic field. In addition to the implementations and modifications made to the thruster - ultimately resulting in mechanical impacts - we cannot rule out the possibility that the specifications of the magnets are still valid upon delivery. Furthermore, particle impacts on the magnets, particularly the ferrite ring magnet, can also alter the magnet characteristics. A more significant factor the magnets must endure is the heating of the thruster. Temperature measurements indicate that the thruster can heat up to 60° C. The temperature sensors were placed on the antenna, so it remains uncertain how hot the magnets actually get. This observation may help explain the asymmetry of the magnetic field after prolonged operational time.

Figure 53 is a representation of the magnetic flux density $|\vec{B}|$ along the centerline of the DEEVAv2-attractive thruster for different operational durations. As shown, the simulation predicts the closest ECR zone to the thruster exit plane, which results in reduced wall losses. Additionally, the gradient of the magnetic field is higher in the simulation, leading to greater acceleration of the plasma. While the overall curve of the magnetic flux density is consistent even after extended operational time, a shift of approximately 10 mm in the ECR zone is already observed after 5 h of operation. After 50 h of operation, a shift of 20 mm is detected.

A.2.2. Supplementary Thrust Balance Results

Thrust balance results for krypton

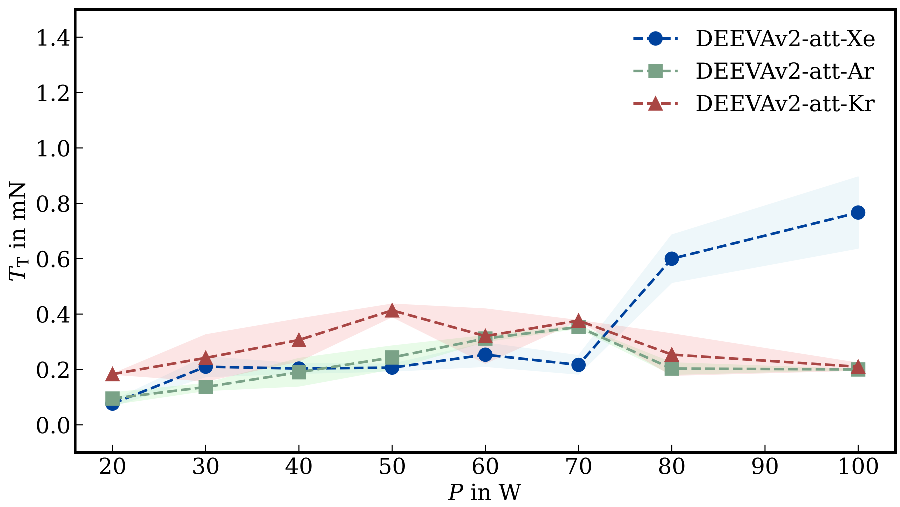

Figure 54: Thrust balance measurements on the DEEVAv2-attractive configuration for three different propellants; xenon, argon and krypton. The thrust T_T is measured in dependence on input power P. The volume flow is for all three propellants set to 1 sccm and the excitation frequency is 2450 MHz.

Results of thrust balance measurements on the DEEVAv2-attractive configuration for three different propellants - xenon, argon and krypton - can be seen in Figure 54. The thrust T_T is depicted versus input power variation P. Xenon operation (represented by the blue line) leads to the highest thrust of about 0.8 mN at 100 W input power, while argon and krypton do not exceed 0.4 mN. Interestingly, at lower power levels, argon exhibits the highest thrust despite its smaller mass. Krypton, which lies between xenon and argon in the periodic table, has a smaller ionization energy and a higher mass than argon. One might assume that these properties would result in thrust values lying between those of the other two propellants; it seems that, with respect to thrust, krypton performs closer to argon than to xenon. The reasons for these differing performances with the various propellants remain an open question.

Variation of operational parameter

Results of thrust balance measurements on the MINOTOR, DEEVAv1, DEEVAv2-attractive and DEEVAv2-repulsive configuration for a variation of frequency and volume flow can be seen in Figure 55. For an increase in volume flow, especially in case of MINOTOR the thrust measured decreases. No significant effect of increasing volume flow on measured thrust can be observed for the DEEVAv2 configurations. However, for the DEEVAv1 prototype an increase in thrust with increasing volume flow can be observed. This is again a strong indication that for the DEEVAv1 prototype the main contribution to thrust production comes from the neutral gas injection itself and is not attributed to plasma effects, as it can be clearly observed in Figure 66 (and also in Figure 39). The ion energy and the ion beam current decreases for increasing volume flow, therefore an increase in thrust with increase in volume flow can be directly linked to the gas injection. As for frequency variation, we see an optimum value for MINOTOR at the design frequency of 2.45 GHz, and for the DEEVAv2-attractive at 2.44 GHz. For both, the DEEVAv2-repulsive and the DEEVAv1, we see no clear dependence on excitation frequency. As for none of the DEEVA prototypes such a pronounced frequency dependence is observed as for the MINOTOR prototype, it can be concluded that the waveguide character of the SLAN leads to a broader operation bandwidth with respect to microwave frequency. Nevertheless

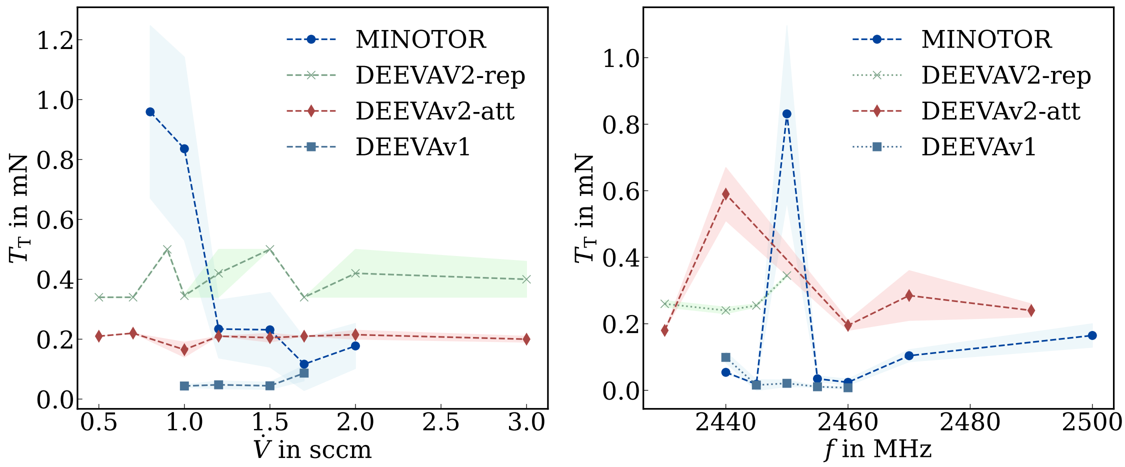

Figure 55: Thrust balance measurement data on the MINOTOR, DEEVAv1, DEEVAv2-attractive and DEEVAv2-repulsive configuration for a variation of frequency and volume flow. The propellant in use is xenon. The input power for all the prototypes is 30 W. In case of the variation of volume flow the frequency is set to 2450 MHz; in case of the frequency variation the volume flow is set to 1 sccm.

there is still an optimum frequency observable, however, the decrease in performance with deviation from this optimal frequency is not as significant as for the MINOTOR prototype. This possible advantage needs to be further investigated.

A.2.3. Supplementary Plasma Properties Results

Influence of variation of operational parameter on ion energy

Plots of ion energies of maximum probability determined for the two DEEVAv2 configurations for different propellants for power, frequency, and volume flow variation can be seen in Figure 56. The propellants in use are xenon, argon and krypton. We see for all the operational variations the highest ion energies in case of argon operation, followed by krypton and xenon. Interestingly even though krypton lies with its characteristics (mass and ionization energy) closer to argon than to xenon, the determined results for krypton are closer to those for xenon as propellant over all operational parameter variations. We also see that the DEEVAv2-repulsive configuration delivers independent of the propellant in use, higher ion energy values than the attractive configuration. As for the observed trends, we see for both configurations and all the propellants an increase in ion energy with increase of input power. There seems to be no significant influence regarding frequency variation. For the increase in volume flow, for all the configurations and propellants a decrease in ion energy can be observed, while the effect in case of argon as propellant is the most prominent. It has to be mentioned at this point, that the discharge is easier to preserve at lower volume flows when using xenon than using argon. Therefore the operation with xenon as propellant is still possible down to 0.4 sccm, while the limit for argon operation is 0.8 sccm. The limit for krypton is 0.6 sccm.

It is observed that the extraction is improved and the ion energies are increasing at very low volume flows. If it were possible to further decrease the volume flow of xenon without that the thruster turns off, it could be possible that the ion energies approach the values of argon operation. However, in the current setup, it is not feasible to operate the prototype at such low volume flows of xenon. If this is indeed due to the inherent thruster characteristics or due to the mass flow control unit's accuracy (it is possible that the minimum flow control is 0.2 sccm and therefore there is simply no neutral gas injection anymore at such low volume flows) is not clear at this point.

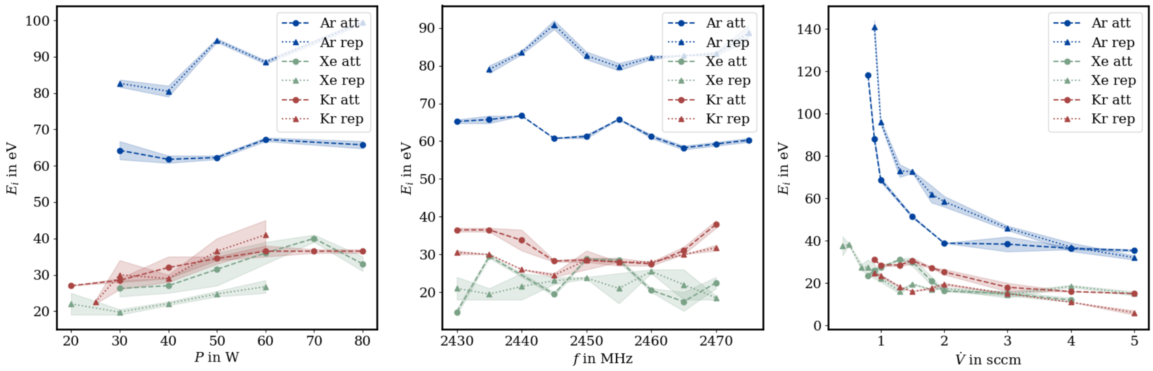

Figure 56: Ion energies with maximum probability determined for the two DEEVAv2 configurations for different propellants for power variation (left), frequency variation (center) and volume flow variation (right). The propellants in use are xenon, argon and krypton. For the power variation an excitation frequency of 2450 MHz and a volume flow of 1 sccm is employed; for frequency variation we keep 30 W and a volume flow of 1 sccm; and for the volume flow variation a frequency of 2450 MHz and a power of 30 W is set.

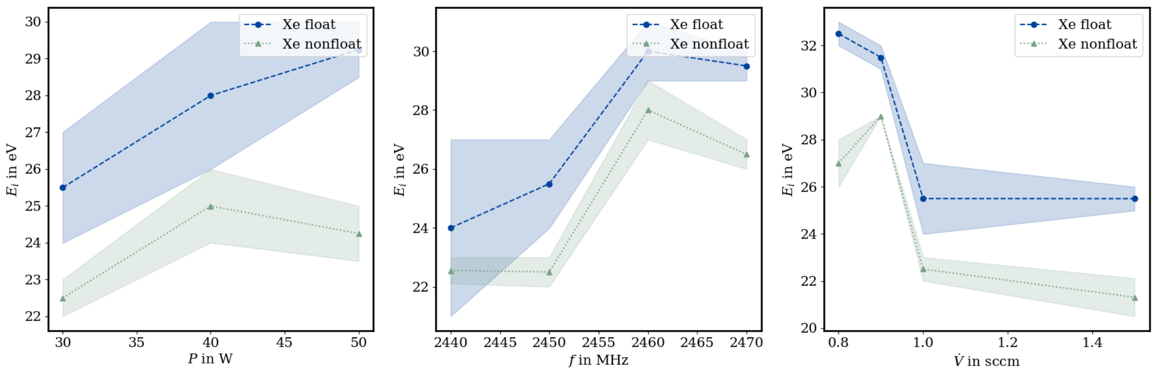

Figure 57: Influence on ion energy of floating or grounded (nonfloat) operation of a DEEVAv2-attractive configuration operated with xenon at variable power input setting, frequency and volume flow variation. On the left, the power variation at 2450 MHz and 1 sccm xenon is shown. The center plot shows the frequency variation at a fixed power of 30 W and 1 sccm. On the right plot the volume flow variation at 2450 MHz and 30 W input power is depicted.

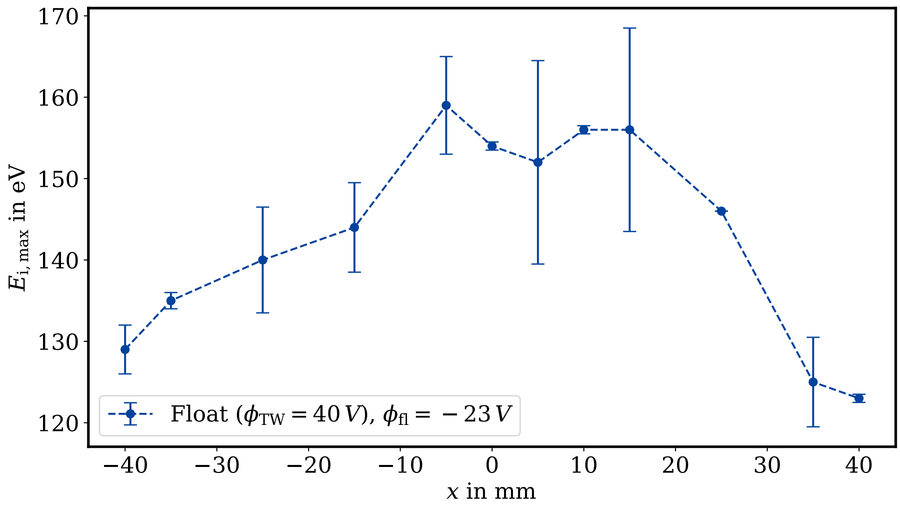

Figure 58: Plot of the beam scan of the ion energy of maximum probability of MINOTOR at standard conditions of 30 W, 2.45 GHz and 1 sccm xenon. The detector is placed at a distance of 10 cm from the thruster exit plane. The thruster is kept in floating condition, the thruster potential ϕ_{TW} as well as the floating grid potential ϕ_{fl} are additionally given in the graph. For each x position in the beam multiple measurements are performed and their standard deviation is given as error bars.

The effect on ion energy of floating or grounded operation of the DEEVAv2-attractive configuration operated with xenon at variable power input setting, frequency and volume flow variation can be seen in Figure 57. We observe on the left plot, for both operational modes, floating and grounded, the similar trend that with increase in power the ion energy of maximum probability also increases. As for the center plot, both operational conditions exhibit the optimal frequency of about 2460 MHz. In case of the volume flow variation (on the right plot), both operational conditions exhibit a decrease in ion energy with increase of volume flow. We see over all parameter variations higher ion energies for the thruster in floating mode of about 2 eV. The trends for both operation modes (floating or grounded) are comparable over the operational parameter variations.

Beam scan of ion energy

Figure 58 shows results of beam scan measurements of the ion energy of maximum probability of MINOTOR at standard conditions. A double peak structure seems to be observable in the curve of the ion energy of maximum probability across the beam, comparable to the ion current beam scans shown in Figure 43. This could be explained by the two gas inlets. A variation of the ion energy with maximum probability from the center to the edge of the beam of about 30 eV can be observed. It is clearly shown that the ion energy differs depending on the measurement position in the beam. This is relevant for the determination of the force determined by the probe measurements, as we assume a homogeneous ion energy in the beam, which is clearly not given. However, it goes beyond the scope of this work to investigate the difference in ion energy profiles for all the prototypes at all the operational conditions. Therefore, the effect of different ion energy distribution functions depending on the position in the beam is chosen to be neglected.

Influence of variation of operational parameter on electron temperature

Electron temperature measurement results for the prototypes for varying microwave frequency and different input power can be seen in Figure 59. For MINOTOR and DEEVAv1 xenon is used as propellant. Argon is used in case of DEEVAv2. The highest electron temperatures are reached with the

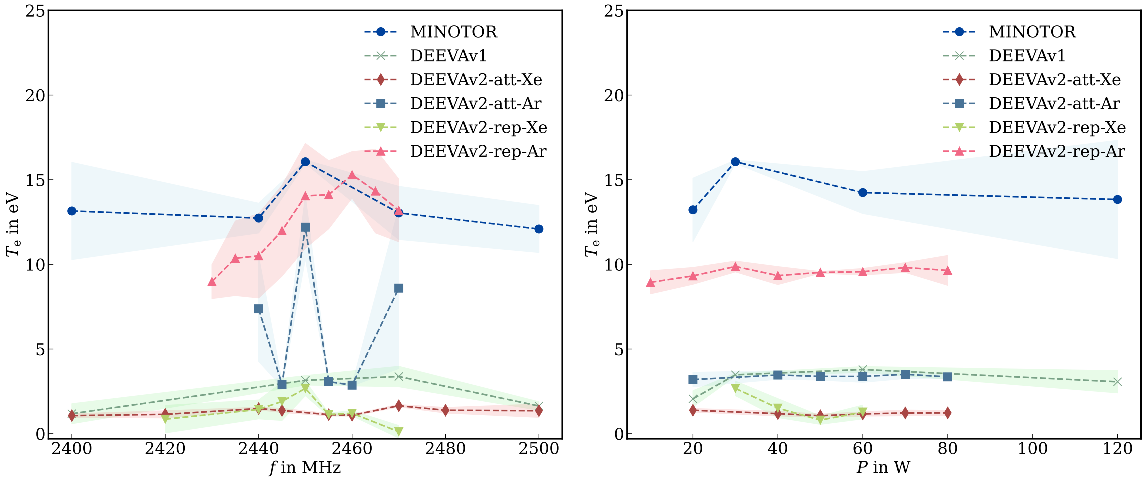

Figure 59: Plots of the electron temperature for the prototypes for varying microwave frequency and different input power. For MINOTOR and DEEVAv1 xenon is used as propellant; in case of DEEVAv2, argon. The left plot shows the frequency variation at a fixed power of 30 W and 1 sccm. On the right, the power variation at 2450 MHz and 1 sccm xenon is shown.

MINOTOR prototype, and the DEEVAv2-rep configuration operated with argon. Here we determine up to 17 eV. As for the frequency variation at 30 W and 1 sccm volume flow, we see higher values around the design frequency of 2.45 GHz in case of MINOTOR and DEEVAv2 configurations (att and rep) operated with argon. When operated with xenon, the DEEVAv2 configurations show similar electron temperatures as the DEEVAv1 prototype not exceeding 5 eV. As for the power variation plot on the right, no prototype's electron temperature seems to be influenced by the input power significantly. This could hint towards the circumstance that not all the microwave power is coupled into the electron system or significant losses occur. However since the electron temperature is the driving force of the ion energy in the system of a magnetic nozzle (compare Chapter 2), and we measure higher ion energies with increase in input power (and higher ion beam current and thrust as well) the only explanation that remains is that with increase in power the ion beam current increases as shown in Figure 45. The observation that the power input influences the ion beam current and not the electron temperature in the plume and with that the ion energy can also be seen in Figure 41.

A.2.4. Supplementary Faraday cup Investigations

Role of orientation of FC in beam

A depiction of the incidence angle correction of the Faraday cup array at the JUMBO facility can be seen in Figure 60. On the top an exemplary sketch is shown, where the thruster is assumed to be a point source. As we are dealing with very small thruster exit planes not exceeding 5 cm in diameter, and are measuring at a distance of 66 cm from the exit plane, the assumption of a point source is adequate. The divergence angle β is shown. It is assumed that the particles leave the thruster exit plane along a linear trajectory. This assumption however is more or less adequate, as we do not know how the detachment of the plasma from the magnetic field lines takes place. Especially in close vicinity to the thruster and at higher volume flows, it could be observed that the plasma follows the magnetic field lines. This could also hold true for the reported experiments and was just not been observed. Due to the lack of the knowledge of the exact beam shape, the assumption of linear trajectories has to be made. Depending on the position within the beam the incidence angle has be taken into account to account for the particles that do not reach the detector due to spatial restrictions. On the bottom plot in Figure 60 the correction value of the measured current for different distances of the FC array towards the thruster exit plane is shown.

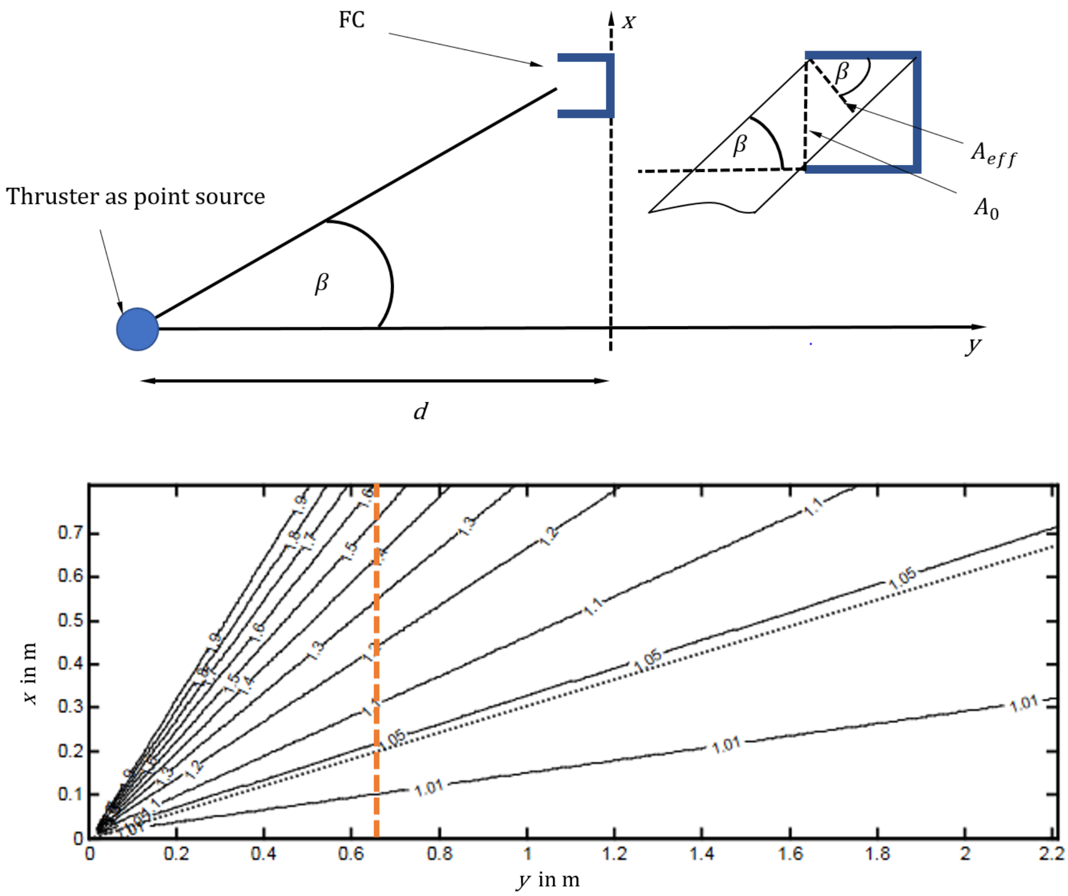

Figure 60: Depiction of the incidence angle correction of the Faraday cup array at the JUMBO facility. On the top an exemplary sketch is shown, where the thruster is assumed to be a point source. The divergence angle β is shown. It is furthermore assumed that the particles leave the thruster exit plane along a linear trajectory. Therefore, the current impinging on the detector corresponds to a smaller effective detector area $A_{\text{eff}} = A_0 \cos(\beta)$. In the bottom graph the correction value of the measured current for different distances of the FC array towards the thruster exit plane is given as $1/\cos(\beta)$. As we are performing our measurements at a distance of 66 cm, the corresponding correction values can be taken and have to be taken into account. Sketch and correction value are adapted from Ref. 82.

As we are performing our measurements at a distance of 66 cm from the thruster exit plane, the corresponding correction values have to be taken into account and resulting values are shown in Figure 44.

The assumption of the thruster as a point source is adequate, if the diagnostic is placed at least half a meter from the thruster exit plane (as it is the case in JUMBO facility). As the FC is placed much closer to the thruster in the STG-MT facility, the assumption of a point source is no longer valid. Therefore investigations regarding the role of orientation of the FC grid with respect to the thruster exit plane have to be conducted. The measurement procedure is performed as follows: For the beam scans the FC is moved with the linear axis at 2 mm/s from -75 mm to +75 mm and the current is measured. In order to obtain information about the divergence (angle) depending on the position in the beam, the detector is mounted on a rotational axis which is moved by the linear scanner. With this set up, rotation curves of the detector response can be recorded at multiple positions in the beam, i.e. the ion current as a function of angle by which the FC is rotated to the thruster exit plane can be recorded at a fixed position x. The set up as well as examples of the angle dependent raw detector currents can be seen in Figure 61.

It is now possible to check if the current value determined with the rotational set up at zero degrees delivers the same values as the beam scan without the rotational axis, at the specific positions. Corresponding curves can be seen in Figure 62. As it is to be expected the FC at zero degree rotation delivers the same raw current value as the beam scan. The results for the spatial points x shown are also the points from which the correction function can be determined.

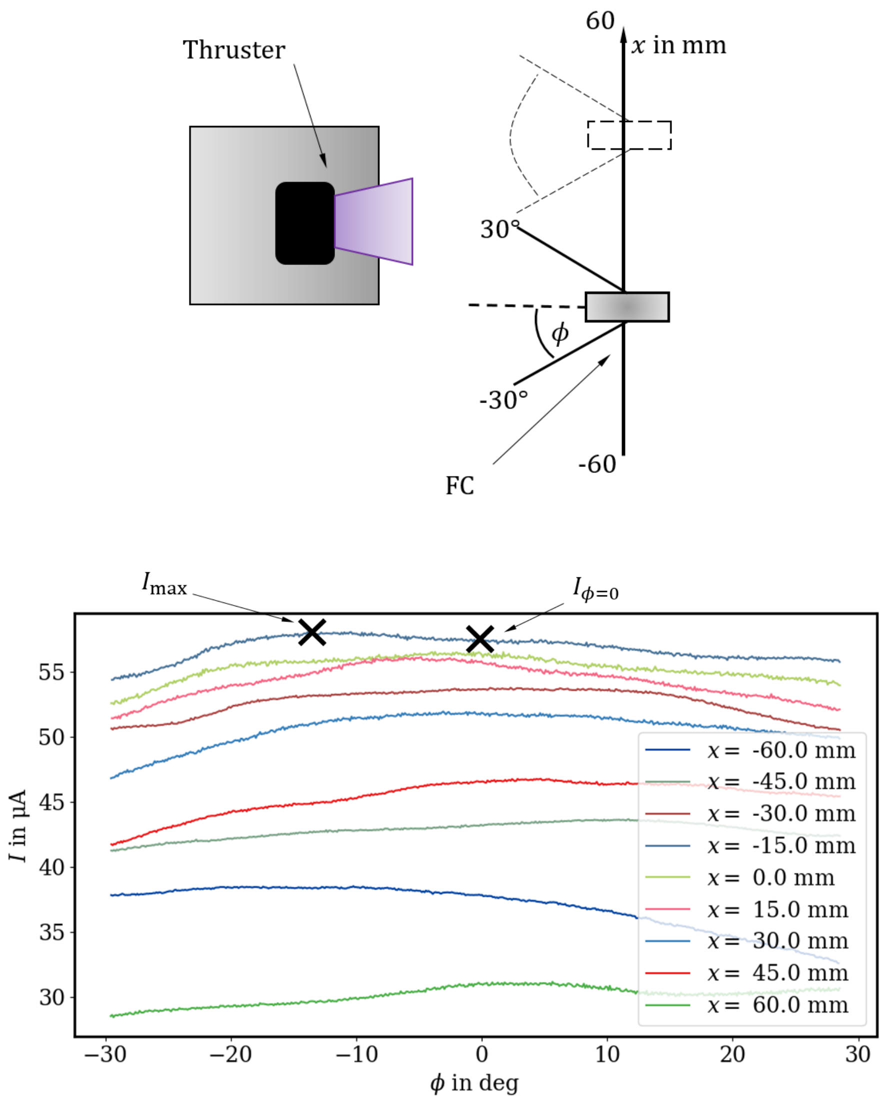

Figure 61: Measurement procedure for the angle correction of FC beam scan measurements in the STG-MT. For the beam scans the FC is moved with the linear axis at 2 mm/s from -60 mm to +60 mm and the current is measured. At each position x, the FC is rotated between $-30°$ and $30°$. With this set up, rotation curves can be recorded at multiple positions in the beam, i.e., the raw current values I as a function of the angle by which the FC is rotated to the thruster exit plane ϕ, see bottom plot.

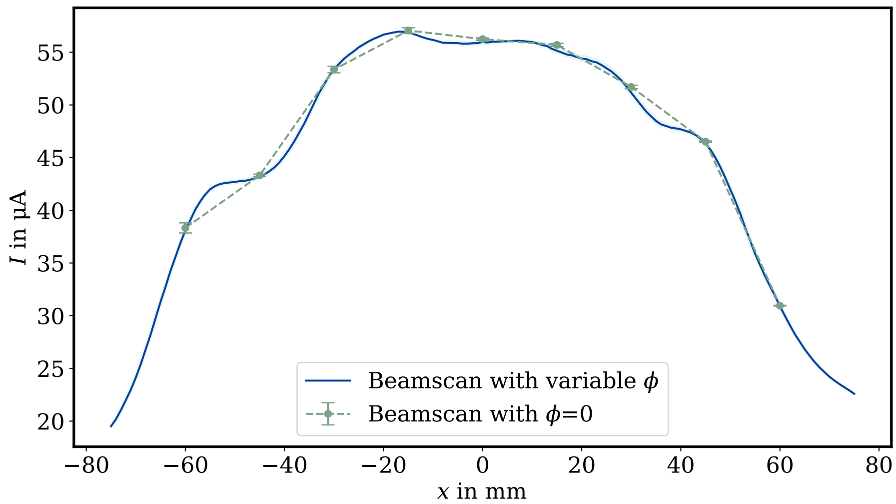

Figure 62: Comparison of the beam scan measurements with a fixed position of the FC and the zero angle position of the FC on the rotational stage at a distance of 20 cm to the thruster exit plane. The thruster in this case is the DEEVAv2-att configuration operated with argon at 30 W, 2.45 GHz and 1 sccm. The repeller of the Faraday cup is biased with -40 V relative to ground in order to repel the electrons within the beam.

We want to determine the angle correction value with which raw linear beam scans can be correlated to achieve an angle corrected estimation of the total ion beam current. For this we firstly determine the ratio of the maximum current value of the rotation measurements $I_{\max}$ and the current at zero degree rotation ($\phi = 0$) $I_{\phi=0}$, for all measured positions of a operational point is made. This ratio (or coefficient) for the multiple positions in the beam, can now be used to formulate a correction function, as it can be seen in Figure 63. The highest deviation of the maximum ion current value and the zero degree value is located at the edge of the beam profile in negative x direction. This indicates that the divergence within the beam is not axis symmetric. However, the ratio shows not much of a dependence of the position in the beam, and shows only deviations of about 5 %.

This interpolated correction function can then be multiplied by the raw measured ion current of the beam scan, to reach a corrected current measurement, see Figure 64. The total ion beam current with these corrected current profiles are about 1 to 5% higher than the currents from uncorrected current profiles. If one considers that the total currents are only to be seen as an estimates, due to the assumption of rotational symmetry, and the error bars of these current measurements overlay this percentage, an error of 1 to 5% is a negligible effect. Therefore, if a linear beam scan is performed to estimate the total current the angular dependence of the ion current from the thruster can be neglected.

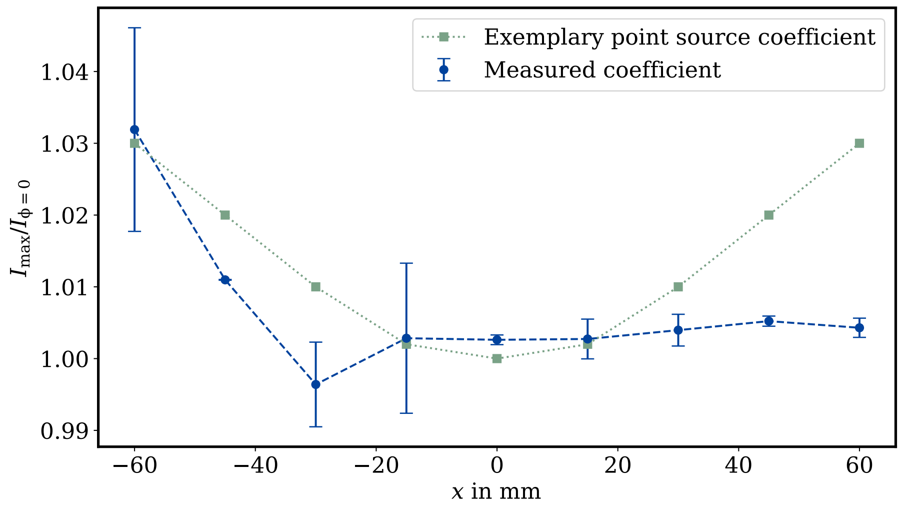

Figure 63: Ratio of the maximum current determined with the rotational measurements $I_{\max}$ and the current at zero degrees rotation $I_{\phi=0}$ for the positions in the beam. We show measured data, as well as an exemplary curve for a point source relation ($I_{\max}/I_{\max} = \cos(\phi)$).

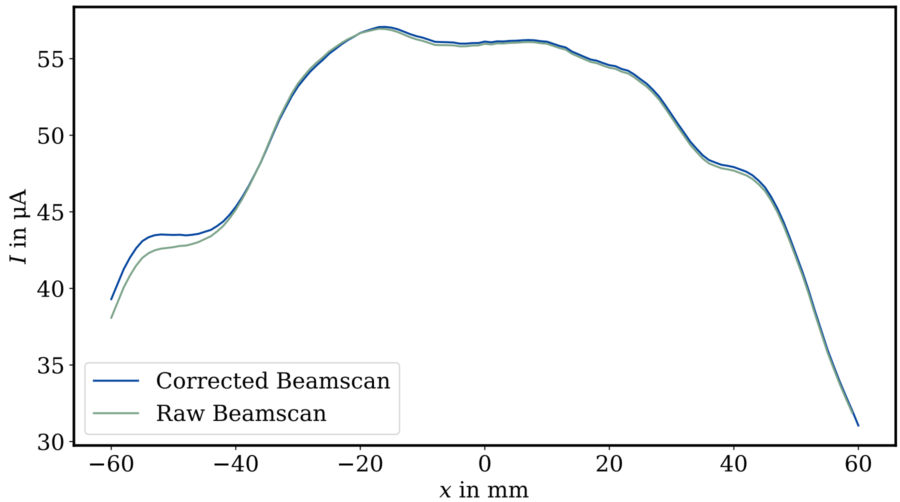

Figure 64: Raw current measurement of the FC beam scan, as well as the corrected current measurement after applying a correction function. The asymmetry of the beam divergence, leading to an asymmetrical correction function, leads therefore to a higher correction of the measured current at the edge of the beam on the negative x axis.

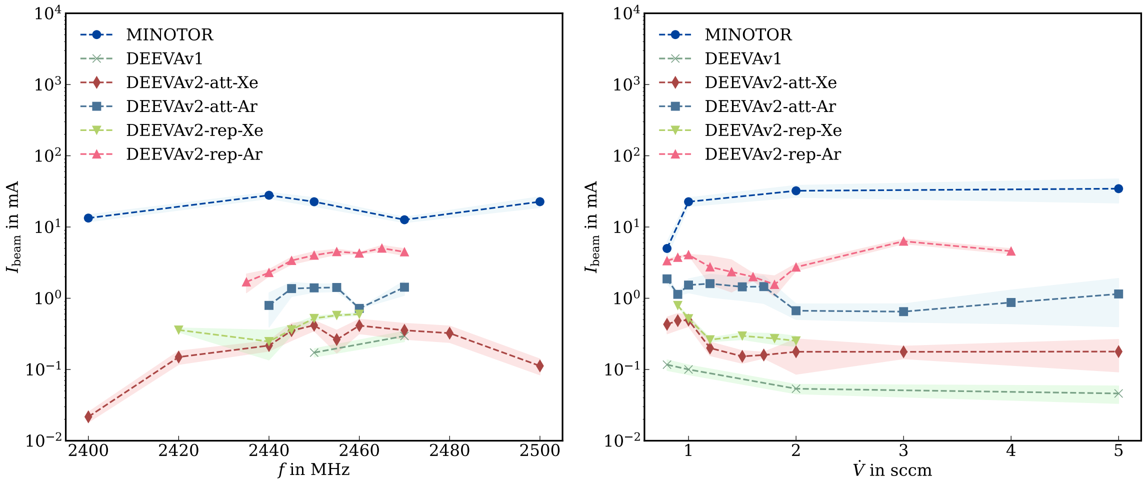

Figure 65: Values of ion beam current measurements of the thruster prototypes for various frequencies and volume flow settings. MINOTOR and DEEVAv1 are operated with xenon, the DEEVAv2 prototypes with argon and xenon. The left plot shows the frequency variation at a fixed power of 30 W and fixed volume flow of 1 sccm. On the right, the volume flow variation at fixed frequency of 2450 MHz and fixed power setting of 30 W is shown.

Influence of variation of operational parameters on ion beam current

Figure 65 presents results of ion beam current measurements of the thruster prototypes for various excitation frequencies and volume flow settings. MINOTOR and DEEVAv1 are operated with xenon, the DEEVAv2 prototypes with argon and xenon. For the frequency variation, we see the highest ion beam current for the MINOTOR prototype and the DEEVAv2-repulsive configuration operated with argon. The smallest ion beam currents are extracted with the DEEVAv1 and the DEEVAv2-attractive configuration operated with xenon. The same observation holds for the volume flow variation. We see a saturation of ion beam current with increasing volume flow in the trends of the MINOTOR prototype. It is possible that a similar behavior can be observed for the DEEVAv2 prototype operated with argon, however, not as clearly.

A.2.5. DEEVAv1 Observations

A comparison between the force determined by probe measurements and the thrust determined by thrust balance measurements in case of volume flow variation of the DEEVAv1 prototype operated at 30 W and a frequency of 2450 MHz can be seen in Figure 66. The thrust balance results show a clear increase with increasing volume flow. Whereas the force estimated from probe measurements of the plasma parameters (with RPA and FC) exhibit a clear decrease with increasing volume flow. The force determination is in accordance with a decrease in ion beam current and ion energy in case of volume flow increase, as it can be seen in Figures 65 and 39. Therefore, the thrust balance results in Figure 66 are a clear indication for thrust production by neutral gas in case of the DEEVAv1 prototype.

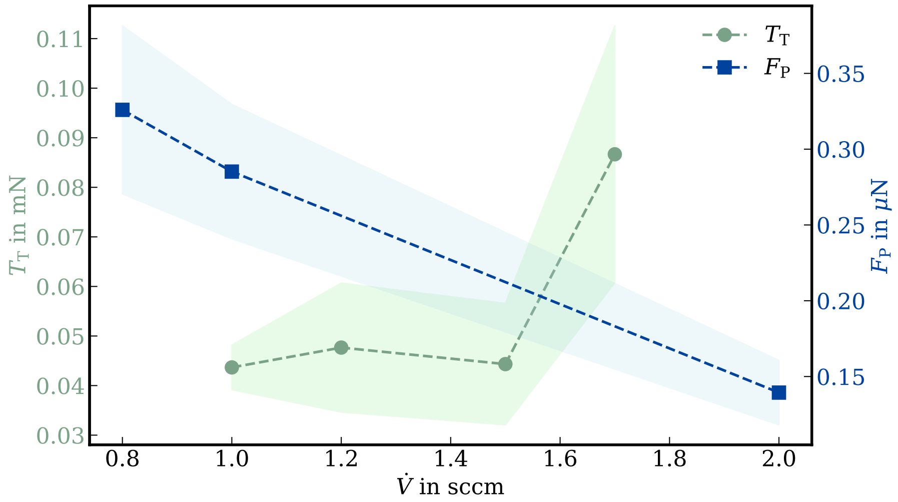

Figure 66: Comparison between the force determined by probe measurements and the thrust determined by thrust balance measurements in case of volume flow variation of the DEEVAv1 prototype operated at 30 W and a frequency of 2450 MHz. On the left axis the thrust balance results can be seen, showing a clear increase with increasing volume flow. On the right scale we see the force determined with probe measurements (with RPA and FC).

Bibliography

[1] K. Holste et al. "Ion thrusters for electric propulsion: Scientific issues developing a niche technology into a game changer". In: *Review of Scientific Instruments* Vol. 91. (2020), p. 061101.

[2] S. Mazouffre. "Electric propulsion for satellites and spacecraft: established technologies and novel approaches". In: *Plasma Sources Science and Technology* Vol. 25. (2016), p. 033002.

[3] U. Stroth. *Plasmaphysik*. Springer, 2011. Chap. 2,9.

[4] M.A. Lieberman and A.J. Lichtenberg. *Principles of plasma discharges and materials processing*. 2nd Edition. John Wiley & Sons, 2005.

[5] D.M. Goebel and I. Katz. *Fundamentals of electric propulsion: Ion and Hall thrusters*. Vol. 1. JPL Space Science and Technology Series. John Wiley & Sons, 2008.

[6] H. Kuninaka and S. Satori. "Development and demonstration of a cathodeless electron cyclotron resonance ion thruster". In: *Journal of Propulsion and Power* Vol. 14. (1998), pp. 1022–1026.

[7] G. Coral et al. "Microwave power absorption to high energy electrons in the ECR ion thruster". In: *Plasma Sources Science and Technology* Vol. 27. (2018), p. 095015.

[8] Y. Tani et al. "Performance improvement of the μ10 microwave discharge ion thruster by expansion of the plasma production volume". In: *Acta Astronautica* Vol. 157 (2019), pp. 425–434.

[9] Y. Nakagawa et al. "Water and xenon ECR ion thruster—comparison in global model and experiment". In: *Plasma Sources Science and Technology* Vol. 29. (2020), p. 105003.

[10] S. Meng et al. "Investigation on the radial distribution of electron density in a miniaturized ECR ion thruster of wide-range operations". In: *Vacuum* Vol. 202 (2022), p. 111138.

[11] J.Y. Kim et al. "Kinetic electron cooling in magnetic nozzle: Experiments and modeling". In: *Plasma Sources Science and Technology* Vol. 32 (2022), p. 073001.

[12] M. Merino and E. Ahedo. "Magnetic nozzles for space plasma thrusters". In: *Encyclopedia of Plasma Technology* Vol. 2 (2017), pp. 1329–1351.

[13] E. Choueiri. "Scaling of thrust in self-field magnetoplasmadynamic thrusters". In: *Journal of Propulsion and Power* Vol. 14. (1998), pp. 744–753.

[14] K. Takahashi et al. "Performance improvement of a permanent magnet helicon plasma thruster". In: *Journal of Physics D: Applied Physics* Vol. 46. (2013), p. 352001.

[15] F.F. Chen. "Helicon discharges and sources: a review". In: *Plasma Sources Science and Technology* Vol. 24. (2015), p. 014001.

[16] C. Charles, R. Boswell, and K. Takahashi. "Boltzmann expansion in a radiofrequency conical helicon thruster operating in xenon and argon". In: *Applied Physics Letters* Vol. 102. (2013), p. 223510.

[17] K. Takahashi et al. "High temperature electrons exhausted from rf plasma sources along a magnetic nozzle". In: *Physics of Plasmas* Vol. 24. (2017), p. 084503.

[18] Y. Zhang, C. Charles, and R. Boswell. "Measurement of bi-directional ion acceleration along a convergent-divergent magnetic nozzle". In: *Applied Physics Letters* Vol. 108. (2016), p. 104101.

[19] K. Takahashi. "Helicon-type radiofrequency plasma thrusters and magnetic plasma nozzles". In: *Reviews of Modern Plasma Physics* Vol. 3. (2019), pp. 1–61.

[20] B.W. Longmier et al. "Ambipolar ion acceleration in an expanding magnetic nozzle". In: *Plasma Sources Science and Technology* Vol. 20. (2011), p. 015007.

[21] C.S. Olsen et al. "Investigation of plasma detachment from a magnetic nozzle in the plume of the VX-200 magnetoplasma thruster". In: *IEEE Transactions on Plasma Science* Vol. 43. (2014), pp. 252–268.

[22] D. Miller, E. Gibbons, and P. Gloersen. "Cyclotron resonance propulsion system". In: *AIAA Electric Propulsion Conference* (Colorado Springs, USA). 1963, p. 2.

[23] S. Peterschmitt. “Development of a stable and efficient electron cyclotron resonance thruster with magnetic nozzle”. PhD thesis. Institut polytechnique de Paris, 2020.

[24] M. Nagatomo. “Plasma acceleration by high frequency electromagnetic wave in staticmagnetic field gradient”. In: *6th Electric Propulsion and Plasmadynamics Conference* (Colorado Springs, USA). 1967, p. 660.

[25] J. Sercel. “Electron-cyclotron-resonance (ECR) plasma acceleration”. In: *19th AIAA, Fluid Dynamics, Plasma Dynamics, and Lasers Conference* (Honolulu, Hawaii). 1987.

[26] J. Sercel. “Electron-cyclotron-resonance (ECR) plasma thruster research”. In: *24th AIAA / ASME/SAE/ASEE Joint Propulsion Conference & Exhibit* (Boston, USA). 1988.

[27] D. Kaufman, D. Goodwin, and J. Sercel. “Experimental studies of an ECR plasma thruster”. In: *29th AIAA/ASME/SAE/ASEE Joint Propulsion Conference & Exhibit* (Monterey, USA). 1993.

[28] S. Larigaldie. *Plasma thruster and method for generating a plasma propulsion thrust.* US Patent 9,591,741. 2017.

[29] J. Jarrige et al. “Characterization of a coaxial ECR plasma thruster”. In: *44th AIAA Plasmadynamics and Lasers Conference* (San Diego, USA). 2013, p. 2628.

[30] F. Cannat et al. “Optimization of a coaxial electron cyclotron resonance plasma thruster with an analytical model”. In: *Physics of Plasmas* Vol. 22. (2015), p. 053503.

[31] T. Vialis, J. Jarrige, and D. Packan. “Geometry optimization and effect of gas propellant in an electron cyclotron resonance plasma thruster”. In: *35th International Electric Propulsion Conference* (Atlanta, USA). 2017, pp. 1–12.

[32] D. Packan et al. “H2020 MINOTOR: Magnetic Nozzle Electron Cyclotron Resonance Thruster”. In: *36th International Electric Propulsion Conference* (Vienna, Austria). 2019.

[33] S. Correyero et al. “Plasma beam characterization along the magnetic nozzle of an ECR thruster”. In: *Plasma Sources Science and Technology* Vol. 28. (2019), p. 095004.

[34] S. Correyero Plaza et al. “Measurement of anisotropic plasma properties along the magnetic nozzle expansion of an Electron Cyclotron Resonance Thruster”. In: *35th International Electric Propulsion Conference* (Atlanta, USA). 2017.

[35] S. Peterschmitt and D. Packan. “Comparison of waveguide coupled and coaxial coupled ECRA magnetic nozzle thruster using a thrust balance”. In: *36th International Electric Propulsion Conference* (Vienna, Austria). 2019.

[36] M.R. Inchingolo, M. Merino, and J. Navarro-Cavallé. “Plume characterization of a waveguide ECR thruster”. In: *Journal of Applied Physics* Vol. 133. (2023), p. 113304.

[37] A. Ganguli et al. “Development and studies on a compact electron cyclotron resonance plasma source”. In: *Plasma Sources Science and Technology* Vol. 25. (2016), p. 025026.

[38] A. Ganguli et al. “Evaluation of compact ECR plasma source for thruster applications”. In: *Plasma Sources Science and Technology* Vol. 28. (2019), p. 035014.

[39] R. Moloney et al. “Experimental validation and performance measurements of an ECR thruster operating on multiple propellants”. In: *36th International Electric Propulsion Conference* (Vienna, Austria). 2019.

[40] J. Schmidt, J. Simon, and M. Grabe. “The DEEP Thruster Concept”. In: *37th International Electric Propulsion Conference* (Boston, USA). 2022.

[41] F. Werner, D. Korzec, and J. Engemann. “Slot antenna 2.45 GHz microwave plasma source”. In: *Plasma Sources Science and Technology* Vol. 3. (1994), p. 473.

[42] D. Korzec et al. “Scaling of microwave slot antenna (SLAN): a concept for efficient plasma generation”. In: *Plasma Sources Science and Technology* Vol. 5. (1996), p. 216.

[43] J. Engemann and M. Walter. “Modelling of microwave plasma sources: potential and applications”. In: *Plasma Physics and Controlled Fusion* Vol. 41. (1999), p. 259.

[44] R. Winter, D. Korzec, and J. Engemann. "Remote and direct cleaning by use of microwave plasma source SLAN II: comparative study". In: *Surface and Coatings Technology* Vol. 91. (1997), pp. 101–106.

[45] E. Messerschmid and S. Fasoulas. *Raumfahrtsysteme*. 4th Edition. Vol. 2. Springer, 2011.

[46] V. Hugonnaud. "Plasma probe measurements for electric propulsion device ion beam: Optimization and standardization". PhD thesis. Technische Universität Wien, 2022.

[47] A. Fridman and L.A. Kennedy. *Plasma physics and engineering*. CRC press, 2004.

[48] M. Merino, J. Nuez, and E. Ahedo. "Fluid-kinetic model of a propulsive magnetic nozzle". In: *Plasma Sources Science and Technology* Vol. 30. (2021), p. 115006.

[49] M. Martinez-Sanchez, J. Navarro-Cavallé, and E. Ahedo. "Electron cooling and finite potential drop in a magnetized plasma expansion". In: *Physics of Plasmas* Vol. 22. (2015), p. 053501.

[50] C.A. Deline et al. "Plume detachment from a magnetic nozzle". In: *Physics of Plasmas* Vol. 16. (2009), p. 033502.

[51] J.D. Jackson. *Classical electrodynamics*. 3rd Edition. John Wiley & Sons, 2021.

[52] D.M. Pozar. *Microwave engineering: theory and techniques*. 4th Edition. John Wiley & Sons, 2021.

[53] S. Errede. *UIUC Physics 436 EM Fields & Sources II Fall Semester, 2015*. Accessed 02/2025. URL: https://hep.physics.illinois.edu/home/serrede/P436/Lecture_Notes/P436_Lect_10.pdf.

[54] T. Vialis, J. Jarrige, and D. Packan. "Separate measurements of magnetic and pressure thrust contributions in a magnetic nozzle electron cyclotron resonance plasma thruster". In: *Space Propulsion 2018* (Seville, Spain). 2018.

[55] T. Vialis et al. "Direct thrust measurement of an electron cyclotron resonance plasma thruster". In: *Journal of Propulsion and Power* Vol. 34. (2018), pp. 1323–1333.

[56] T. Lafleur et al. "Electron dynamics and ion acceleration in expanding-plasma thrusters". In: *Plasma Sources Science and Technology* Vol. 24. (2015), p. 065013.

[57] C.E. Schäfer et al. "Influences on Langmuir probe measurements by an ECR thruster with magnetic nozzle". In: *New Results in Numerical and Experimental Fluid Mechanics XIV, STAB/DGLR Symposium 2022, Notes on Numerical Fluid Mechanics and Multidisciplinary Design* Vol. 154. (2022), pp. 153–162.

[58] S. Correyero et al. "Characterization of diamagnetism inside an ECR thruster with a diamagnetic loop". In: *Physics of Plasmas* Vol. 26. (2019), p. 053511.

[59] F. Boni, V. Désangles, and J. Jarrige. "Experimental characterization of thrust production mechanisms in a magnetic nozzle ECR thruster". In: *Journal of Electric Propulsion* Vol. 1. (2022), pp. 1–15.

[60] D. Packan et al. "The" MINOTOR" H2020 project for ECR thruster development". In: *36th International Electric Propulsion Conference* (Atlanta, USA). 2017.

[61] S. Correyero Plaza et al. "Ion acceleration in the magnetic nozzle of an ECR thruster: Comparison of experimental measurements with a quasi 1D kinetic model". In: *Space Propulsion 2018* (Seville, Spain). 2018.

[62] J. Jarrige et al. "Investigation on the ion velocity distribution in the magnetic nozzle of an ECR plasma thruster using LIF measurements". In: *35th International Electric Propulsion Conference* (Atlanta, USA). 2017.

[63] J. Jarrige et al. "Performance comparison of an ECR plasma thruster using argon and xenon as propellant gas". In: *33rd International Electric Propulsion Conference* (Washington D.C., USA). 2013, p. 420.

[64] B. Wachs and B. Jorns. "Background pressure effects on ion dynamics in a low-power magnetic nozzle thruster". In: *Plasma Sources Science and Technology* Vol. 29. (2020), p. 045002.

[65] V. Désangles et al. "ECRA thruster advances: 30W and 200W prototypes latest performances". In: *Journal of Electric Propulsion* Vol. 2. (2023), p. 10.

[66] *Testanlagen Übersicht*. Accessed 02/2025. URL: https://www.uni-giessen.de/fbz/fb07/fachgebiete/physik/institute/ipi/raumfahrtphysik/Ionentriebwerke/testanlagen.

[67] V.I. Demidov, S.V. Ratynskaia, and K. Rypdal. "Electric probes for plasmas: The link between theory and instrument". In: *Review of Scientific Instruments* Vol. 73. (2002), pp. 3409–3439.

[68] R.B. Lobbia and B.E. Beal. "Recommended practice for use of Langmuir probes in electric propulsion testing". In: *Journal of Propulsion and Power* Vol. 33. (2017), pp. 566–581.

[69] M.J. Druyvesteyn. "Der Niedervoltbogen". In: *Zeitschrift für Physik* Vol. 64. (1930), pp. 781–798.

[70] C.E. Schäfer. "Langmuir probe and Faraday cup measurements on the MINOTOR thruster at the DLR Göttingen". In: *German Aerospace Center, Spacecraft Department, Internal report.* 2022.

[71] I.H. Hutchinson. "Principles of plasma diagnostics". In: *Plasma Physics and Controlled Fusion* Vol. 44. (2002), p. 2603.

[72] S.T. Lai and C. Miller. "Retarding potential analyzer: Principles, designs, and space applications". In: *AIP Advances* Vol. 10. (2020), p. 095324.

[73] D.L. Brown et al. "Recommended practice for use of Faraday probes in electric propulsion testing". In: *Journal of Propulsion and Power* Vol. 33. (2017), pp. 582–613.

[74] M. Sangregorio et al. "Ion engine grids: Function, main parameters, issues, configurations, geometries, materials and fabrication methods". In: *Chinese Journal of Aeronautics* Vol. 31. (2018), pp. 1635–1649.

[75] A. Neumann, J. Simon, and J. Schmidt. "Thrust measurement and thrust balance development at DLR's electric propulsion test facility". In: *EPJ Techniques and Instrumentation* Vol. 8. (2021), p. 17.

[76] J. Schmidt, J. Simon, and A. Neumann. "Thrust measurements of the RIT-10 thruster with DLR's new DEPB thrust balance". In: *8th International conference on space propulsion* (Estoril, Portugal). 2022, pp. 1–7.

[77] J. Schmidt. "DLR Electric Propulsion Balance Documentation". In: *German Aerospace Center, Spacecraft Department, Internal report.* 2023.

[78] C.E. Schäfer et al. "Comparative study of electron temperature and ion energy in two different magnetic nozzle thruster designs". In: *Journal of Electric Propulsion* Vol. 3. (2024), pp. 1–20.

[79] K. Takahashi, T. Sugawara, and A. Ando. "Spatially-and vector-resolved momentum flux lost to a wall in a magnetic nozzle rf plasma thruster". In: *Scientific Reports* Vol. 10. (2020), p. 1061.

[80] J.M. Little and E.Y. Choueiri. "Critical condition for plasma confinement in the source of a magnetic nozzle flow". In: *IEEE Transactions on Plasma Science* Vol. 43. (2014), pp. 277–286.

[81] J. Schmidt and L. Basov. "Simulation of the neutral gas flow within an electric thruster by the kinetic Fokker-Planck method and comparison with force balance measurements". In: *33rd International Symposium on Rarefied Gas Dynamics* (Göttingen, Germany). 2024.

[82] H.-P. Harmann. "Untersuchung und Modellierung der Ionenstrahlformung großflächiger Ionenquellen mit Hilfe einer beweglichen Faradaysondenzeile". PhD thesis. Justus-Liebig Universität, Gießen, 2003.

Glossary

A_P Probe surface (m^2)
B Magnetic field (T)
C Capacitance (F)
E Energy (eV)
E_i Ion energy (eV)
I_beam Beam current (A)
$I_\mathrm{e,sat}$ Electron saturation current (A)
I_e Electron current (A)
$I_\mathrm{i,sat}$ Ion saturation current (A)
I_i Ion current (A)
J_beam Beam current density ($\frac{\mu\mathrm{A}}{\mathrm{cm}^2}$)
L Inductivity (H)
T_T Thrust (N)
T_e Electron temperature (eV)
U Voltage (V)
Φ_P Plasma potential (V)
Φ_fl Floating potential (V)
$\vec{B}$ Magnetic field (T)
$\vec{F}$ Force (N)
α Beam divergence angle (deg)
$\bar{\bar{\epsilon}}$ Dielectric tensor
λ_D Debye length (m)
ω_C Cyclotron frequency ($\frac{1}{\mathrm{s}}$)
ω_P Plasma frequency ($\frac{1}{\mathrm{s}}$)
ρ_L Larmor radius (m)
$f(E)$ Electron energy distribution function
m Mass (kg)
n Charge density (m^{-3})
n_e Electron density (m^{-3})
$p_{e,\perp}$ Perpendicular electron pressure ($\frac{\mathrm{eV}}{\mathrm{m}^3}$)
q Elementary charge (C)
r_B Beam radius (mm)
r_P Grid radius (mm)
v_i Ion velocity ($\frac{\mathrm{m}}{\mathrm{s}}$)

DEEP Decentralized Energy supplied Electric Propulsion
DEEVA DLR Electrodeless ECR Via microwave plasma Accelerator
DEPB DLR Electric Propulsion Thrust Balance
DLR Deutsches Zentrum für Luft und Raumfahrt

ECR Electron Cyclotron Resonance
ECRT Electron Cyclotron Resonance Thruster
EEDF Electron Energy Distribution Function
EM Electromagnetic
EP Electric Propulsion

FC Faraday Cup
FP Faraday Probe

IEDF Ion Energy Distribution Function

LIF Laser Induced Fluorescence
LP Langmuir Probe

MHD Magnetohydrodynamic
MINOTOR Magnetic Nozzle Electron Cyclotron Resonance Thruster
MN Magnetic Nozzle

OES Optical Emission Spectroscopy

RF Radio Frequency
RPA Retarding Potential Analyzer

STG-MT Simulationsanlage für Treibstahlen Göttingen - Miniatur Triebwerke

TB Thrust Balance

List of Figures

Index